Doctoral thesis

Study on Design Procedure of

Triple Active Bridge DC-DC Converter for

Hybrid Energy Storage Systems

Pham Van Long (Van-Long Pham)

TOKYO METROPOLITAN UNIVERSITY

Contents

vi

Journal papers 117

Patent 119

International Conference 121

Domestic Conferences 123

Acknowledgements 125

List of Figures

List of Tables

List of Abbreviations

TAB   Triple Acttive Bridge

DAB   Dual Acttive Bridge

Li-ion   Lithium-ion

HES   Hybrid Energy Storage

DC   Direct Current

PV   PhotoVoltaic

EVs   Electric Vehicles

OCV   Open Circuit Voltage

List of Symbols

P_r	rated power	W
L_{eq}	equivlent inductance	%
$L_\%$	normalized inductance	%
$P_\%$	normalized power	%
$V_{1\%}$	Voltage variation of primary port	%
$V_{3\%}$	Voltage variation of tertiary port	%
f	switching frequency	Hz
ω	angular frequency	rad

Chapter 1

Introduction

1.1 Research Background

1.1.1 Hybrid Energy Storage Systems

What are Hybrid Energy Storage Systems?

Hybrid energy storage (HES) systems, which are hybridized of Li-ion battery and other types of energy storage and renewable energy in a single system [1]-[5], are developing in many applications, as shown in Figure 1.1. For example, it is microgrid; a household electrical system connects photovoltaic (PV) power and electric vehicles (EVs), or storage systems; a plug-in hybrid electric vehicle (PHEV) uses hybrid fuel and plug-in battery; a battery electric vehicle (BEV) includes main battery and support battery; the direct current (DC) distribution connected to source, load, and battery.

Why Hybrid Energy Storage Systems are Developing?

The renewable energy systems and electric vehicles (EVs) are increasingly used in recent years [6]-[14]. Renewable energy systems include but are not limited to solar
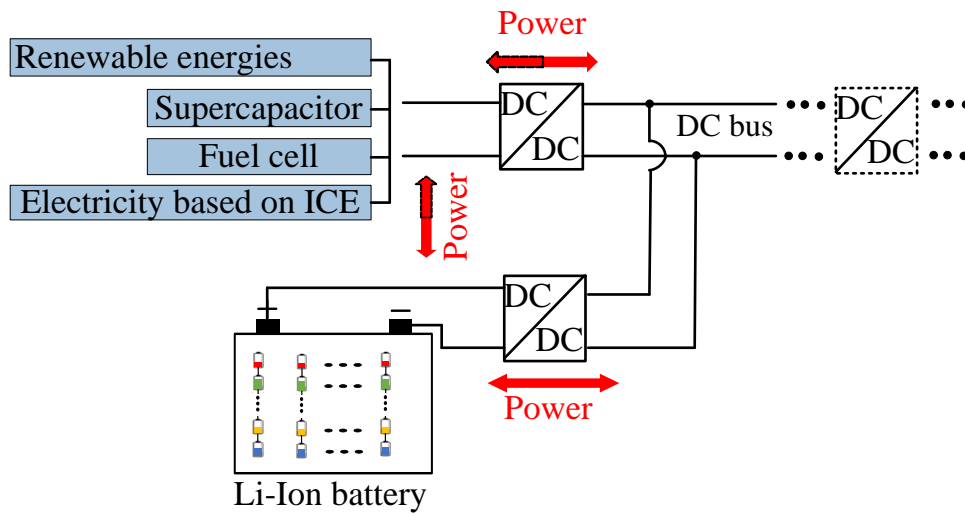
FIGURE 1.1: Hybrid energy storage (HES) systems.

photovoltaic (PV), wind power, biomass, hydro, and geothermal systems. World-wide yearly addition renewable energies include 60% PV solar and 30% wind power [8]. Together with the PV power plant, the rooftop PV system is a common and essential energy source for residential loads. On the other hand, Electric mobility is developing with the assistance of the participants of the electric vehicles initiative for electric vehicles (EVs). EVs have been developing rapidly during the last ten years, with the global stock of passenger EVs passing five million in 2018, which is 63% from 2017 [9]. The number of EVs is continuing increasing around 50% each year, from 5.3 million in 2018 to 130 million in 2030.

However, renewable energies have fluctuation voltage and power depending on the daily weather and time [11]-[13]. The solar PV energy, which depends on the sunny time, generates high power at day time. However, it does not has power at

night time. However, morning and evening is high load in residents [13]. There-fore, Battery and other energy storage can support PV and grid to increase the per-formance, stability, and reliability of the systems. Other than the battery storage station, EVs have a high capacity battery that can also be the storage to support the household, building, and grid. PV can charge EVs directly [14], and or EVs can support to grid [15]. Because many storage systems and household loads as are mainly direct current (DC) types, the DC grid has considerable potential for in-creasing the efficiency of distribution grids and reducing filter effort [16]-[18] in the future. Therefore, the future electrical grid systems include many HES systems, as shown in Figure 1.2.
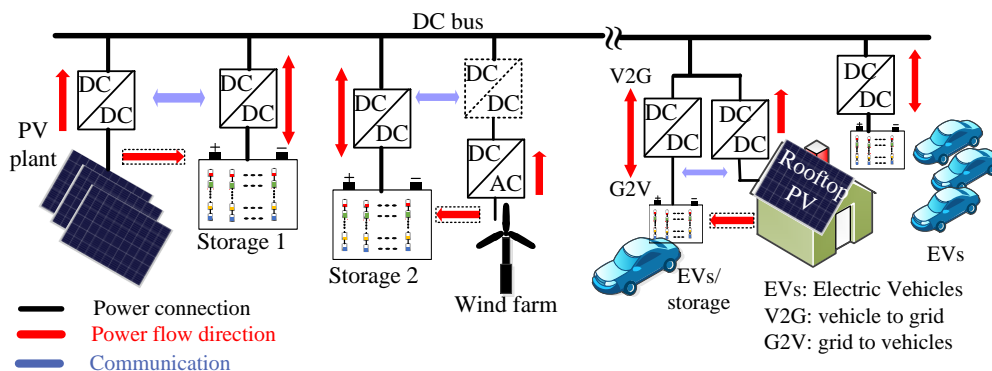
FIGURE 1.2: DC gid/microgrid including HES systems.

Moreover, specific energy (Wh/Kg) and specific power (W/Kg) of the Li-ion bat-tery are improved better than lead-acid batteries and nickel-cadmium (Ni-Cd) bat-teries, but are still under the expectation of electric mobility applications, as shown in Figure 1.3. Therefore, HES systems are developing for EVs application [19]-[23]. The EVs can be categorized in many types as battery electric vehicle (BEV), plug-in hybrid electric vehicle (PHEV), and hybrid electric vehicle (HEV). Other than

BEVs, HEV, and PHEV, many fuel cell EVs (FCEVs) are also developed and implemented [20]-[22]. However, the fuel cells have the disadvantage of a slow transient response. Therefore, the battery or supercapacitor is used to adapt to the fast response in FCEVs [23]. Japan's car strategy via a co-operative method throughout industrial stakeholders, targets to reduce 80% of greenhouse gas (GHG) emissions from cars produced by home automakers (90% for passenger EVs, consisting of exported vehicles), to be performed by 2050 with a combination of HEVs, BEVs, PHEVs, and FCEVs.
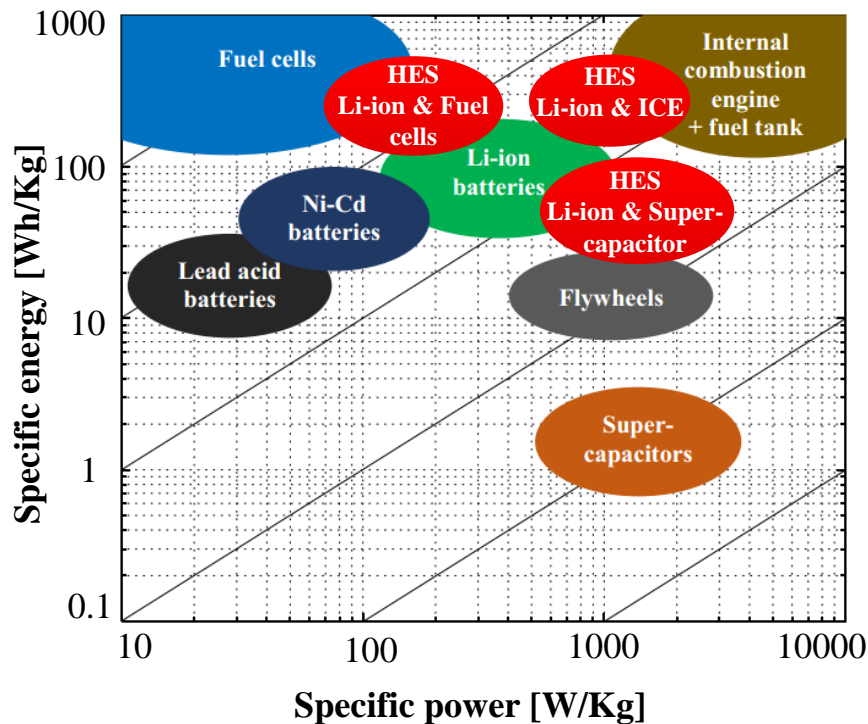
FIGURE 1.3: Specific power and energy of common sources for vehicles [3].

The HES systems can optimize the advantages of all the energy systems. HES systems contribute performance, stability, reliability, and flexibility of the applications. Therefore, HES systems will be developed more in the future.

1.1.2 Required Technologies and Challenges in Realizing HES Systems

DC-DC converter

The DC-DC converter is one of the essential technologies for realizing the HES systems [24]-[25]. DC-DC converters offer precise control ability for power flow with high reliability by controlling the voltage, current of each element. Dual active bridge (DAB), an isolated bidirectional DC-DC converter, has been proposed for many applications [26]-[27]. The DAB converter includes two full-bridge inverters that are connected by an isolation transformer at high-frequency operation, as shown in Figure 1.4. It has advantages such as a bidirectional power flow with high efficiency and a simple control method.
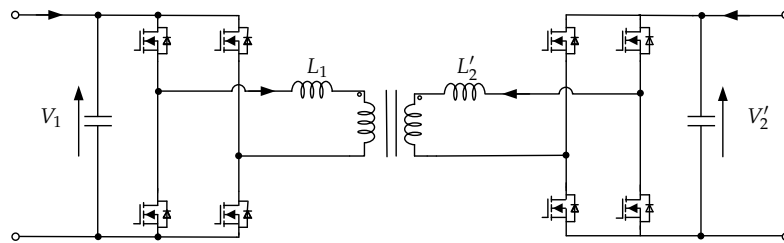
FIGURE 1.4: Dual active bridge (DAB) converter circuit.

However, it can only connect two ports; thus, many DAB converters need to be used to connect different elements to the DC-bus in the HES systems. Moreover, it may require a communication bus to control power flow. Therefore, the triple-active-bridge (TAB) converter is proposed to connect one more element by adding one more port to the DAB converter, as shown in Figure 1.5 [28]. The advantages of the DAB converter can be kept in the TAB converter. Moreover, the TAB converter enables flexible power transmission between three ports, as shown in Figure 1.6. This shows that three DAB converters are required in Figure 1.6 to achieve flexible

power transmission between three elements, which is achieved by only one TAB

converter in Figure 1.6b. Also, the communication between the three elements is not

necessary when using the TAB converter. Therefore, the control of the total system

is more straightforward. Therefore, the TAB converter is a next-generation DC-DC

converter for HES systems.
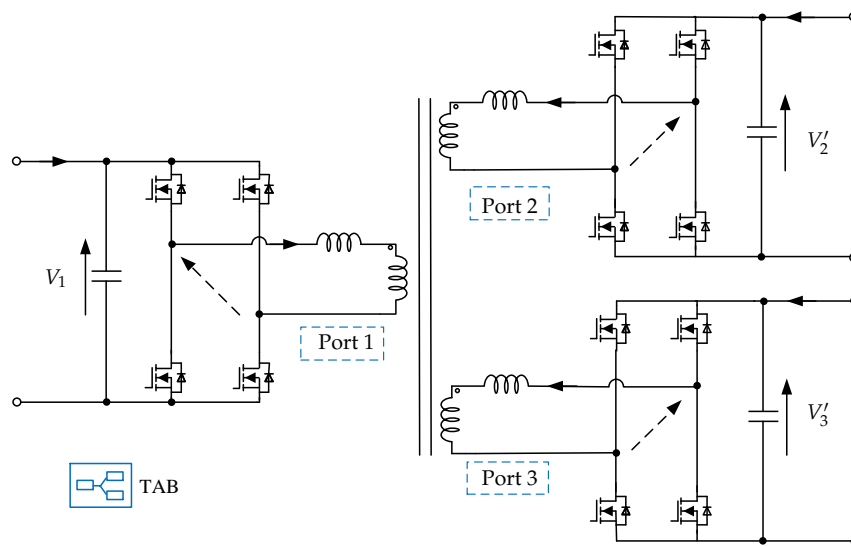
FIGURE 1.5: Triple-active-bridge (TAB) converter circuit.

(a)   (b)
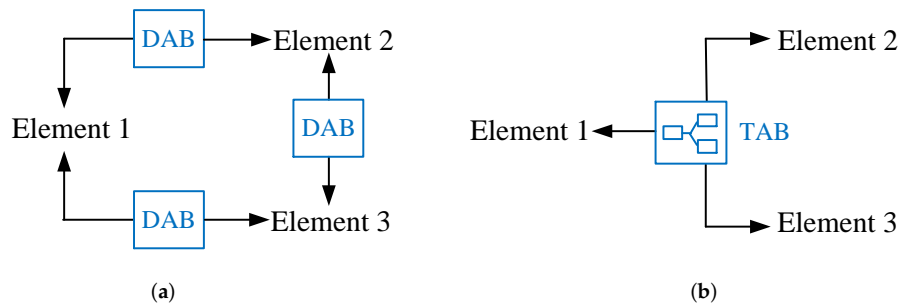
FIGURE 1.6: Comparison of a system using DAB and TAB converters.
(**a**) System using DAB converter, (**b**) System using TAB converter.

Li-ion Battery Capacity

The advantages of Li-ion batteries such as high energy efficiency, long life, and no memory effects, which make them ideal as the leading energy storage in HES systems [29]-[30]. The high adoption rate of Li-ion batteries for many applications is leading to the growth of the market. However, the safe operation and maximizing capacity of Li-ion battery are the challenges due to several hundred or thousand cells in a battery pack [31]. Figure 1.7 shows the usable charge/discharge and capacity loss of the battery pack in a charging/discharging cycle. The capacity loss keeps increasing by each charge/discharge cycle. In addition, the battery pack capacity in HES systems decides the operating voltage and capacity of the systems. Therefore, the battery voltage balancing is the technology to maximize the capacity and realize the battery's safe operation [31]-[32].
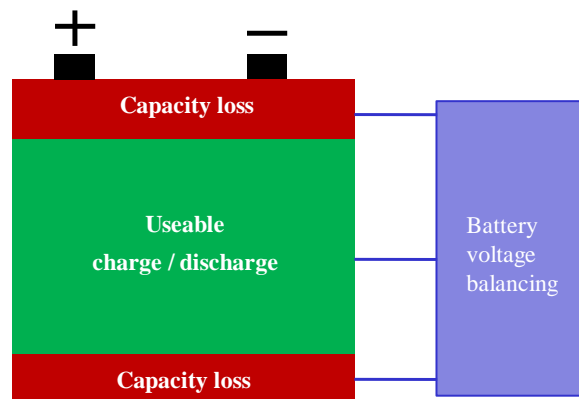
FIGURE 1.7: Capacity loss and battery voltage balancing.

1.2   Motivation and Objective

In the HES systems, the triple active bridge (TAB) converter, which is an isolated bidirectional DC-DC converter, has many advantages as a core circuit. The power control of the TAB converter for the HES systems is setup based on the voltage and current of the battery packs and other elements. However, the battery packs and these elements have a wide voltage variation. The voltage and current range and the rated power vary depending on the size and target of the systems.
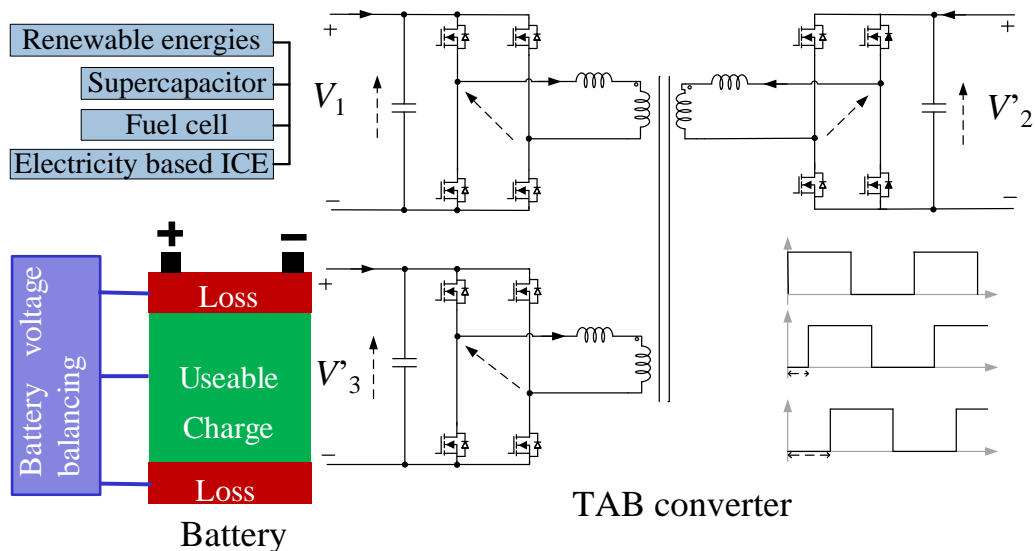
FIGURE 1.8: HES systems using the TAB converter and Li-ion battery.

Therefore, it needs a normalized design method of the TAB converter in considering voltage variation of the battery and other elements in the HES applications. Also, the suitable battery voltage balancing method is proposed to maximize the capacity of the battery pack and correct the battery cell voltage for safety operation.

This dissertation proposes the design procedure for the TAB converter. The voltage level and variation, which are different in each application, are normalized in

percentage. The complicated relationships between the elements of the TAB converter are clarified. The limitation of inductances corresponding to the different voltage variations is specified. The inductances are designed by considering the operation range of the phase shift angles. Therefore, the proposed design method can be applied in various rated power and voltage variation in many HES systems. Additionally, the Li-ion battery pack, which is used in many HES systems, is consisted of many cells connected in series and parallel to provide enough energy and voltage. The unbalanced voltage between the cells in a battery pack results in capacity loss and voltage error of the battery pack. Also, some cells may be overcharge voltage, which is very critical for the Li-ion battery. It affects the safety of the HES systems. Therefore, a cell balancing circuit is proposed in this dissertation for the battery pack to improve protection over cell voltage during the TAB converter operation and maximize the battery pack capacity.

1.3 Dissertation Outline

This dissertation proposes a design procedure of the triple active bridge converter and battery voltage balancing method for hybrid energy storage systems through the following chapters.

Chapter 1 introduces the study background of HES systems. The typical HES systems are introduced. The advantage of the HES systems is listed. Then, the technologies and challenges for realizing HES systems are described. The DC-DC converter and energy storage are the key technologies in realizing HES systems. The active bridge (TAB) converter, which is the next generation active bridge DC-DC

converter, and Li-ion battery capacity are the techniques to develop HES systems. Then, the target and outline of the dissertation are established.

Chapter 2 provides a literature review associated with this dissertation. Firstly, the HES applications using the TAB converter are discussed. The advantages and challenges of the TAB converter and Li-ion in each application are summarized. The voltage variation characteristics of the Li-ion battery and other storages or renewable energies need to be considered in the design of the TAB converter. Also, the usable capacity of the battery, which decides the usable capacity of the HES systems and voltage variation of the TAB converter, need to be corrected. Secondly, the current researches on the TAB converter are reviewed. The operation modes, control methods, and power transmission of the TAB converter are summarized. Many control methods are discussed. However, it remains a discussion about the design of the parameters of the TAB converters. The complicated relationship between parameters as inductances with powers and phase shift angles under the voltage variation is the remaining issue that needs to be solved. Thirdly, the capacity loss of Li-ion battery, which causes by the imbalance cell voltage between Li-ion battery cells in a battery pack, is revised based on the characteristics of the battery. The conventional cell balancing methods are analyzed. The remaining issues of the balancing method are summarized. Then, the remaining issues and research targets of this dissertation are explained clearly at the end of chapter 2.

Chapter 3 proposes a normalized design procedure for the TAB converter in considering the voltage variation of two ports. The voltage variations and inductances are normalized based on percentage, and the complicated relationships between the

elements of the TAB converter are clarified. The limitation of inductances corresponding to the different voltage variations is specified. The inductances are designed by considering the phase shift angle operating range of the TAB converter. Then, the proposed method is applied to design a system rated 400 V - 10 kW with the voltage of primary and tertiary port varies from 85 % to 110 %. A prototype converter rated at 200 V and 500 W is implemented to verify the proposed method.

Chapter 4 proposes a battery voltage balancing method for Li-ion battery pack in HES systems. The configuration and operation principle of the proposed balancing circuit is introduced. The open-circuit voltage (OCV), which is estimated based on a battery model, is introduced to compensate for the effect of the balancing current and load current to the terminal cell voltage. Therefore, all the cells can be balanced at the average OCV. A balancing converter is designed for the proposed balancing circuit to achieve high efficiency. An experimental balancing circuit is implemented for twelve Li-ion cells in a battery module. The experimental results are shown to verify the performance of the proposed battery balancing circuit.

Chapter 5 summaries the fulfillment of each chapter and the advantages of the HES using the TAB converter. Furthermore, the related topics that should be further studied are defined as future works.

Figure 1.9 shows a summarized view of the dissertation outline. Chapter 3 proposes the design procedure of the TAB converter for the HES applications. Chapter 4 proposes the battery balancing circuit for the battery pack in HES systems.
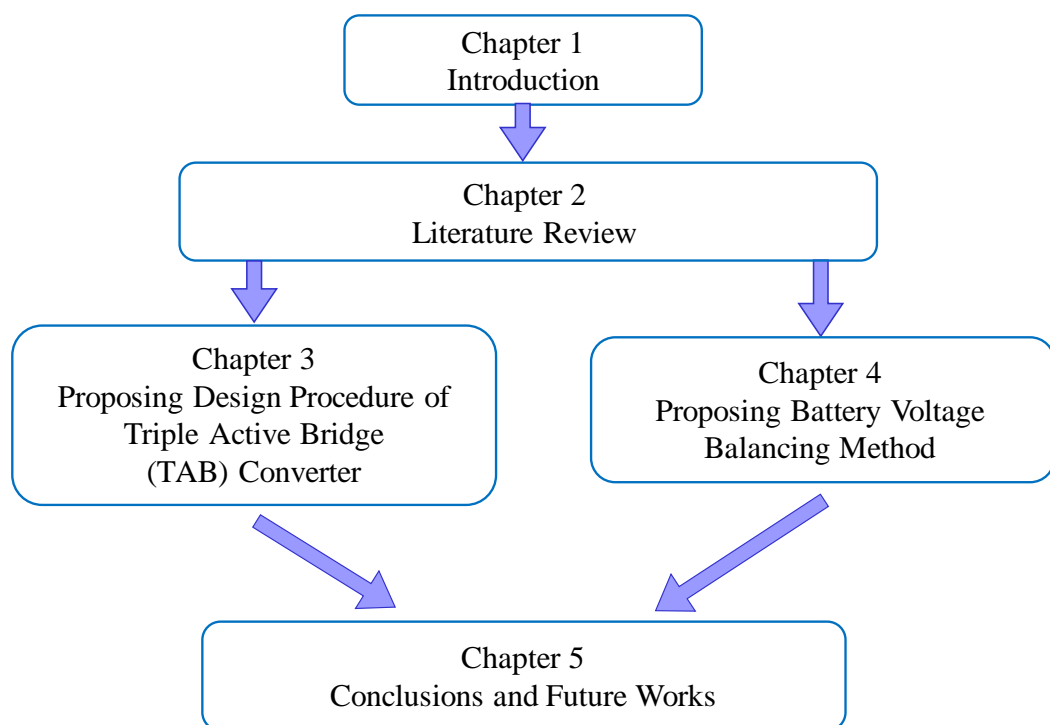
FIGURE 1.9: Dissertation outline.

Chapter 2

Literature Review

Figure 2.1 shows the connection and names all the elements of the TAB converter. n_2 is the turn ratio of the secondary port in comparison to the primary port of the transformer. It is also similar to the tertiary port, which is shown as n_3. The series inductances, L_1, L_2', and L_3' include the external inductance and leakage inductance on each side. The phase leg midpoint voltages u_1, u_2', and u_3' have the amplitudes V_1, V_2', and V_3', respectively.
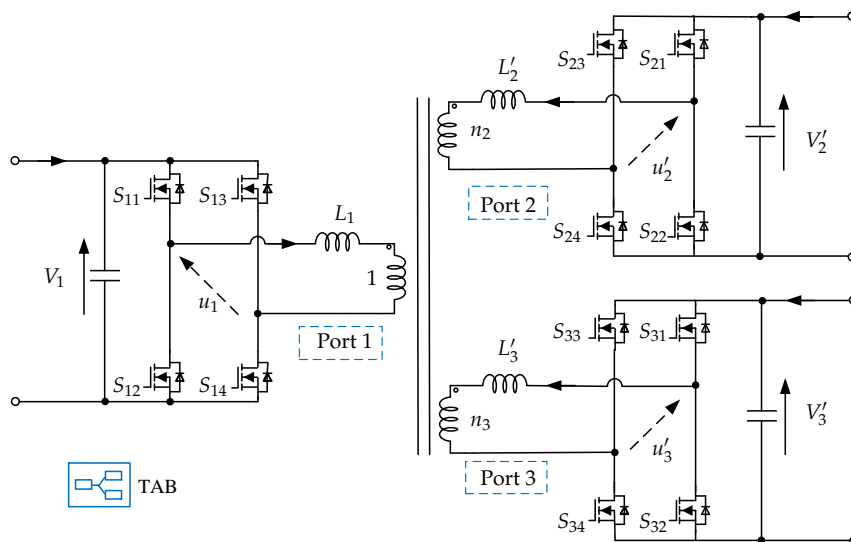
FIGURE 2.1: Triple-active-bridge (TAB) converter circuit.

The TAB converter has many working operation modes, as shown in Figure 2.2
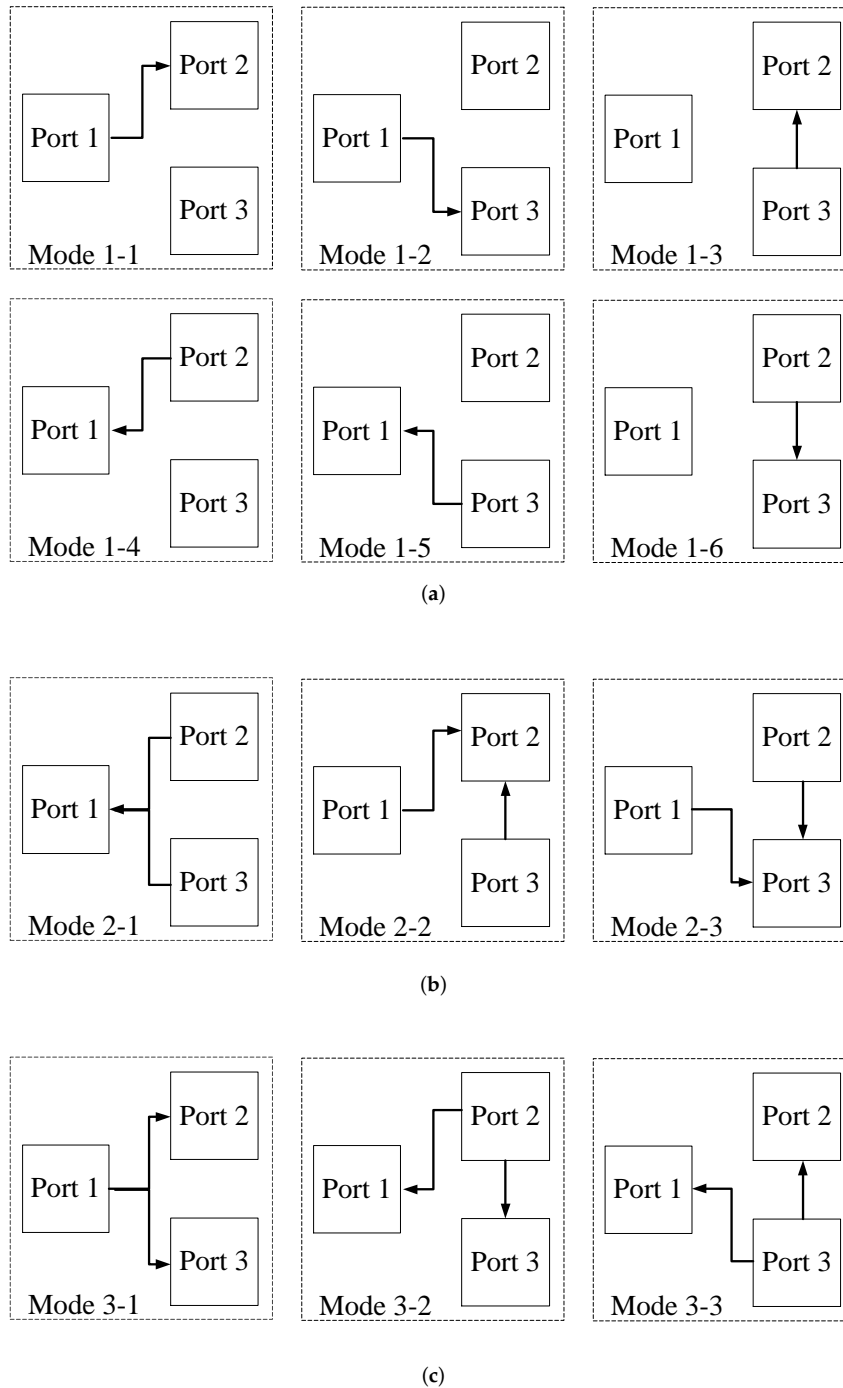
FIGURE 2.2: Operation modes of TAB converter: (**a**) Single input single output (SISO), (**b**) Dual input single output (DISO), (**c**) Single input dual output (SIDO).

[33]. It can be categorized into three groups. The single input single output (SISO) modes when the power comes from one port to another while the third port does not get power. The dual input single output (DISO) modes, which supplies power to one port from the other two ports. The single input dual output (SIDO) modes when power from one port is supplied to the two other ports. This shows the flexible power transmission ability of the TAB converter.

2.1   Characteristics and Requirements of HES Systems using the TAB Converter

Because there is an increase in the number and types of microgrids [34]-[35], the TAB converter is proposed to develop micro-grid systems, as shown in [36]-[39]. An un-interruptible power supply (UPS), which uses a battery to support the source in the worst-case scenario, is a suitable application for the TAB converter [40]-[42]. The TAB converter was discussed as an important part that can improve the reliability of the distribution system in the data center [46]-[48]. The proposed system in EVs applications is discussed in [50]-[54]. Also, many new applications such as all electrical ships, and autonomous underwater vehicles are replacing other energy systems with electricity.

2.1.1   Microgrids

A microgrid is an integrated system that combines sources, storage systems, and loads [34]-[35]. The DC household electrical system is discussed in [35]. The DC bus Microgrid systems using TAB converter were discussed in [36]-[39], as shown in

Figure 2.3. It shows that the system using the TAB converter can reduce the required number of DC-DC converters and communication lines. Consequently, the cost of the system is reduced.. The rapidly increasing use of EVs will bring much change in household electrical systems in the future. The EVs or storage can be charged from the grid or directly from the rooftop PV. In addition, EVs have a high-power battery, which can be a storage and support system for the household load or grid [15]. By using the TAB converter, the DC bus microgrid system becomes more flexible in setup and more optional in operation, which are advantages.
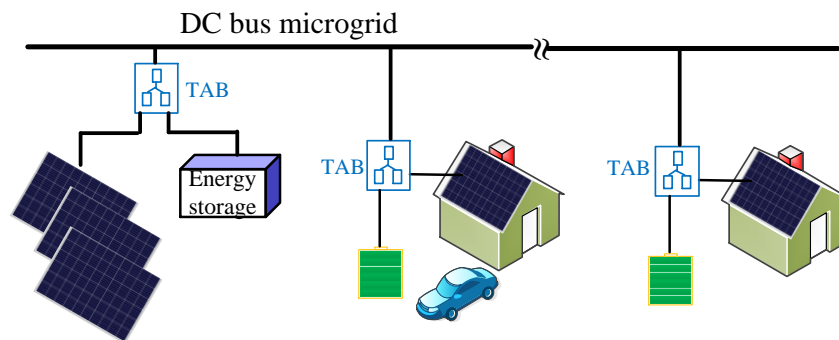
FIGURE 2.3: DC bus microgrid system uses the TAB converter.

An autonomous DC microgrid using the TAB converter is proposed in [37]-[39], as shown in Figure 2.4. One port of the TAB converter is connected to one element, and the remaining two ports are connected to the autonomous DC microgrid to control the power and voltage. The TAB converter can change the control target to keep a constant voltage and current for the different load or source depending on the system's condition. The transformers of the TAB converters isolate all the parts of the microgrid. Therefore, if one element has an error; other elements still work well. Also, the system is easy to extend at any time. The DC/AC converter can be added

to a port that connects to an AC load or source. This idea can be applied to the traditional microgrid system when some elements are used to improve reliability. In the future microgrid system, the TAB converter is a promising circuit when combining two above systems.
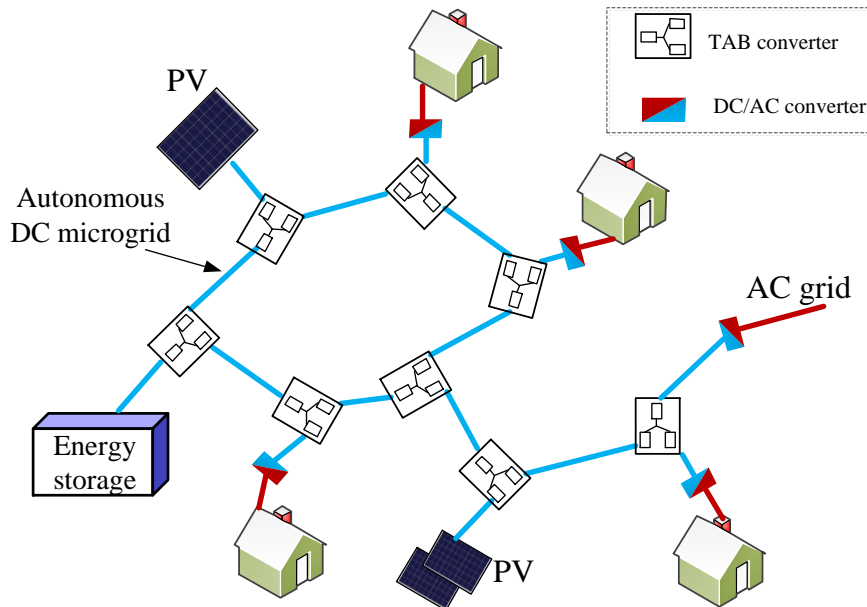
FIGURE 2.4: TAB converter for an autonomous DC microgrid system.

2.1.2 Uninterrupted Power Supply Systems

The TAB converter was proposed for the uninterrupted power supply (UPS) systems [40, 41], as shown in Figure 2.5. The power source, load, and battery are connected using one TAB converter as discussed in [40, 41], where the power source and electric load may require frequency isolation of 50 Hz and 60 Hz, respectively. The system operates typically in the mode 1-1. However, all remaining modes can be used in an abnormal situation. By using a TAB converter with a three-winding transformer, the safety of the system is improved. The operation of the system is flexible with simple control.
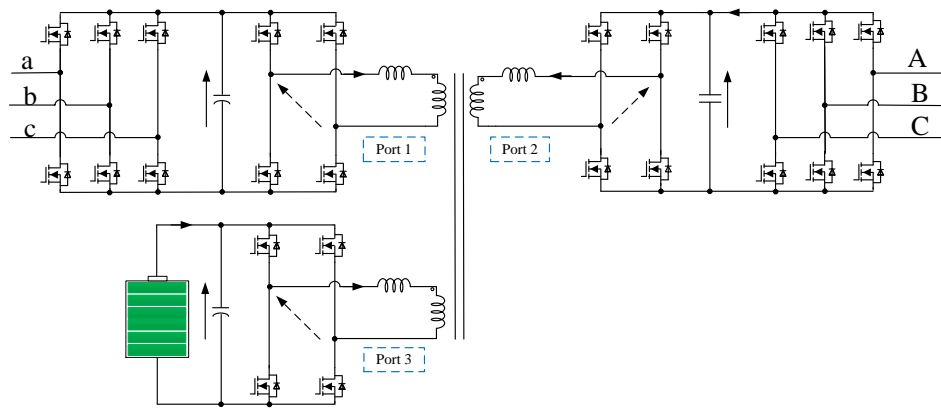
FIGURE 2.5: TAB converter in UPS application.

A UPS system powered by a fuel cell is proposed by using a TAB converter in [42]-[44]. The system is flexible and can work on grid-connected or stand-alone modes. The fuel cells have a slow transient response, which is a drawback. The supercapacitor can be used as storage to support the fuel cells to respond quickly in transient time. Depending on the load and the status of the supercapacitor and fuel cell, it may operate in different modes. This could be discussed more in the future. For high power applications, multiple TAB converter can be used. One port, which can be connected in series for high voltage application, can be connected in parallel for the three-phase TAB converter can also be used. This shows that the TAB converter is an excellent selection for these proposed systems where all operation modes are achieved by one converter.

2.1.3 Power Distribution for Data Center

The reliability of the distribution systems for data centers is one of the most critical points. Interruptions of power systems in the data center have a high cost of millions of dollars an hour [45]. Therefore, the TAB converter was proposed to improve the reliability and availability of power distribution of data centers in [46]-[48], as shown

in Figure 2.6. This system can operate as a UPS system to prevent power faults in

the data center's distribution systems. The number of converters can be reduced

by sharing a battery between two distribution lines. Consequently, using the TAB

converter can reduce the cost of the system. Furthermore, two distribution lines can

support each other in a critical situation. Therefore, all operation modes of the TAB

converter can be used in this application, which maximizes the advantages of the

TAB converter.
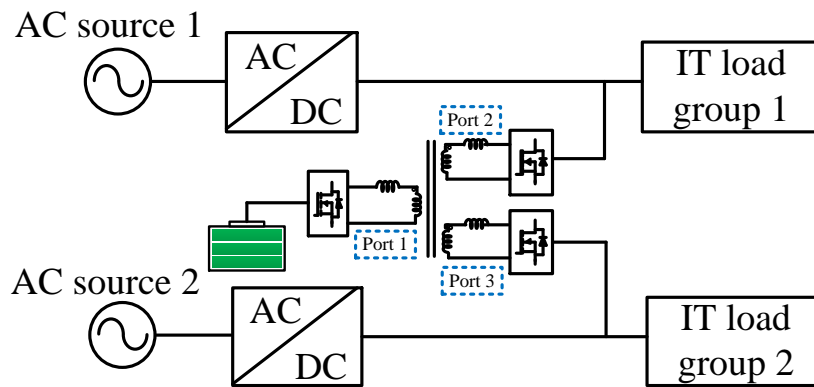
FIGURE 2.6: TAB converter in power distribution for data center application.

2.1.4 Electric Vehicles

Electric vehicles (EVs) normally have a high voltage (HV) battery of 300 V–400 V and

a low voltage (LV) battery of 14 V [49]. The HV battery supplies the main power for

the motor. The LV battery supplies power for other facilities such as the fan, light,

wiper, radio, and others. The on-board charger is implemented in EVs to charge

the EVs at home with a power range of 3–6 kW. Therefore, the DC-DC converter

and charger are combined using the TAB converter, as shown in Figure 2.7 [50]-[52].

The port-1 is connected to the main battery. The port-2 is connected to the low voltage battery. The port-3 is connected to the DC source after the rectifier from the AC grid. The two DC-DC converters in the conventional system are combined by using one TAB converter. This reduces the components, size, and cost of the system. However, the idling isolation of the charger port is a challenge in this application. Therefore, the combined voltage duty cycles and two-phase shift angles method is proposed for this condition to reduce the peak and root mean square (RMS) current [50]-[54]. It shows that this method can be applied in other applications that have a similar critical condition.
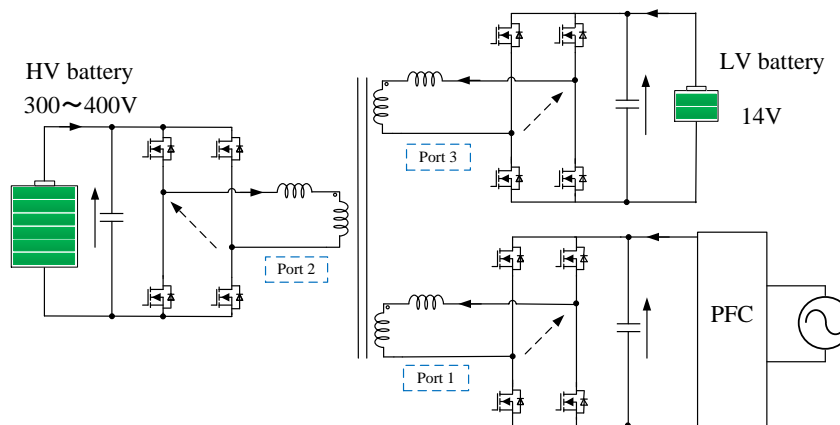
FIGURE 2.7: TAB converter for electric vehicles (EVs) application as
an integrated on-board charger and DC-DC converter.

The 42 V bus for EVs was discussed in [54] to increase the power for HEVs. Therefore, the electrical system may have three voltage levels (14 V / 42 V / 400 V). The TAB converter has many advantages for this system because it separates voltage levels using one converter with a three-winding transformer, as shown in Figure 2.8. The power can be supplied from three storage systems adequately during start-up or regular running. It shows that all the operation modes of the TAB converter can be applied in this application to maximize the power and lifetime of the system.
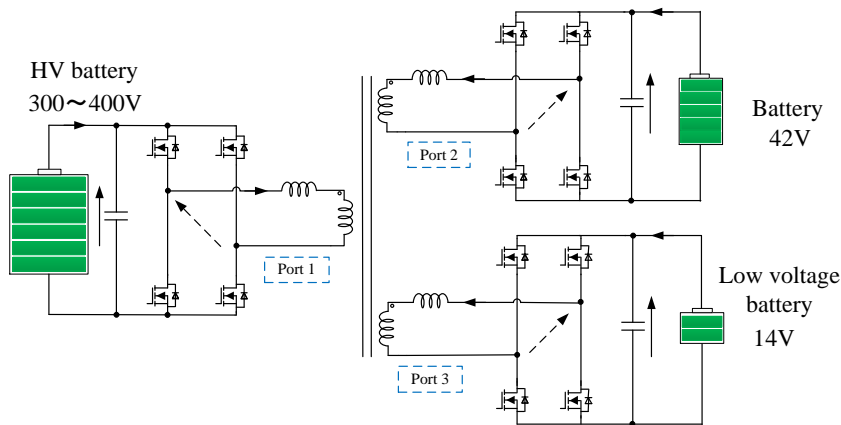
FIGURE 2.8: DC-DC converter in EVs application using the TAB converter.

2.1.5 More Electric Aircraft

Besides electric vehicles, the more electric aircraft (MEA) has been widely researched and discussed to reduce CO2 emissions in the world [56]-[57]. The electrical system in MEA requires improved efficiency, reliability, and reduced implementation costs. The electrical system usually uses a 230 V AC voltage and two DC voltages, of 270 V and 28 V. The auxiliary power unit (APU) is used to supply power when the MEA is on the ground. It can use a battery and fuel cell system of 270 V or 540 V [57]-[59]. The battery can also be used for emergencies, to store energy in low load conditions, and support in heavy load conditions. Therefore, the TAB is proposed to regulate power flow in MEAs in [60], as shown in Figure 2.9. Two DC voltages and APU are connected and supported by one TAB converter and a centralized control system.

Using the TAB converter is advantageous because the power between three elements always works together to achieve the high safety and reliability of this application. However, high current and high power design and control are the challenges of this application. More research and verification should be discussed in detail in

the future.
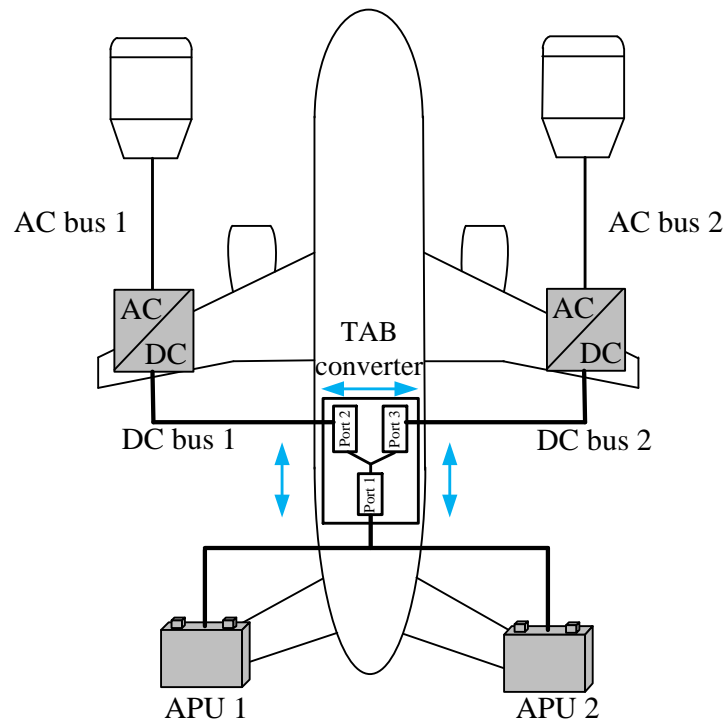
FIGURE 2.9: TAB converter in more electric aircraft application.

2.1.6   Autonomous Underwater Vehicle

The autonomous underwater vehicle (AUV) is spread widely in recent years [61]-
[63]. The size and weight of the AUV are limited, and the data can be corrected if
the AUV can work for a long time. Therefore, the power system of the AUV is a
challenge. The Lithium-ion battery is used for AUV because of its high power den-
sity [61]. The fuel cell system for AUV is discussed to extend their working time [62].
The integrated fuel cell and battery systems for AUV have been discussed in recent
times [63]. This can achieve a higher power density, which reduces the number of
the batteries and increases the power for the AUV. With the many advantages in the

integrated power system, the TAB converter is a promising candidate for this application. A TAB converter can be connected directly between the motor driver (M), fuel cell, and battery, as shown in Figure 2.10. It can use a 48 V battery with a capac-
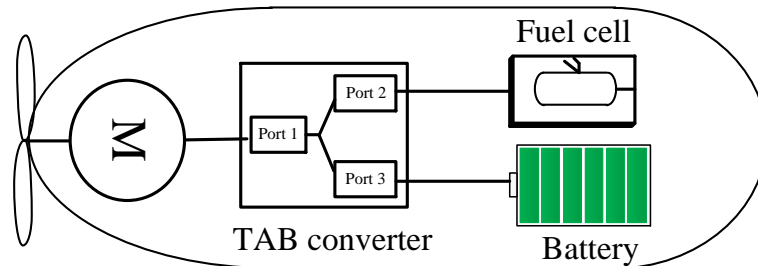
FIGURE 2.10: Autonomous underwater (AUVs) vehicles using the
TAB converter.

ity of 34 Ah for a small AUV [63]. A fuel cell can install a 48 V system. The converter operates at 1 to 3 kW. However, this application requires high efficiency and small size. To realize a large power AUV system, the system can be implemented with an optimal design of the TAB converter, depending on the battery and fuel cell system.

2.1.7 All-Electric Ships

All-electric ships (AESs) are developed to improve the efficiency of energy in the ships [64]-[65]. The advantages of MVDC distribution for all-electric ships (AESs) were discussed in [66]. By using MVDC (1–8 kV) distribution, the motor is not connected to a fixed-frequency system and can be designed and operated to maximize efficiency. The advantage of the battery energy storage system (BESS) for the ship was discussed in [67]. Therefore, the electrical ship is a promising application of the TAB converter in the future, as shown in Figure 2.11. The battery and supercapacitor can be charged by regenerative energy in the light load condition, and then used for the heavy load condition. It stabilizes the voltage and current of the electrical grid
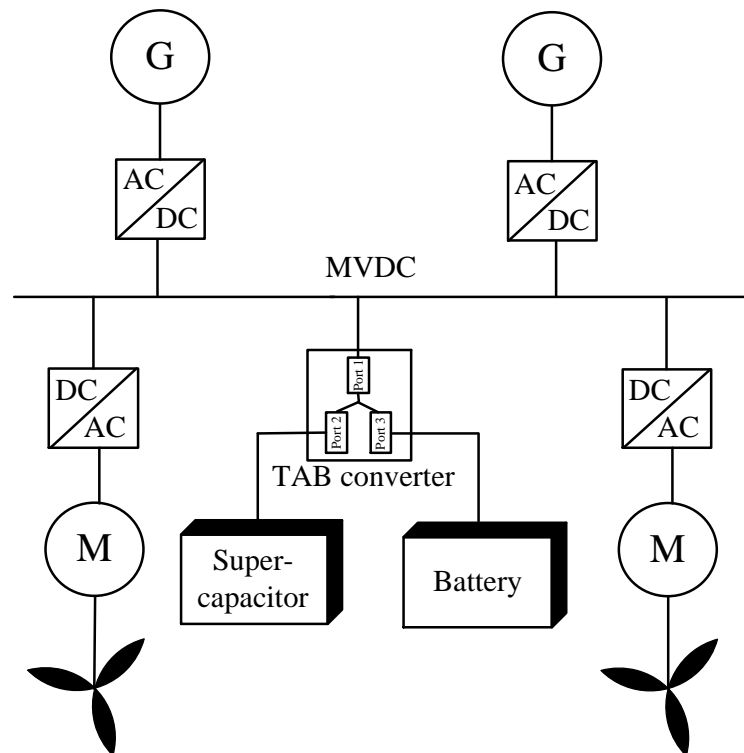
FIGURE 2.11: Proposed TAB converter for future all-electric ships.

in the ship. Additionally, the battery and supercapacitor are useful auxiliary power

systems for rapid-starting in booster or electric-motor modes. Depending on the size

and type of ship, the power system may range from 500 kW to several megawatts.

The storage capacity can be selected depending on the control strategy and imple-

mented by the 400 V level. The TAB converter for AESs application may work at

several hundred kW, which is challenged by the high voltage high power design.

2.1.8   Summary of Characteristic and Requirements for the TAB Converter Li-ion Battery

This subsection gives a summary of current and potential future HES systems using

the TAB converter. The advantage and challenges of each application are summa-

rized, as shown in Table 2.1. For each application, the TAB converter contributes

to the different targets to develop conventional systems. There are also different challenges in each application, which also need more development in the future. It shows that some applications use all operation modes such as microgrid, distribution systems for data center, electric vehicles, and more electric aircraft. The TAB converter is a good selection because of saving cost and improving reliability. Some applications do not use all operation modes. However, by using the TAB converter, it not only reduces the component but also extends the functionality of the system.

TABLE 2.1: Characteristics of the HES Applications using the TAB Converter.

Application	Meaning of the TAB Converter	Challenges	Operation Modes			Suggest/Note
			Normal	Abnormal	Do Not Use	
DC-bus micro-grid (Figure 2.3)	Reducing the components and cost; centralizing control in each household;	Variation voltage from variation connection to each house hold system;	1-1; 1-2; 3-1;	1-3; 1-6; 2-2; 2-3;	1-4; 1-5; 1-6; 2-1; 3-2; 3-3;	By combining two ideas, the TAB can develop the future micro grid system.
Autonomous microgrid (Figure 2.4)	Easy to be extended or maintained any time;	Still large number of converter complex control of the system level;	All	N/A	No	
UPS with AC source (Figure 2.5)	Improving safety and reliability; flexible operation;	Fast transient response strategy;	1-1;	Remain modes;	No;	N/A
Data center 1 (Figure 2.6)	Reducing the components, cost, and size; balancing two loads;	Stability and accuracy of the system;	No	All	No	N/A
EVs 1 (Figure 2.7)	Reduce the components, cost, and size of the system;	Virtually isolating the AC charger side;	1-1; 1-3; 1-5; 3-3;	1-4; 2-1; 2-2;	1-2; 1-6; 2-3; 3-1; 3-2;	N/A
EVs 2 (Figure 2.8)		Optimal transmission power of each element;	1-1; 1-2; 1-6; 3-1;	1-3; 1-4; 1-5; 2-1; 2-2;	No	N/A
More Electric Aircraft (Figure 2.9)	Improving the reliability of the system;	High current and power design;	All	No	No	Increase voltage of the system to reduce operating current;
AUV [proposed] (Figure 2.10)	Central power control by only one converter;	High efficiency and high power density;	1-4; 1-5; 1-6;	1-2; 2-1; 2-3; 3-2;	1-1; 1-3; 2-2; 3-1; 3-3;	N/A
AES [proposed] (Figure 2.11)	DC grid for ship to maximize the advantages; central power control by only one converter;	High voltage (1-8 kV) and high power 500 kW-MW design and measurement;	1-1; 1-2; 1-4; 1-5; 2-1; 3-1;	1-3; 1-6; 2-2; 2-3; 3-2; 3-3	No	Connecting many TAB converter in module for very high power and voltage application;

2.2 Current Status of Triple Active Bridge Converter

2.2.1 Converter Structure and the Variation of Topology

Other configurations, which can connect multiple single-phase TAB converters, can also be applied to interconnect MVDC and LVDC, as shown in Figure 2.12 [68, 69, 70]. It can connect two ports in series and one port in parallel to connect two MVDC grids and one LVDC grid, as shown in Figure 2.12a. Figure 2.12b shows the system which connects one port in series and two ports in parallel to connect one MVDC grid and two LVDC grids. The number of modules is selected depending on the available semiconductor devices and operating voltage.
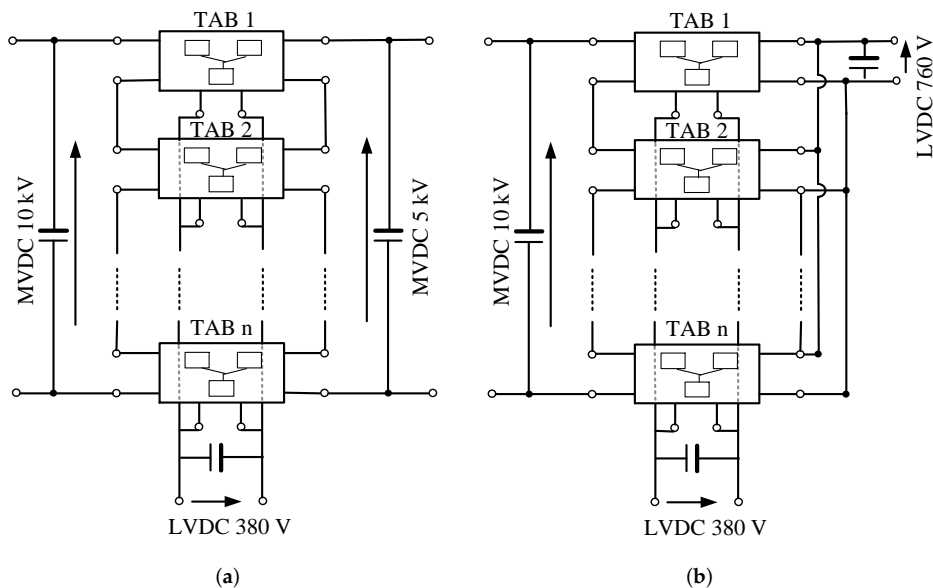
FIGURE 2.12: Multiple TAB converter for high voltage high power application: (**a**) two ports in series, one port in parallel; (**b**) one port in series, two ports in parallel.

In addition, a three-phase TAB converter is proposed for high power application by adding one switching leg to each inverter [71], as shown in Figure 2.13. Each phase of the three-phase TAB converter can be modeled as a single-phase TAB converter [71]-[76].
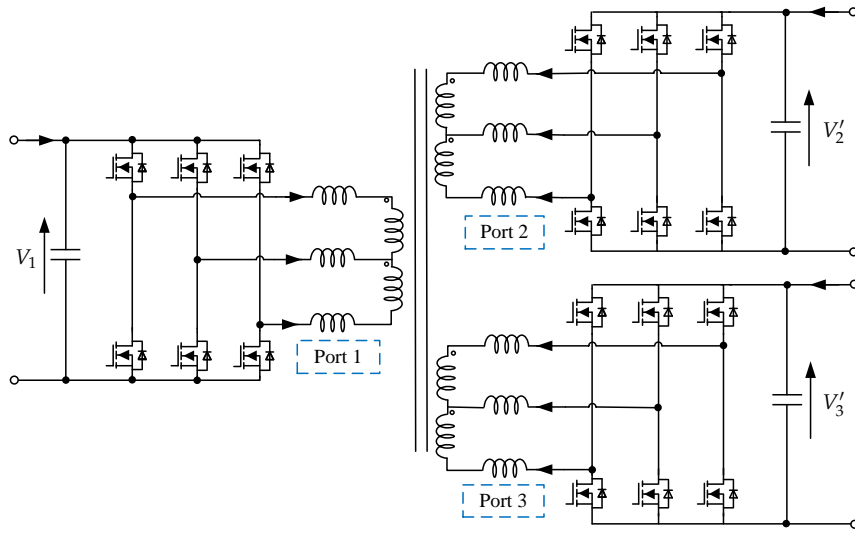
FIGURE 2.13: Three-phase TAB converter.

2.2.2 Power transmission

The primary-referred inductances and voltages are then used for the power calculation [54]. The power of each port is formulated in the equations below.

$$P_1 = \frac{V_1 V_2 \varphi_2 (\pi - |\varphi_2|) L_3 + V_1 V_3 \varphi_3 (\pi - |\varphi_3|) L_2}{2\pi^2 f (L_1 L_2 + L_2 L_3 + L_3 L_1)} \tag{2.1}$$

$$P_2 = \frac{V_2 V_1 (-\varphi_2)(\pi - |\varphi_2|) L_3 + V_2 V_3 (\varphi_3 - \varphi_2)(\pi - |\varphi_3 - \varphi_2|) L_1}{2\pi^2 f (L_1 L_2 + L_2 L_3 + L_3 L_1)} \tag{2.2}$$

$$P_3 = \frac{V_3 V_1 (-\varphi_3)(\pi - |\varphi_3|) L_2 + V_3 V_2 (\varphi_2 - \varphi_3)(\pi - |\varphi_2 - \varphi_3|) L_1}{2\pi^2 f (L_1 L_2 + L_2 L_3 + L_3 L_1)} \tag{2.3}$$

Where f denotes the switching frequency, and P_1, P_2, and P_3 are the transmission power of the primary, secondary, and tertiary sides, respectively.

For I_{p2} and I_{p3} are the output currents of the secondary port and tertiary port.

Where $I_{p2}=P_2/V_2$, $I_{p3}=P_3/V_3$. By using sinusoidal approximation and linear approximation, the linear model of converter is shown as the following.

$$
\begin{bmatrix} I_{p2} \\ I_{p3} \end{bmatrix} = \begin{bmatrix} \frac{4L_3}{\pi^3 fL_{sum}}V_1 + \frac{4L_1}{\pi^3 fL_{sum}}V_3 & -\frac{4L_1}{\pi^3 fL_{sum}}V_3 \\ -\frac{4L_1}{\pi^3 fL_{sum}}V_2 & \frac{4L_2}{\pi^3 fL_{sum}}V_1 + \frac{4L_1}{\pi^3 fA}V_2 \end{bmatrix} \begin{bmatrix} \varphi_2 \\ \varphi_3 \end{bmatrix} \tag{2.4}
$$

$$
\begin{bmatrix} I_{p2} \\ I_{p2} \end{bmatrix} = \begin{bmatrix} T_{11} & T_{12} \\ T_{21} & T_{22} \end{bmatrix} \begin{bmatrix} \varphi_2 \\ \varphi_2 \end{bmatrix} \tag{2.5}
$$

Where $L_{sum} = (L_1L_2 + L_2L_3 + L_3L_1)$. It shows that, the phase shift can control the amount and direction of the power.

2.2.3   Control Method

The equation (2.4) and (2.4) show the interaction from φ_2 and φ_3 to I_{p2} and I_{p3}. The interference can be eliminated via a compensation network by decoupling matrix [D] is implemented in the controller. With u_2 and u_3 are the output of the controllers as shown in Figure 2.14.

$$
\begin{bmatrix} \varphi_2 \\ \varphi_3 \end{bmatrix} = \begin{bmatrix} D_{11} & D_{12} \\ D_{21} & D_{22} \end{bmatrix} \begin{bmatrix} u_2 \\ u_3 \end{bmatrix} \tag{2.6}
$$

$$
[D] = [T]^{-1} = \begin{bmatrix} T_{11} & T_{12} \\ T_{21} & T_{22} \end{bmatrix}^{-1} = \frac{1}{T_{11}T_{22}-T_{12}T_{21}} \begin{bmatrix} T_{22} & -T_{12} \\ -T_{21} & T_{11} \end{bmatrix} \tag{2.7}
$$

From the above equation, the decoupling matrix is implemented into the control loop to remove the interference among the ports [39, 54, 55] The current control loops for TAB converter are designed as the following.
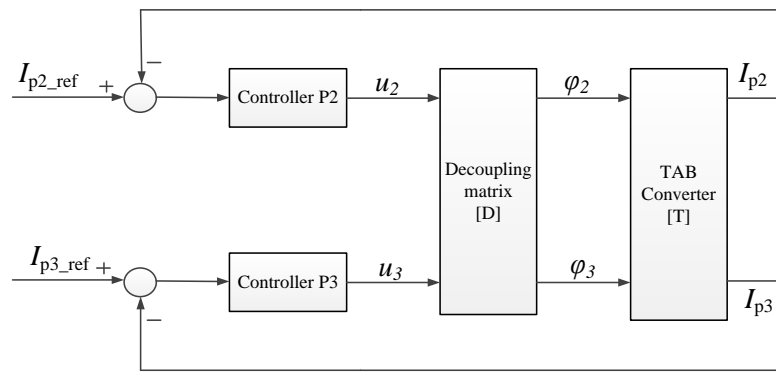
FIGURE 2.14: Decoupling current control loop.

Therefore, the power transmission ability of each port can be controlled by two-phase shift angles, φ_2 and φ_3, as shown in Figure 2.15a. The phase shift angles between u_1, u_2, and u_3 decide amplitude and direction of the transmission power among the three ports [37, 38, 39]. Besides, the combined duty cycles and two-phase shift angles methods were discussed to improve the efficiency of the TAB converter, as shown in Figure 2.15b [52, 53, 54, 44]. δ_1, δ_2, and δ_3 are duty cycle variations of u_1, u_2, and u_3, respectively. This technique can extend the soft switching at light load, but it reduces the power transmission ability of the converter [44]. Furthermore, upon adding more variables to the system, the control system, and calculation of the controller become more complex. Therefore, the two-phase shift angles method is widely used for controlling the TAB converter in many applications. The combined duty cycle and two-phase shift angles method can be considered for applications that usually operate under light load condition.
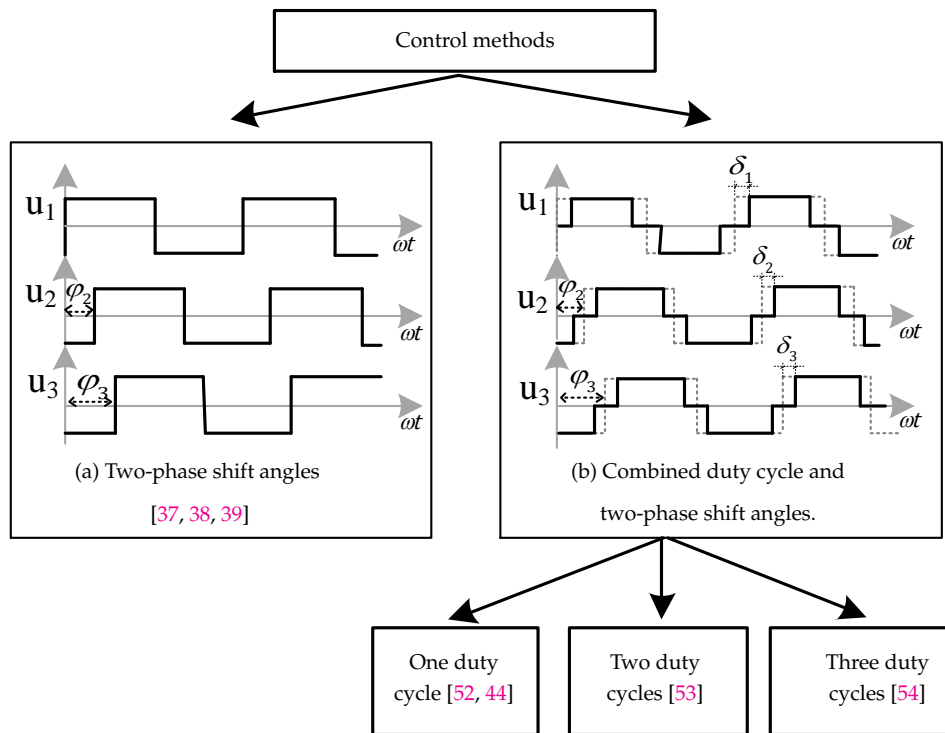
FIGURE 2.15: Control methods of the TAB converter.

2.3   Capacity Loss and Battery Voltage Balancing Methods

2.3.1   Why does Capacity Loss Happen?

Lithium-Ion (Li-Ion) batteries have become increasingly important in many applications due to high power and energy density. Figure 2.16 shows the SOC-OCV curve of a Li-ion battery cell. Each cell of Li-ion battery has small voltage as 2.5 V - 4.2 V. Therefore, a battery pack typically is composed of many cells connected in series and in parallel to supply sufficient power as required voltage and capacity by the specifications, as shown in Figure 2.17. In a battery pack, each cell may have different characteristics and capacities due to variances in assembly or manufacturing processes. As the charge and discharge processes repeat, the unbalance of the charges in the cells increases as shown in Figure 2.18.
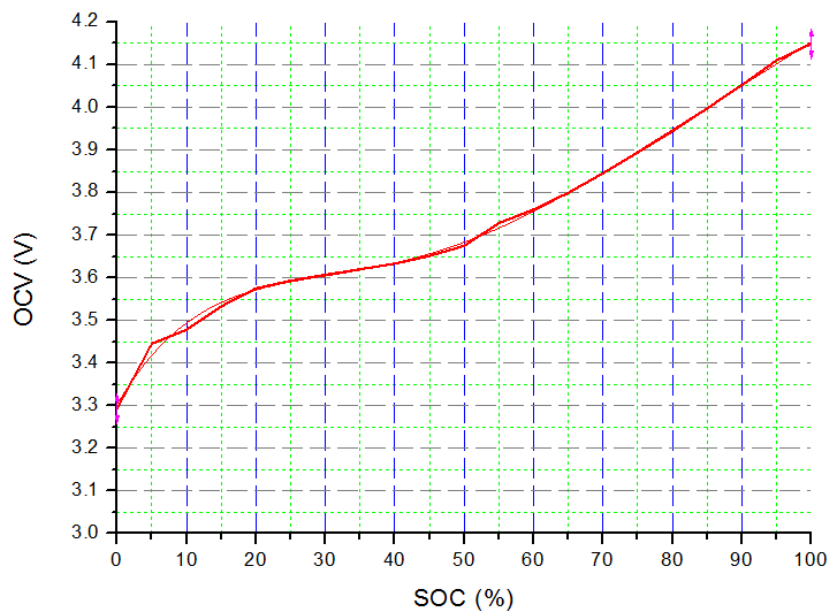
FIGURE 2.16: Voltage and state of charge of one lithium-ion battery
cell.

If the unbalance issue is not recognized and solved, the weakest cell undergoes

over-discharge and undercharge and eventually reaches failure. In the meanwhile,

the normal cell may experience overcharge because the charge operation continues

until the string voltage reaches the nominal value. In case of Li-Ion batteries, it

is extremely important not to exceed the maximum voltage during charging since

this accelerates the formation of a Solid Electrolyte Interface (SEI) film on the nega-

tive electrode which further accelerates the aging of the battery [77]-[78]. The over

voltage of li-ion can make a fire. Also, the capacity of the battery pack is reduced

during each charge or discharge cycle. Therefore, the cell balancing circuit is crucial

to achieve cell voltages that are the same to extend the life cycle and capacity of the

battery pack [79].
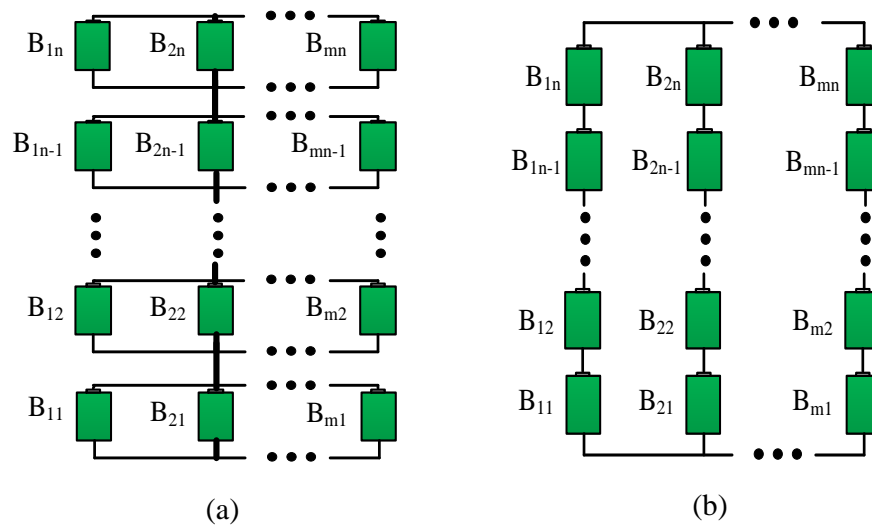
FIGURE 2.17: Many battery cells are connected in series and parallel in a battery pack.
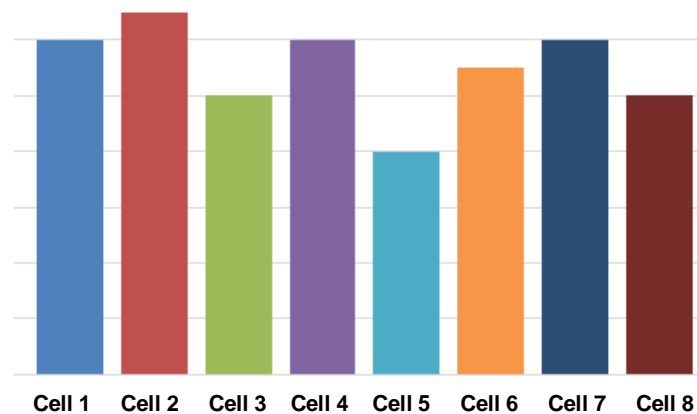
FIGURE 2.18: Unbalance of the battery cell in a pack.

2.3.2 Battery Voltage Balancing Methods

Various kinds of cell balancing topologies have been discussed to cope with unbalanced problems [80]-[104]. They are divided in two types, passive balancing methods and active balancing methods. The passive balancing methods use resistors to discharge the highly charged cells [80]-[82]. The advantages of passive balancing include low cost and easy implementation. The passive methods that use resistors to

discharge the overcharged cells are useful for lead-acid batteries and Ni-MH batteries. However, it is unfavorable in that the power is only dissipated by converting it into heat and heat dissipation becomes another concern. In the case of a lithium-ion battery, it is well known that the life cycle can become shorter and that it can cause a fire [83]-[84]. Therefore, active balancing methods are preferred since they can transfer power from a cell with a higher charge to a cell with a lower charge to save the energy and to protect the batteries.

Many kinds of active balancing methods are under researched [85]-[104]. These methods are often divided into four types: pack-to-cell, cell-to-pack, cell-to-pack-to-cell, and cell-to-cell methods Figure 2.20. A comparison of the balancing methods in terms of component count and characteristics is shown in Table 2.2. The pack-to-cell balancing methods are outstanding in terms of balancing speed when a cell is less charged than others, and the others are all balanced [85]-[88]. However, if one cell has a higher charge than those of the others, it takes a longer time to balance the battery module since the battery module needs to be discharged first. Then all of the other cells have to be charged again one by one. The cell-to-pack method can be implemented by using a transformer or multiple transformers. The cell-to-pack balancing methods have a very low speed when one cell has a lower charge than the others [89]-[91]. Also, the two methods require a lot of bidirectional switches and gate drivers, it is high in cost and low in balancing speed.

The cell-to-pack-to-cell balancing methods were proposed to provide a solution to these problems by combining the advantages of the other two methods [92]-[93]. However, two converters are required in this method and the voltage stress of the
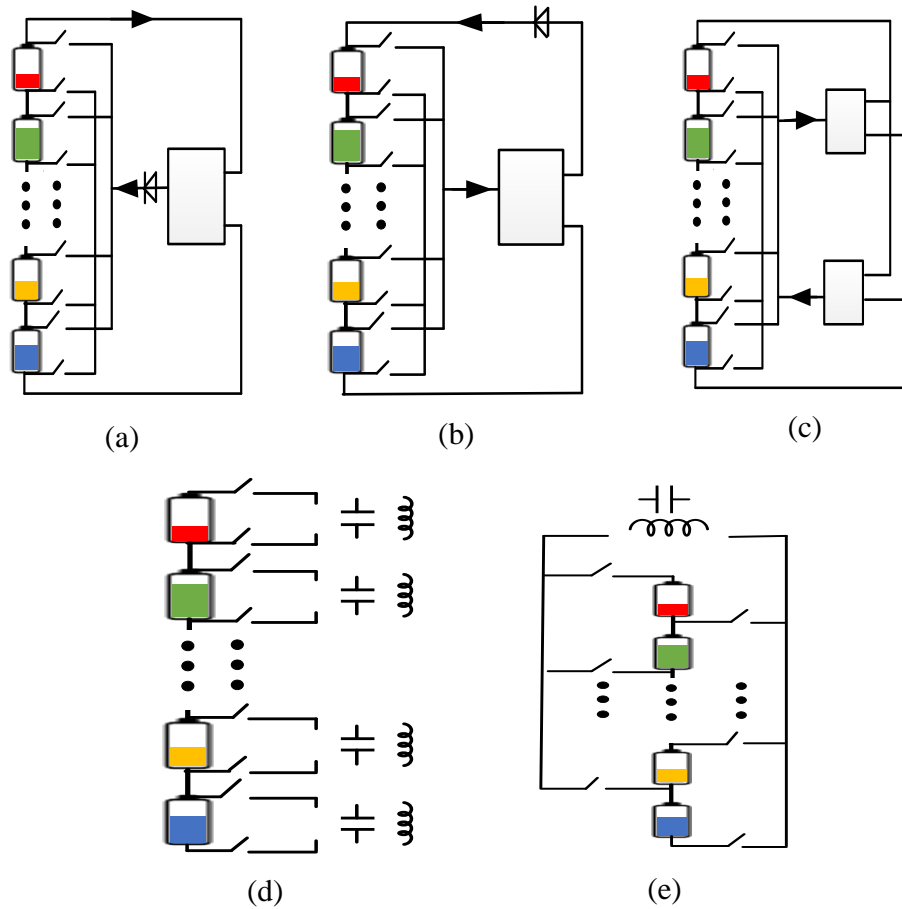
FIGURE 2.19: Simple model of active balancing methods. (a) pack-
to-cell, (b) cell-to-pack, (c) cell-to-pack-to-cell method, (d) adjacent
cell-to-cell, (e) direct cell-to-cell.

switch is very large. In addition, energy is transferred from a cell with higher charge

to the pack. Then it is transferred from the pack to a cell with lower charge. Since

it requires two energy transfer processes to balance the cells, the efficiency of these

methods is not good due to the losses associated with the energy transfer. However,

it still needs a lot of photo-couplers to drive the bidirectional switches and two DC–

DC converters, it is complex and expensive to implement.

The cell-to-cell balancing methods show a fair performance when compared to the

above methods. There are several topologies developed based on the cell-to-cell
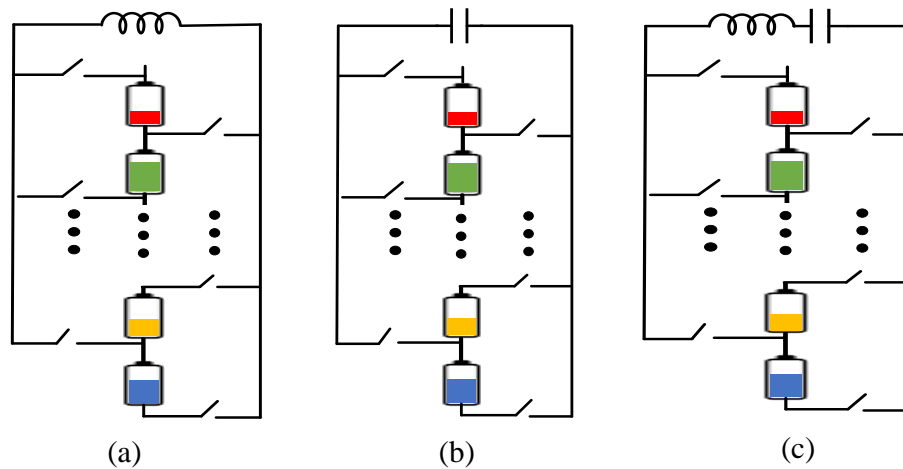
FIGURE 2.20: conventional direct cell-to-cell methods. (a) single inductor, (b) single capacitor, (c) LC resonant.

balancing method. They include two kinds of method as the adjacent cell-to-cell methods and the direct cell-to-cell methods. The adjacent cell-to-cell method transfers the charge between two adjacent cells through the capacitors, the inductors, or a combination of the two as a resonant tank [94]-[101]. The methods require a lot of passive components such as inductors and capacitors. The switches are driven using pulse transformers, photo-couplers, or gate driver and power supply. Therefore, the methods is high in cost and complex in implementation. they exhibit low efficiency in a battery pack due to the fact that the energy needs to be transferred into several adjacent cells.

The direct cell-to-cell method is developed to transfer the charge directly from any cell to any cell to get high efficiency. In this method, because the single switched capacitor [102] or single switched inductor [103] is used as a media for the charge transfer, the method is easier to implement but the charge and discharge are processed separately each half cycle with hard-switching. The cell-to-cell LC resonant

topology in [104] can achieve higher efficiency due to the soft-switching operation. However, the charge and discharge are still processed separately each half cycle. The large number of switches and gate drivers are still required to implement the bidirectional switches.

In summary, each above method or typology has the different advantages and remaining issues. It is clear that most of the balancing methods require lots of photocouplers or pulse transformers to drive the switches. It is high cost and complexity in the implementation. In addition, faster balancing can help the battery pack utilize the capacity. Also, higher efficiency result lower hit and smaller cooling system. Therefore, the balancing circuit need to be improve for more simple design, higher-balancing speed and efficiency.

2.4   Remaining Issues and Research Target

Hybrid energy storage (HES) systems using the TAB converter, which connect storage with grid/bus, and/or different types of renewable energies, have bee summarized. The advantage and challenges of each application are summarized, as shown in Table 2.1. For each application, the TAB converter contributes to the different targets to develop conventional systems. The power control of the TAB converter for the HES systems is setup based on the voltage and current at each port terminal. There are many type of the storage with different voltage variation. Also, the battery pack of each HES system has a different voltage level. Therefore, the voltage variation need to be considered in the design of the TAB converter.

Also, lithium-ion battery pack, which is used in many HES systems, is consisted

of many cells connected in series and parallel to provide enough energy and volt-

age. The unbalanced voltage between the cells in a battery pack reduce the safety

and usable capacity of the battery pack. Also, some cells may be overcharge volt-

age, which is very critical for the lithium-ion battery. It affects the safety of the HES

system. In order to apply the TAB converter effectively, the balancing circuit is pro-

posed for HES systems. Many balancing method and typologies are summarised,

as shown in Table 2.2. However, almost active methods is complexity and high cost

in implementation and control.

TABLE 2.2: Summary of the conventional balancing methods.

Balancing method		Component counts						Characteristics
		Switch	Photo-coupler/ pulse Trans.	Diode	Ind.	Cap.	Trans.	
Cell-to-pack		2N	2N	2N-2	0	0	m	Requires many steps to balance causing a slow balancing speed, especially for the low voltage cells.
Pack-to-cell		2N*	2N	m+1	0	0	m+1	Requires many steps to balance causing a slow balancing speed, especially for the high voltage cells.
Cell-to-pack-to-cell		2N*	2N	2	0	0	2	Faster than the cell-to-pack and pack-to-cell methods, but still takes a long time to balance the cells.
Adjacent cell-to-cell	Switched Cap.	4N	4N	0	0	N	0	The charge is transferred many cells.
	Improved switched Cap.	N+2*	N+2	0	0	N+1	0	
	Switched inductor	2N	2N	0	N	0	0	
	Quasi-resonant	2N	2N	0	2N	N	0	
Direct cell-to-cell	Single Cap.	N+1*	N+1	0	0	1	0	The charge and discharge are processed separately in half switching cycle.
	Single Ind.	2N	2N	2N	1	0	0	
	LC resonant	N+10*	N+10	0	1	1	0	

N: number of cells, m: number of module, *: bidirectional switch, Ind.: inductor, Cap.: capacitor, Trans.: transformer

Chapter 3

Design Procedure of Triple Active Bridge Converter

This chapter proposes a design procedure for the TAB converter. The voltage variations and inductances are normalized based on percentage, and the complicated relationships between the elements of the TAB converter are clarified [105]-[106]. The limitation of inductances corresponding to the different voltage variations is specified. The inductances are designed by considering the operation range of the phase shift angles. The design procedure is applied to design the TAB converter for a household renewable energy system rated at 400 V and 10 kW. A prototype converter rated at 200 V and 500 W is implemented to verify the proposed method. The experimental phase shift angles are close to the calculated values. Then, the TAB converter can operate under the rated power for all operation modes. It indicates that the proposed method can be applied for the design of the TAB converter in various applications.

3.1   Parameters and Normalization

3.1.1   Primary-referred Parameters

Figure 3.1 shows the connection of the TAB converter to three main parts of the household renewable energy system. The rooftop PV is connected to the primary side. The secondary side connects to the DC grid and load. The EVs is connected to the tertiary side of the TAB converter.
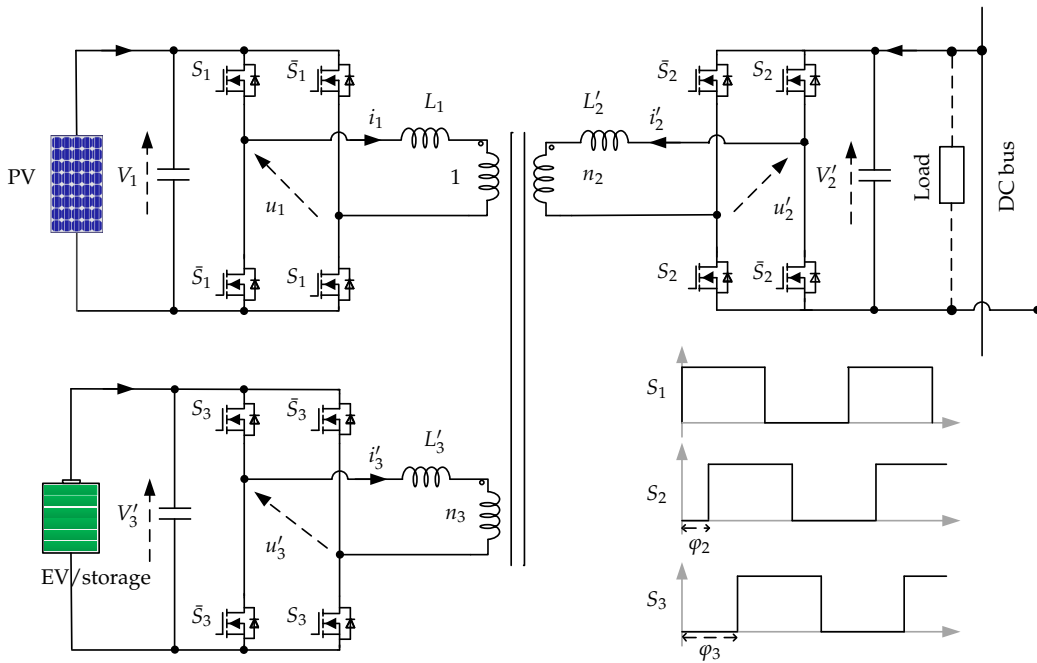
FIGURE 3.1: TAB converter for household renewable energy system.

As shown in Figure 3.1, n_2 is the turn ratio of the secondary side compared to the primary side of the transformer. It is also similar to the tertiary side, which is shown as n_3. The series inductances, L_1, L_2', and L_3' include the external inductance and leakage inductance on each side. The phase leg midpoint voltages u_1, u_2', and u_3' have the amplitudes V_1, V_2', and V_3', respectively.

The direction and amplitude of each port's power are controlled by the phase

shift between the gate signals of the ports. Thus, the gate signal of the primary port

keeps the phase shift angle at zero, whereas the phase shift angle of the gate signal

on the secondary side, φ_2, and the tertiary side, φ_3, are changed.

Figure 3.2 shows Y-type and Δ-type equivalent circuits of the TAB converter, respectively [54]. The voltages and currents of the secondary side and tertiary side

refer to the port-1 as the following equation.

(a)   (b)
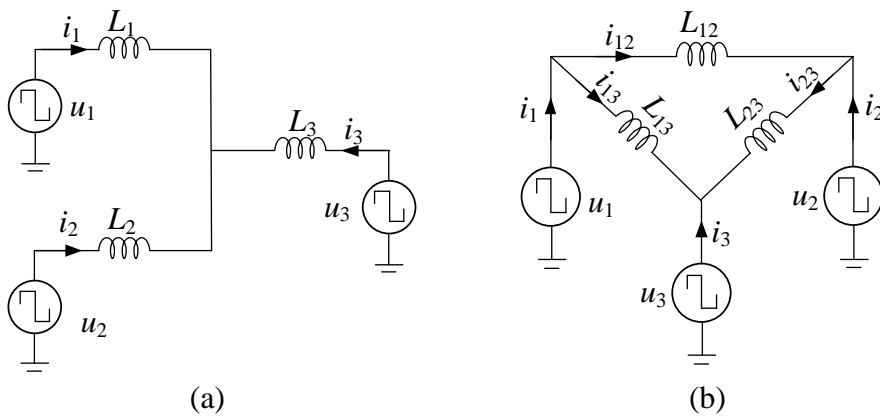
FIGURE 3.2: Primary-referred model of the TAB converter. (a) Y-type primary-referred equivalent circuit, (b) Δ-type primary-referred equivalent circuit.

$$\begin{cases} u_2 = u_2'/n_2 \\ u_3 = u_3'/n_3 \\ i_2 = i_2'n_2 \\ i_3 = i_3'n_3 \end{cases} \tag{3.1}$$

where u_2 and u_3 are the primary-referred voltages, and i_2 and i_3 are the primary-referred currents, respectively. Thus, it has the following equation.

$$\begin{cases} L_2 = L_2'/n_2^2 \\[2ex] L_3 = L_3'/n_3^2 \\[2ex] V_2 = V_2'/n_2 \\[2ex] V_3 = V_3'/n_3 \end{cases} \tag{3.2}$$

where L_2 and L_3 are primary-referred inductances, and V_2 and V_3 are primary-referred voltage amplitudes, respectively.

The primary-referred inductances and voltages are then used for the power calculation. The power of each port is formulated in the equations below.

$$P_1 = \frac{V_1 V_2 \varphi_2 (\pi - |\varphi_2|) L_3 + V_1 V_3 \varphi_3 (\pi - |\varphi_3|) L_2}{2\pi^2 f (L_1 L_2 + L_2 L_3 + L_3 L_1)} \tag{3.3}$$

$$P_2 = \frac{V_2 V_1 (-\varphi_2)(\pi - |\varphi_2|) L_3 + V_2 V_3 (\varphi_3 - \varphi_2)(\pi - |\varphi_3 - \varphi_2|) L_1}{2\pi^2 f (L_1 L_2 + L_2 L_3 + L_3 L_1)} \tag{3.4}$$

$$P_3 = \frac{V_3 V_1 (-\varphi_3)(\pi - |\varphi_3|) L_2 + V_3 V_2 (\varphi_2 - \varphi_3)(\pi - |\varphi_2 - \varphi_3|) L_1}{2\pi^2 f (L_1 L_2 + L_2 L_3 + L_3 L_1)} \tag{3.5}$$

Where f denotes the switching frequency, and P_1, P_2, and P_3 are the transmission power of the primary, secondary, and tertiary sides, respectively.

3.1.2 Normalized Parameters

The normalization method is proposed to The normalization method is proposed to design the inductances of the TAB converter. The inductance, voltages, and power of the converter are standardized based on the rated values. The voltage variations

and power transmission are normalized in terms of percentage. The inductances are then calculated based on the percentage of the rated equivalent inductance, which can be used to design the TAB converter for many different voltages and power ratings in other applications.
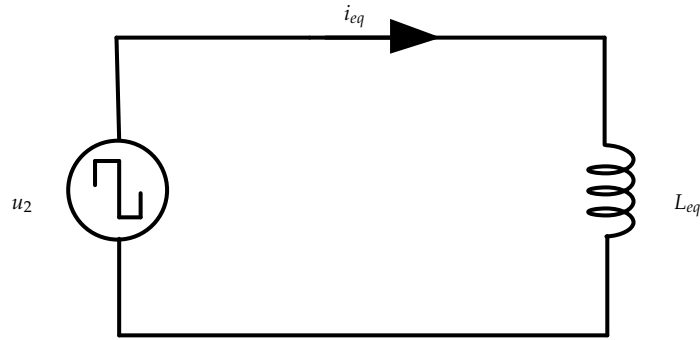
FIGURE 3.3: Simple equivalent circuit of TAB converter.

Figure 3.3 shows an equivalent circuit for a TAB converter. It includes a source u_2 and inductance L_{eq}. where L_{eq} is the rated equivalent inductance, which is represented as the total load of the converter. Voltage u_2 has the amplitude as V_2. For Z_{eq} is rated equivalent impedance of the equivalent circuit. For $Z_{eq} = 2\pi f L_{eq}$, it has the following.

$$Z_{eq} = \frac{V_2^2}{P_r} \tag{3.6}$$

Where P_r is the rated power. Therefore, the relationships among the rated power, voltage, rated equivalent current i_{eq}, and rated equivalent inductance L_{eq} are shown in the following equation.

$$L_{eq} = \frac{V_2^2}{2\pi f P_r} \tag{3.7}$$

$$i_{eq} = \frac{V_2}{Z_{eq}} = \frac{V_2}{\omega L_{eq}} \tag{3.8}$$

For the tertiary voltage, V_3 varies from the minimum voltage V_{3min} to the maximum voltage V_{3max}. It has a relationship with the rated voltage through the following equations.

$$V_{3\%} = 100\frac{V_3}{V_2} \quad [\%] \tag{3.9}$$

$$V_{1\%} = 100\frac{V_1}{V_2} \quad [\%] \tag{3.10}$$

where $V_{1\%}$ and $V_{3\%}$ are the voltage of the primary side and tertiary side in percentage, respectively. It has the following relationship.

$$V_{1\%} = 100\frac{V_1}{V_2'}n_2 \quad [\%] \tag{3.11}$$

$$V_{3\%} = 100\frac{V_3'}{V_2'}\frac{n_2}{n_3} \quad [\%] \tag{3.12}$$

For the sake of simplicity of the calculation, the primary-referred inductances, L_1, L_2, or L_3, are simplified as the same. If the primary-referred inductances are different, the proposed method can be used. The detailed explanation will be shown in the next section.

$$L_1 = L_2 = L_3 = L \tag{3.13}$$

$$L_{\%} = 100\frac{L}{L_{eq}} \quad [\%] \tag{3.14}$$

where $L_\%$ is the normalized inductance, which is a percentage of the primary-referenced inductance to the rated equivalent inductance. The normalized inductance can be designed based on the voltage variations and phase shift of the operating area.

3.2 Design of Inductances in the TAB Converter

3.2.1 Inductance Calculation

This section describes the normalized inductance calculation when the voltages of the primary and tertiary ports vary. It is considered for $V_2 \geq V_{1min} \geq V_{3min}$. Thus, $P_1 = P_r$ and $P_3 = -P_r$, where $P_2 = 0$ is the most critical operation point because the phase shift of the tertiary port φ_3 is at maximum, as shown in Figure 3.4. Figure 3.4(a) shows the phase shift operating area when voltage of three port are 100%. The phase shift angle of the design point is moved in considering the variation voltage as shown in Figure 3.4(b).

This is discussed for the range of phase shift in φ_2 and φ_3 from zero to $\pi/2$. The powers change the direction within the range of phase shift from $-\pi/2$ to zero. First, it is necessary to satisfy the following equation for $P_2 = 0$.

$$V_2 V_1(-\varphi_2)\,(\pi - |\varphi_2|) + V_2 V_3(\varphi_3 - \varphi_2)(\pi - |\varphi_3 - \varphi_2|) = 0 \tag{3.15}$$

or

$$V_1\,(\varphi_2)\,(\pi - |\varphi_2|) = V_3(\varphi_3 - \varphi_2)(\pi - |\varphi_3 - \varphi_2|) \tag{3.16}$$

Using the sinusoidal and linear approximation, the following is derived.
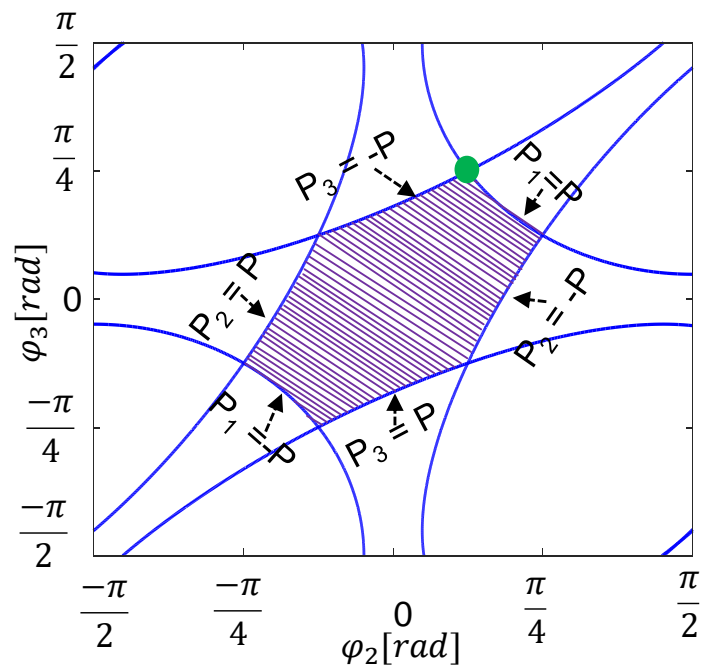
(a)
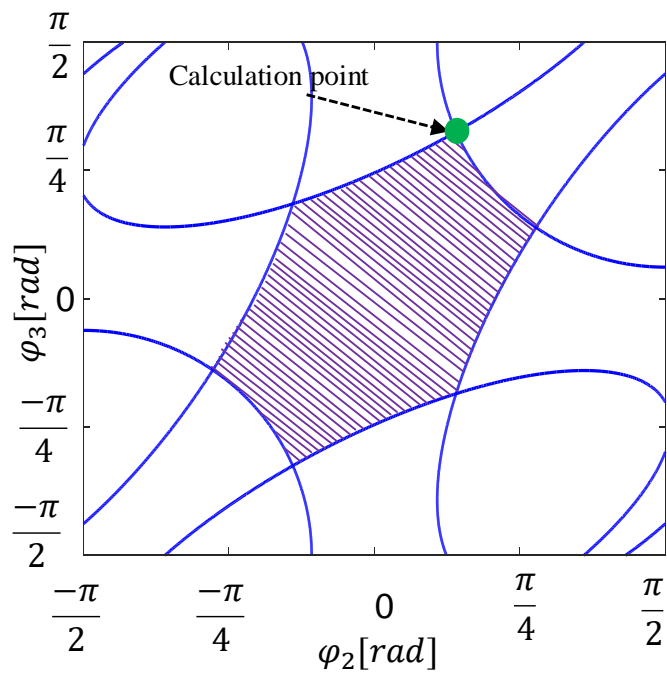
(b)

FIGURE 3.4: Calculation of inductance in considering the critical operation point. (a) voltage of three port are 100%, (b) voltage of one port is 80%

$$\varphi_2 \left(\pi - |\varphi_2| \right) \cong \frac{8}{\pi} \varphi_2 \tag{3.17}$$

$$(\varphi_3 - \varphi_2) \left(\pi - |\varphi_3 - \varphi_2| \right) \cong \frac{8}{\pi} (\varphi_3 - \varphi_2) \tag{3.18}$$

where $0 < \varphi_2 < \frac{\pi}{4}$ and $0 < \varphi_3 - \varphi_2 < \frac{\pi}{4}$. From (3.16)–(3.18), the following can be approximated:

$$V_1 \varphi_2 = V_3 (\varphi_3 - \varphi_2) \tag{3.19}$$

or

$$\varphi_2 = \frac{V_3}{V_1 + V_3} \varphi_3 \tag{3.20}$$

This indicates that the voltage variation effects the relationship between φ_2 and φ_3. Applying the condition $P_2 = 0$ by (3.20) to the equation of power of the primary port P_1, the following equation is derived:

$$P_t = \frac{V_1 V_2 \frac{V_3}{V_1 + V_3} \varphi_3 \left(\pi - \frac{V_3}{V_1 + V_3} \varphi_3 \right) + V_1 V_3 \varphi_3 (\pi - \varphi_3)}{6\pi^2 f L} \tag{3.21}$$

where P_1 is replaced by P_t as the transmission power. Then it has the following.

$$P_t = \frac{V_1 V_2 \varphi_3}{6\pi^2 f L} \left[\frac{V_3}{V_1 + V_3} \pi - \left(\frac{V_3}{V_1 + V_3} \right)^2 \varphi_3 + \frac{V_3}{V_2} \pi - \frac{V_3}{V_2} \varphi_3 \right] \tag{3.22}$$

or

$$P_t = \frac{V_1 V_2}{6\pi^2 f L} \varphi_3 \left\{ \left(\frac{V_3}{V_1 + V_3} + \frac{V_3}{V_2} \right) \pi \right.$$
$$\left. - \left[\left(\frac{V_3}{V_1 + V_3} \right)^2 + \frac{V_3}{V_2} \right] \varphi_3 \right\} \tag{3.23}$$

Using $V_{1\%}$ and $V_{3\%}$ for the above equation, it has the following.

$$
\begin{aligned}
L \;=\; & \frac{V_2^2}{100}\frac{V_{1\%}}{6\pi^2 f P_t}\varphi_3\left\{\left(\frac{V_{3\%}}{V_{1\%}+V_{3\%}}+\frac{V_{3\%}}{100}\right)\pi\right. \\
& \left. -\left[\left(\frac{V_{3\%}}{V_{1\%}+V_{3\%}}\right)^2+\frac{V_{3\%}}{100}\right]\varphi_3\right\}
\end{aligned}
\tag{3.24}
$$

or

$$
L \;=\; \frac{V_2^2}{100}\frac{V_{1\%}V_{3\%}}{6\pi^2 f P_t}\varphi_3\left(A\pi-B\varphi_3\right)
\tag{3.25}
$$

where A and B are calculated as the following.

$$
\begin{cases}
A = \frac{1}{V_{1\%}+V_{3\%}}+\frac{1}{100} \\[2ex]
B = \frac{V_{3\%}}{(V_{1\%}+V_{3\%})^2}+\frac{1}{100}
\end{cases}
\tag{3.26}
$$

From (3.7), (3.14), and (3.24)-(3.26), the relationship between the normalized inductance and phase shift of the tertiary port at the rated power ($P_t = P_r$) is shown in the following.

$$
L_{\%} = \frac{V_{1\%}V_{3\%}}{3\pi}\varphi_3\left(A\pi-B\varphi_3\right)\qquad [\%]
\tag{3.27}
$$

The solution to (3.27) shows the relationship between the normalized inductance, phase shift, and voltage variations. Figure 3.5 demonstrates the limitation of inductance $L_{\%max}$ corresponding to different voltage variations according to (3.27), where the phase shift is at maximum as $\varphi_3 = \pi/2$. The secondary and tertiary sides' voltages are drawn from 70% to 120% depending on the application. This indicates that the limitation of the inductance is specified for different voltage variations.

According to (3.27), by determining the maximum phase shift operation, the inductance is designed directly depending on the voltage variations of the application.
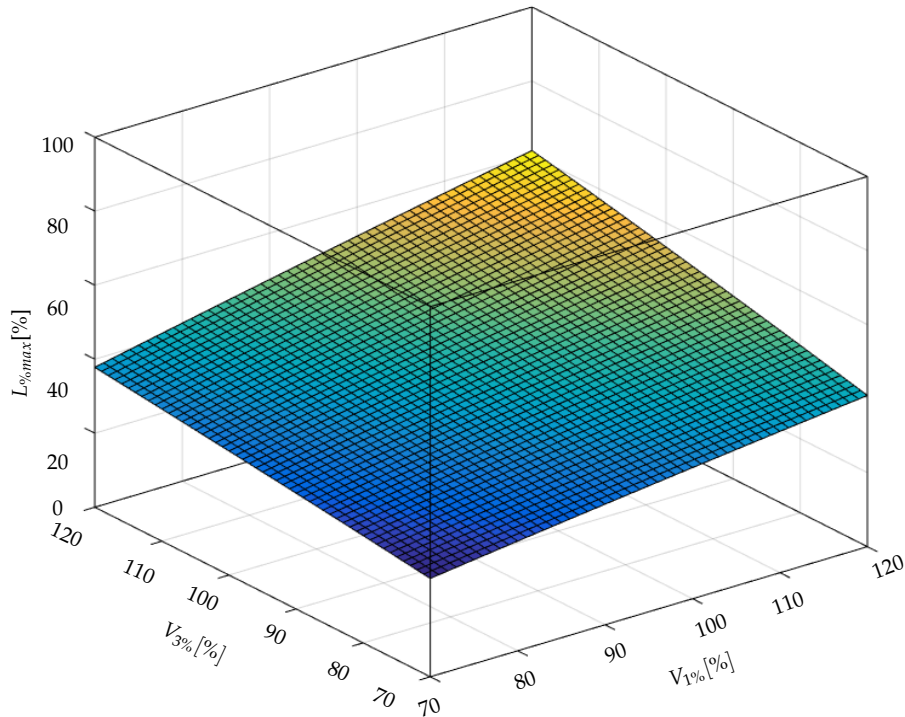
FIGURE 3.5: Limitation of normalized inductance $L_{\%max}$ corresponding to different voltage variations $V_{1\%}$ and $V_{3\%}$.

For an application in which the voltages of the three ports are the same as follows.

$$L_{\%} = \frac{100}{12\pi} \, \varphi_3 \left(6\pi - 5\varphi_3\right) \qquad [\%] \tag{3.28}$$

It can also be applied to an application that has one voltage variation. For example, only the tertiary voltage has a variation, and thus the normalization is calculated as follows.

$$L_{\%} = \frac{100}{3\pi} V_{3\%} \varphi_3 \left(A\pi - B\varphi_3\right) \qquad [\%] \tag{3.29}$$

3.2.2   Transmission Power and Current of Inductance

Transmission Power

In the operation of the TAB converter, the transmission power P_t changes depending on the voltage variations and phase shift angles.

$$P_\% = 100 \frac{P_t}{P_r} \quad [\%] \tag{3.30}$$

where $P_\%$ is the normalized power, which is the percentage of the transmission and rated power. The relationship between inductance, voltage variations, and power is as follows:

$$L_\% = 100 \frac{V_{1\%} V_{3\%}}{3\pi P_\%} \varphi_3 \left(A\pi - B\varphi_3 \right) \quad [\%] \tag{3.31}$$

The transmission power can be viewed as depending on the voltage variations at the designed inductance through the following.

$$P_\% = 100 \frac{V_{1\%} V_{3\%}}{3\pi L_\%} \varphi_3 \left(A\pi - B\varphi_3 \right) \quad [\%] \tag{3.32}$$

Current of Inductance

The current of the inductance is analyzed for mode 1-2 that is one of the most critical condition. It can be applied as the same for other conditions. Based on the Δ-type

primary-referred equivalent circuit Figure 3.2, the instant value of inductance currents in the steady state condition i_{12}, i_{13}, i_{23} are as follows.

$$
\begin{cases}
i_{12}(\varphi) = \frac{u_1 - u_2}{\omega L_{12}} \varphi + i_{12}(0) \\[2mm]
i_{13}(\varphi) = \frac{u_1 - u_3}{\omega L_{13}} \varphi + i_{13}(0) \\[2mm]
i_{23}(\varphi) = \frac{u_2 - u_3}{\omega L_{23}} \varphi + i_{23}(0)
\end{cases}
\tag{3.33}
$$

where $i_{12}(0)$, $i_{13}(0)$, and $i_{23}(0)$ are the value of the each inductance current at beginning switching cycles in steady state operation, respectively. φ are the phase at the calculation point.

$$
\varphi = \omega t
\tag{3.34}
$$

and ω is angular frequency, which is defined as follow.

$$
\omega = 2\pi f
\tag{3.35}
$$

It is considered for the condition $0 \leq \varphi_2 \leq \varphi 3 \leq \pi/2$. The analysis for the other conditions can be applied similarly. Figure 3.6 shows the simulation voltage and current waveform of this condition. In one switching cycle, it is defined by six states from 0 to 2π. The value from π to 2π is the negative of the value from 0 to π. Therefore, the currents are analyzed in three states I, II, and III. Because u_1, u_2, and u_3 are square voltage as $\pm$ primary-referred voltage of each port, the instant value of currents can be calculated separately for each state.
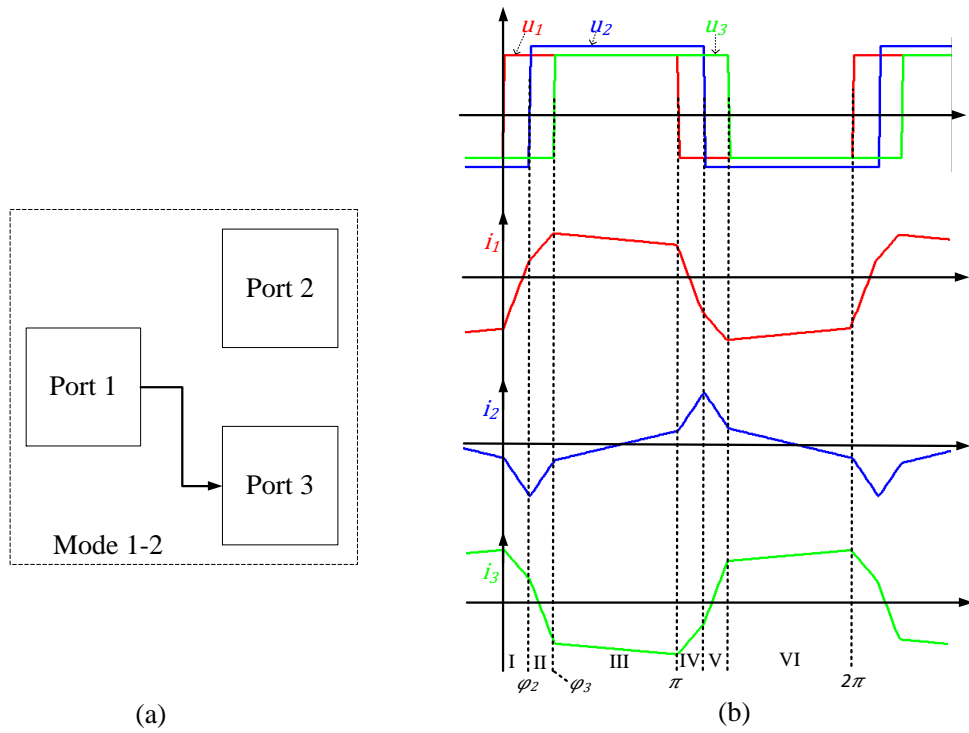
FIGURE 3.6: Steady state current and voltage waveform in mode 1-2.
(a) Operating condition, (b) Voltage and current waveform.

In state I, $0 \leq \varphi \leq \varphi_2$, the inductance currents is as following equation.

$$
\begin{cases}
i_{12}(\varphi) = \frac{V_1 + V_2}{\omega L_{12}} \varphi + i_{12}(0) \\[2mm]
i_{13}(\varphi) = \frac{V_1 + V_3}{\omega L_{13}} \varphi + i_{13}(0) \\[2mm]
i_{23}(\varphi) = \frac{V_3 - V_2}{\omega L_{23}} \varphi + i_{23}(0)
\end{cases}
\tag{3.36}
$$

In state II, $\varphi_2 < \varphi \leq \varphi_3$, the inductance currents is as following equation.

$$
\begin{cases}
i_{12}(\varphi) = \frac{V_1 - V_2}{\omega L_{12}} (\varphi - \varphi_2) + i_{12}(\varphi_2) \\[2mm]
i_{13}(\varphi) = \frac{V_1 + V_3}{\omega L_{13}} (\varphi - \varphi_2) + i_{13}(\varphi_2) \\[2mm]
i_{23}(\varphi) = \frac{V_3 + V_2}{\omega L_{23}} (\varphi - \varphi_2) + i_{23}(\varphi_2)
\end{cases}
\tag{3.37}
$$

In state III, $\varphi_3 < \varphi \le \pi$, the inductance currents is as following equation.

$$
\begin{cases}
i_{12}(\varphi) = \frac{V_1-V_2}{\omega L_{12}}(\varphi - \varphi_3) + i_{12}(\varphi_3) \\[2mm]
i_{13}(\varphi) = \frac{V_1-V_3}{\omega L_{13}}(\varphi - \varphi_3) + i_{13}(\varphi_3) \\[2mm]
i_{23}(\varphi) = \frac{V_2-V_3}{\omega L_{23}}(\varphi - \varphi_3) + i_{23}(\varphi_3)
\end{cases}
\tag{3.38}
$$

The half-cycle end at $\varphi = \pi$. It has the following equation.

$$
\begin{cases}
-i_{12}(0) = i_{12}(\pi) \\[2mm]
-i_{13}(0) = i_{13}(\pi) \\[2mm]
-i_{23}(0) = i_{23}(\pi)
\end{cases}
\tag{3.39}
$$

Solving (3.39), the dynamic inductance currents are obtained at any phase shift angle by (3.36)-(3.38). From (3.36)-(3.39), it has the following equation.

$$
\begin{cases}
-i_{12}(0) = \frac{V_1-V_2}{\omega L_{12}}(\pi - \varphi_2) + \frac{V_1+V_2}{\omega L_{12}}\varphi_2 + i_{12}(0) \\[2mm]
-i_{13}(0) = \frac{V_1-V_3}{\omega L_{13}}(\pi - \varphi_3) + \frac{V_1+V_3}{\omega L_{13}}\varphi_3 + i_{13}(0) \\[2mm]
-i_{23}(0) = \frac{V_2-V_3}{\omega L_{23}}(\pi - \varphi_3) + \frac{V_3+V_2}{\omega L_{23}}(\varphi_3 - \varphi_2) + \frac{V_3-V_2}{\omega L_{23}}\varphi_2 + i_{23}(0)
\end{cases}
\tag{3.40}
$$

Therefore, the following equation is obtained.

$$
\begin{cases}
-2i_{12}(0) = \frac{1}{\omega L_{12}}[(V_1 - V_2)(\pi - \varphi_2) + (V_1 + V_2)\varphi_2] \\[2mm]
-2i_{13}(0) = \frac{1}{\omega L_{13}}[(V_1 - V_3)(\pi - \varphi_3) + (V_1 + V_3)\varphi_3] \\[2mm]
-2i_{23}(0) = \frac{1}{\omega L_{23}}[(V_2 - V_3)(\pi - \varphi_3) + (V_3 + V_2)(\varphi_3 - \varphi_2) + (V_3 - V_2)\varphi_2]
\end{cases}
\tag{3.41}
$$

$$
\begin{cases}
i_{12}(0) = \frac{-1}{2\omega L_{12}}[V_1\pi - V_2(\pi - 2\varphi_2)] \\[2mm]
i_{13}(0) = \frac{-1}{2\omega L_{13}}[(V_1\pi - V_3(\pi - 2\varphi_3)] \\[2mm]
i_{23}(0) = \frac{-1}{2\omega L_{23}}[(V_2(\pi - 2\varphi_2) - V_3(\pi - 2\varphi_3)]
\end{cases}
\tag{3.42}
$$

The inductance current of port 2,i_2, is the most critical in the operation mode 1-2,

as shown in Figure 3.6. The peak current, which is highest at $\varphi = \varphi_2$, is calculated by the following equation.

$$i_2(\varphi_2) = i_{23}(\varphi_2) - i_{12}(\varphi_2) \tag{3.43}$$

$$i_2(\varphi_2) = \frac{V_3 - V_2}{\omega L_{23}}\varphi_2 + i_{23}(0) - \frac{V_1 + V_2}{\omega L_{12}}\varphi_2 - i_{12}(0) \tag{3.44}$$

$$
\begin{aligned}
i_2(\varphi_2) \quad = \quad & \frac{V_3 - V_2}{2\omega L_{23}}2\varphi_2 - \frac{1}{2\omega L_{23}}[(V_2(\pi - 2\varphi_2) - V_3(\pi - 2\varphi_3)] \\
& - \frac{V_1 + V_2}{2\omega L_{12}}2\varphi_2 + \frac{1}{2\omega L_{12}}[V_1\pi - V_2(\pi - 2\varphi_2)]
\end{aligned}
\tag{3.45}
$$

For the sake of simplicity of the calculation, the primary-referred inductances, L_1, L_2, or L_3, are simplified as the same.

$$L_1 = L_2 = L_3 = L \tag{3.46}$$

Therefore, the primary-referred inductances in the Δ model of three-port are the same as the following equation.

$$L_{12} = L_{13} = L_{23} = 3L \tag{3.47}$$

Therefore, (3.45) is defined as the following equation.

$$i_2(\varphi_2) = \frac{V_1(\pi - 2\varphi_2) - 2V_2\pi + V_3(\pi + 2\varphi_2 - 2\varphi_3)}{6\omega L} \tag{3.48}$$

Using $V_{1\%}$, $V_{3\%}$, and $L_\%$ for (3.45), the effect of the voltage variation and turn ratio is as the following equation.

$$i_2(\varphi_2) = \frac{V_2}{100} \frac{V_{1\%}(\pi - 2\varphi_2) - 200\pi + V_{3\%}(\pi + 2\varphi_2 - 2\varphi_3)}{\frac{6\omega L_\% L_{eq}}{100}} \qquad (3.49)$$

From (3.49) and (3.8), The normalized current of inductance in secondary port in percentage is as following.

$$i_{2\%}(\varphi_2) = 100 \frac{V_{1\%}(\pi - 2\varphi_2) - 200\pi + V_{3\%}(\pi + 2\varphi_2 - 2\varphi_3)}{6L_\%} \ [\%] \qquad (3.50)$$

3.2.3 Design Process

This part proposes the design process for inductances in a TAB converter using the normalization design method. The design of the inductance is the trade-off between power transmission and performance. Here, the limitation and range of the phase shift angles, power transmission, and peak current are considered. Further consideration can be applied more in the future.

Figure 3.7 shows a flowchart of the design process. First, the rated power and voltage ranges of the converter are listed. After that, the voltages and inductances of the secondary and tertiary sides are referred to the primary side from the transformer turn ratio by (3.2). Therefore, the proposed method can be applied if the turn ratios are different. The rated voltage is decided. Thus, equivalent inductance is calculated by (3.7). The voltage variations in percentage are shown as (3.9) and (3.10). By applying (3.26) and (3.27), the normalized inductance $L_\%$ is shown in relationship to the phase shift angle and voltage variation.
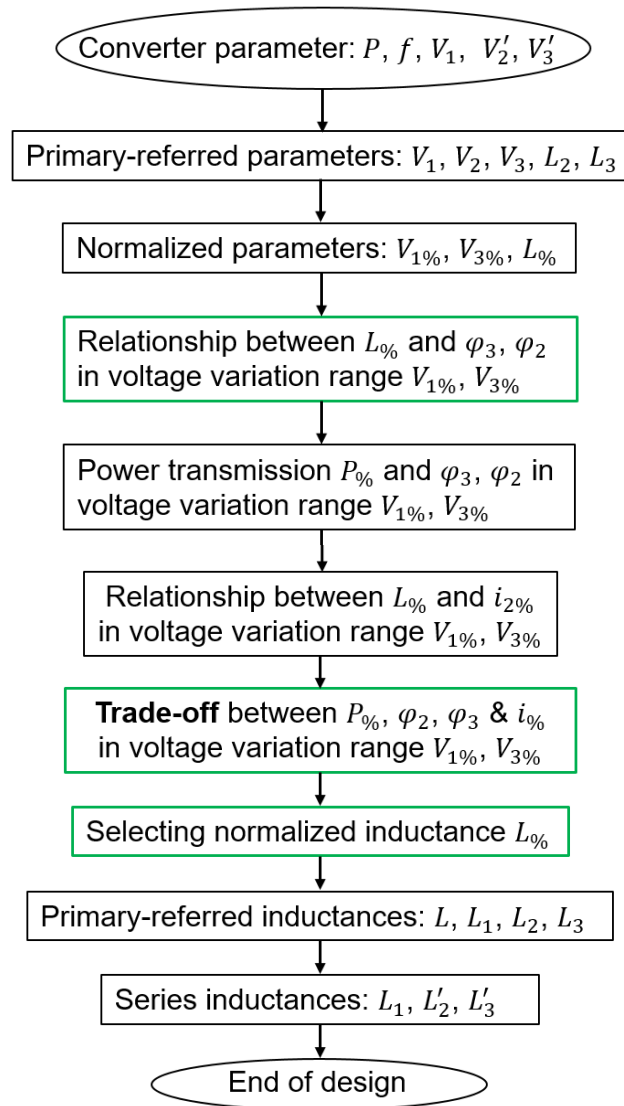
FIGURE 3.7: Design process of inductances in the TAB converter.

Then, the power transmission, phase shift operating area, and the peak of induc-

tance current are considered for the inductance design trade-off. By selecting the

design point for the rated phase shift operation range, $L_\%$ is determined. The design

is based on the most critical aspect of the operation, and thus it makes certain that

the converter can operate in all working modes. The primary-referred inductance

is calculated according to (3.13) and (3.14). If the primary-referred inductances are

different, L_2 and L_3 are calculated by the next part in the detail. Based on the transformer turn ratio n_2 and n_3, the series inductances in the secondary and tertiary ports, L_2' and L_3' of the TAB converter are computed from (3.2).

3.2.4 Design of Inductances in TAB Converter if Primary-referred Inductances are Different

If the primary-referred inductances, L_1, L_2, and L_3, are different, $L_1 \neq L_2 \neq L_3$, the equation (3.20) is updated as the following.

$$\varphi_2 = \frac{V_3 L_1}{V_1 L_3 + V_3 L_1} \varphi_3 \tag{3.51}$$

Therefore, the equation (3.21) is updated as the following.

$$P_t = \frac{V_1 V_2 \frac{V_3 L_1 \varphi_3}{V_1 L_3 + V_3 L_1} (\pi - \frac{V_3 L_1 \varphi_3}{V_1 + V_3}) L_3 + V_1 V_3 \varphi_3 (\pi - \varphi_3) L_2}{2\pi^2 f (L_1 L_2 + L_2 L_3 + L_3 L_1)} \tag{3.52}$$

Then, it results in the following.

$$
\begin{aligned}
P_t = {} & \frac{V_1 V_2}{2\pi^2 f (L_1 L_2 + L_2 L_3 + L_3 L_1)} \varphi_3 \left\{ \left(\frac{V_3 L_1 L_3}{V_1 L_3 + V_3 L_1} \right. \right. \\
& + \left. \frac{V_3 L_2}{V_2} \right) \pi - \left[\left(\frac{V_3 L_1}{V_1 L_3 + V_3 L_1} \right)^2 L_3 + \frac{V_3 L_2}{V_2} \right] \varphi_3 \Bigg\}
\end{aligned} \tag{3.53}
$$

Using $V_{1\%}$ and $V_{3\%}$ for the above equation at rated power, $P_t = P_r$, it has the following.

$$
\begin{aligned}
P_r = {} & \frac{V_2^2}{100} \frac{V_{1\%} \varphi_3}{2\pi^2 f (L_1 L_2 + L_2 L_3 + L_3 L_1)} \left\{ \left(\frac{V_{3\%} L_1 L_3}{V_{1\%} L_3 + V_{3\%} L_1} \right. \right. \\
& + \left. \frac{V_{3\%} L_2}{100} \right) \pi - \left[\left(\frac{V_{3\%} L_1}{V_{1\%} L_3 + V_{3\%} L_1} \right)^2 L_3 + \frac{V_{3\%} L_2}{V_2} \right] \varphi_3 \Bigg\}
\end{aligned} \tag{3.54}
$$

Equation (3.54) has four variables, L_1, L_2, L_3, and φ_3. The proposed method can be applied as the following. Firstly, the design process is used to design the

normalized inductance,$L_\%$, as shown in Figure 3.7. After designing the normalized inductance $L_\%$, the inductance of one port, for example, inductance of primary port, is the same as L.

$$L_1 = L \tag{3.55}$$

Because L_1 and φ_3 were already decided, equation (3.54) has only two variables as L_2 and L_3. Therefore, L_2 and L_3 can be decided based on (3.54). Then, L_2' and L_3' are calculated by (3.2).

3.3 Applying the Design Method for the TAB Converter in a Household Renewable Energy System Rated at 400 V and 10 kW

The proposed design method is applied to a TAB converter design for a household

renewable energy system rated at 400 V and 10 kW, as shown in Figure 3.8.
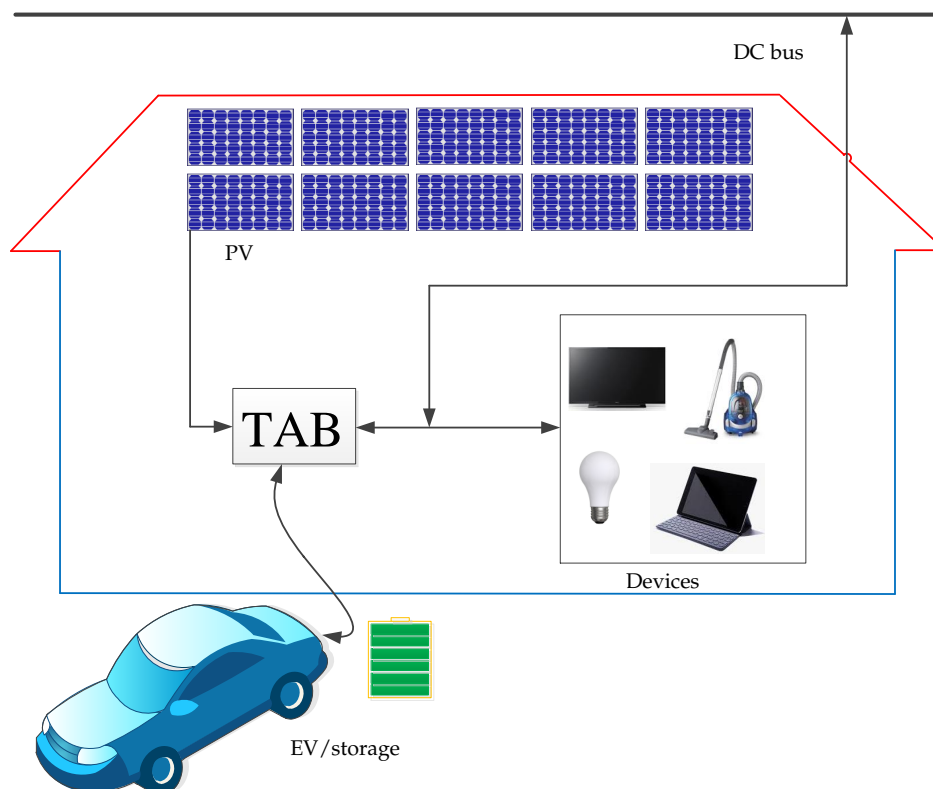
FIGURE 3.8: Household renewable energy system configuration.

The battery voltage, which connects to tertiary port varies from 340 to 440 V.

The voltage range of the PV is also from 340 to 440 V. Table 3.1 shows the circuit

parameters. The switching frequency of the TAB converter is within the range of 20

to 100 kHz.

The primary-referred parameters are shown in Table 3.2. In this application, the

TABLE 3.1: Parameters of TAB Converter for Household Renewable Energy System

Elements	Symbol	Parameter
Rated power	P_r	10 kW
Primary voltage	V_1	340 V - 440 V
Secondary voltage	V_2'	400 V
Tertiary voltage	V_3'	340 V - 440 V
Switching frequency	f	20 kHz - 100 kHz

turn ratio of the transformer can be designed as 1:1:1. Thus, the primary voltage, $V_{1\%}$, varies from 85% to 110%. The tertiary side's voltage range, $V_{3\%}$, is from 85% to 110%. The voltage of the secondary side is the same as the rated voltage.

TABLE 3.2: Primary-referred Parameters

Symbol	Parameter	Normalization
$1 : n_2 : n_3$	$1 : 1 : 1$	N/A
V_1	340 V - 440 V	85% - 110%
V_2	400 V	100%
V_3	340 V - 440 V	85% - 110%

Figure 3.9 shows the relationship between normalized inductance and highest phase shift operation point within the voltage variation ranges of $V_1 = 85\%$ and $V_3 = 85\%$ by applying (3.27). This indicates that $L_\%$ needs to be smaller than 35.6% for this application.

If the practical implementation and operation have an error in each inductance, the proposed method is still can be used. For example, the datasheet of an inductor shows that the inductance may have an error [107]. In addition, it shows that the error of inductance is depended on the operating current [108]. Therefore, the normalized inductance should be smaller than the limitation value, $L_{\%max}$. As in this application, normalized inductance is suggested equal or smaller than 30%, which allows the error is 18%, at the rated power, and even higher error at lower power. 35.4% is smaller than $L_{\%max}$.
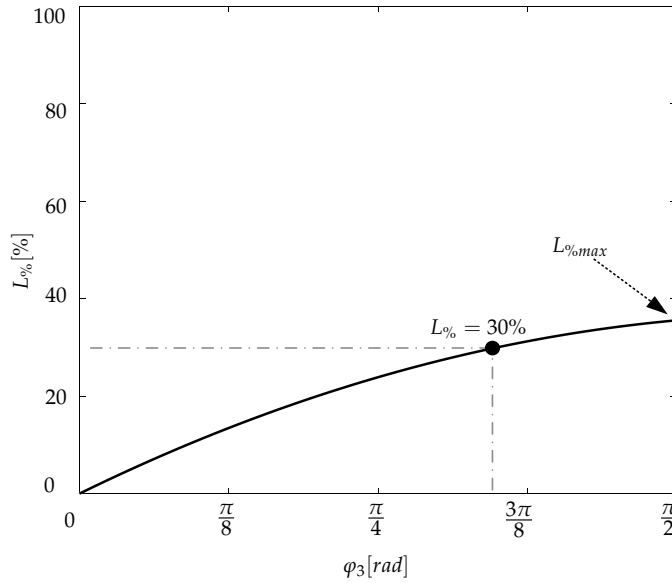
FIGURE 3.9: Relationship between normalized inductance and high-est phase shift operation point when $V_1 = 85\%$ and $V_3 = 85\%$.

It indicates that the power is limited under the rated power when the normalized inductance is over $L_{\%max}$. For example, the power is limited at 90% when $L_\%$ is 40%, as shown in Figure 3.10. When the inductance is 20%, the converter operates at the rated power with a phase shift smaller than $\pi/6$. However, that is the highest phase shift operation when the voltage is lowest. At the highest operating voltage, the phase shift is smaller.

Figure 3.11 shows the phase shift operation areas of the TAB converter for the household application in the comparison of the normalized inductance $L_\%$ at 20%, and 30%, and 40% respectively. The violet color shows the phase shift operation area of the converter, which is limited by the operation of rated power, $P_1 = P_r$, $P_2 = -P_r$, $P_3 = -P_r$, and at $P_1 = 0$, respectively.

The highest voltage is considered because the phase shift operation area is the smallest, which is critical for the control's accuracy. For $L_\%$ is 20%, the operation
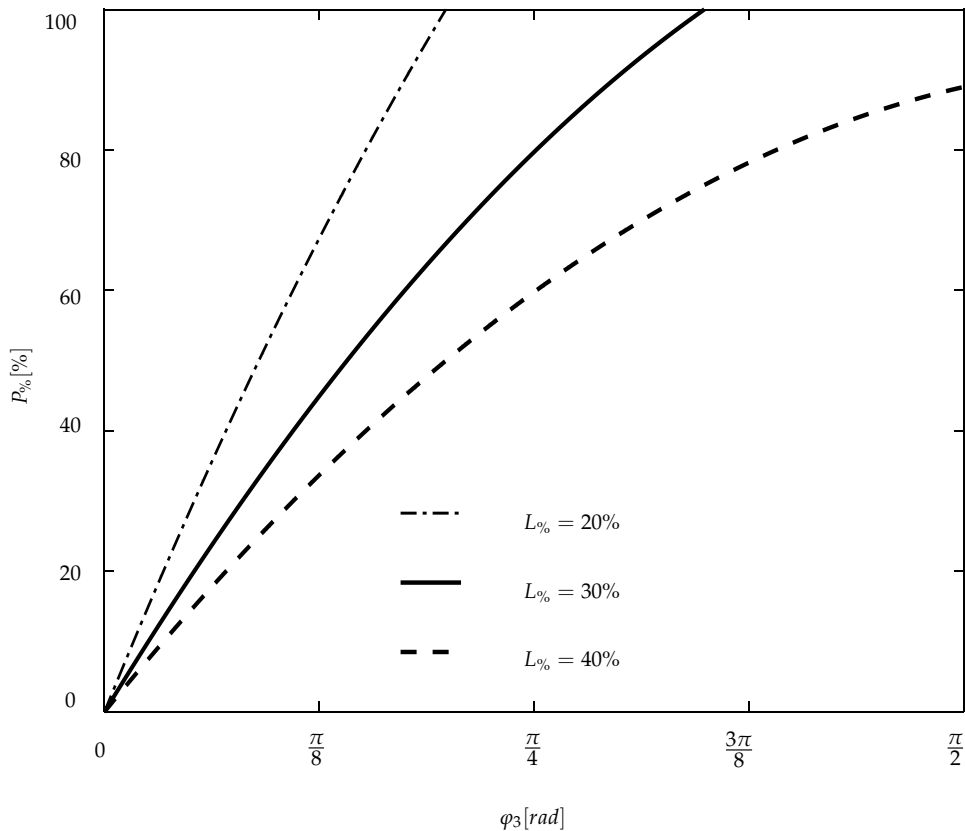
FIGURE 3.10: Power transmission ability at different inductances
when $V_{1\%} = 85\%$ and $V_{3\%} = 85\%$.

area is small, as shown in Figure 3.11(a). Depending on the operation mode, but the

phase shift angle of one port is smaller than 11°, which is sensitive in control. Each

degree affects 10% of the rated power. For $L_\%$ is 30%, the phase shift angles of both

two ports are higher 16° at the rated power, as shown in Figure 3.11(c). When the $L_\%$

is 40%, the converter can operate all the mode at the highest voltage Figure 3.11(e).

However, at the lowest voltages, the phase shift falls in the maximum phase shift

and loses some operation modes, as shown in Figure 3.11(d).

The peak current of port 2 in mode 1-2 is considered for various normalized

inductance values, as shown in Figure 3.12. It shows that for this application and

voltage variation range, the inductance in the range of 20%-34% has a small peak
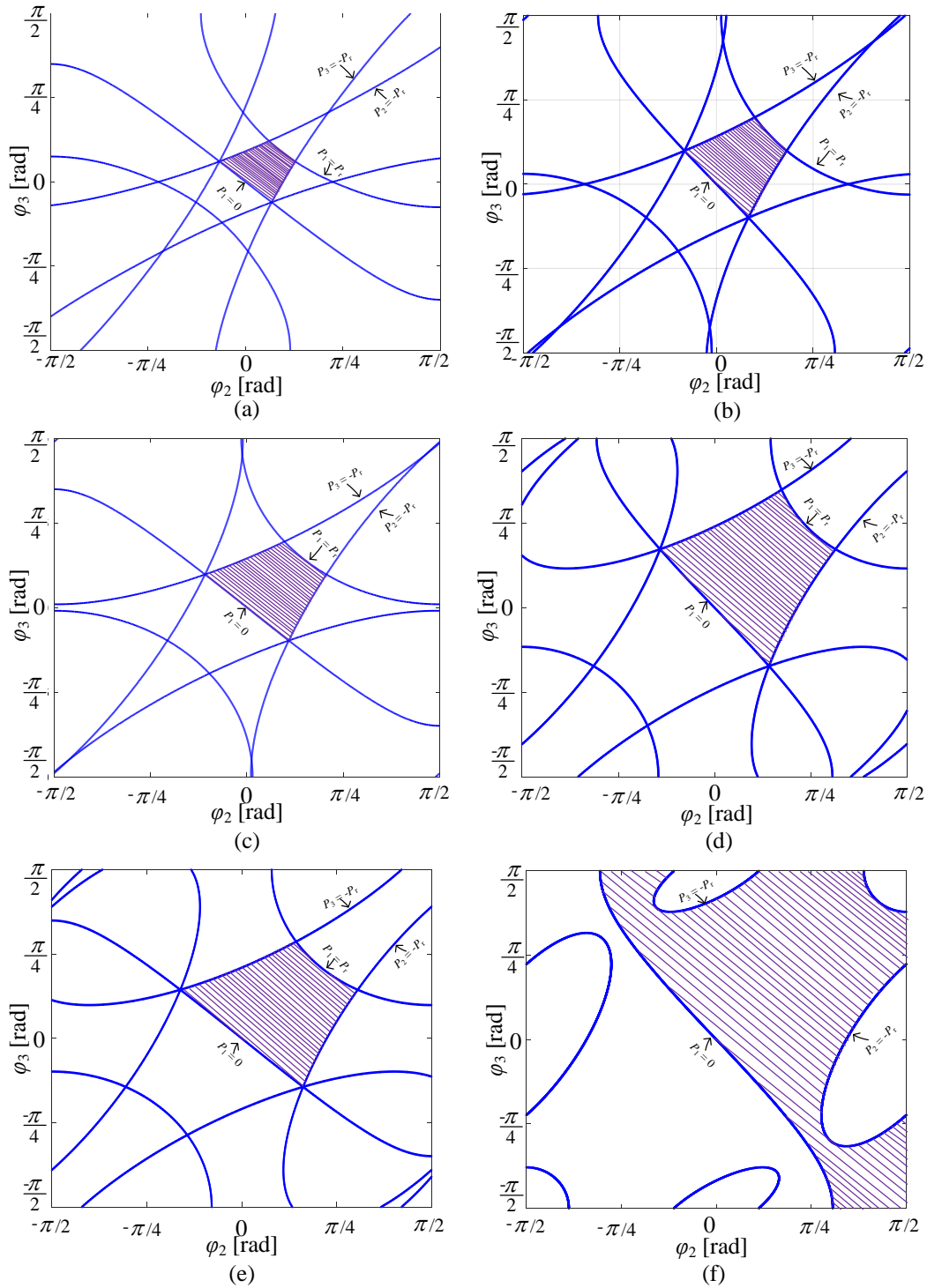
FIGURE 3.11: Phase operating area in variation of the voltages with different inductance. (a) at $V_{1\%} = 110\%$ and $V_{3\%} = 110\%$, $L_\% = 20\%$; (b) at $V_{1\%} = 85\%$ and $V_{3\%} = 85\%$, $L_\% = 20\%$; (c) at $V_{1\%} = 110\%$ and $V_{3\%} = 110\%$, $L_\% = 30\%$; (d) at $V_{1\%} = 85\%$ and $V_{3\%} = 85\%$, $L_\% = 30\%$, (e) at $V_{1\%} = 110\%$ and $V_{3\%} = 110\%$, $L_\% = 40\%$; (f) at $V_{1\%} = 85\%$ and $V_{3\%} = 85\%$, $L_\% = 30\%$,

current.
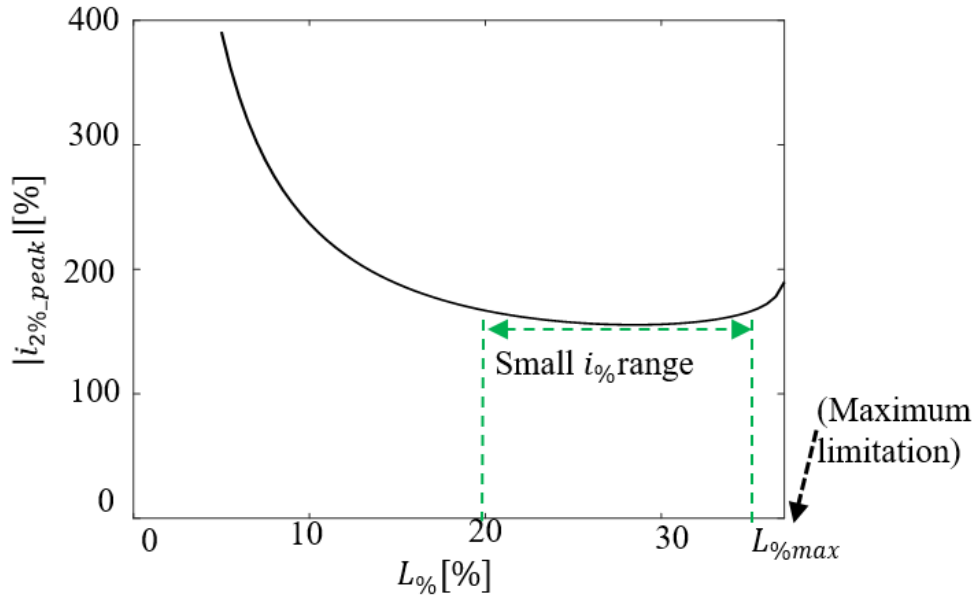
FIGURE 3.12: $i_{2\%peak}$ and $L_\%$ relationship.

It indicates that the normalized inductance $L_\%$ at 30% is a suitable point for this application. There is no issue regarding the operation area of the TAB converter. Figure 3.13 shows the relationship between the transmission power and phase shift at an inductance of 30% for the voltage variation range. It shows that the phase shift operation of the tertiary port, φ_3, varies from 35° to 62.8^o at the rated power.

After determining the normalized inductance, each port's inductance is calculated for two switching frequency systems, as shown in Table 3.3. The switching frequency increases in inverse proportion to the inductance (3.7). As a result, the inductances reduce five-fold when increasing the switching frequency from 20 kHz to 100 kHz.
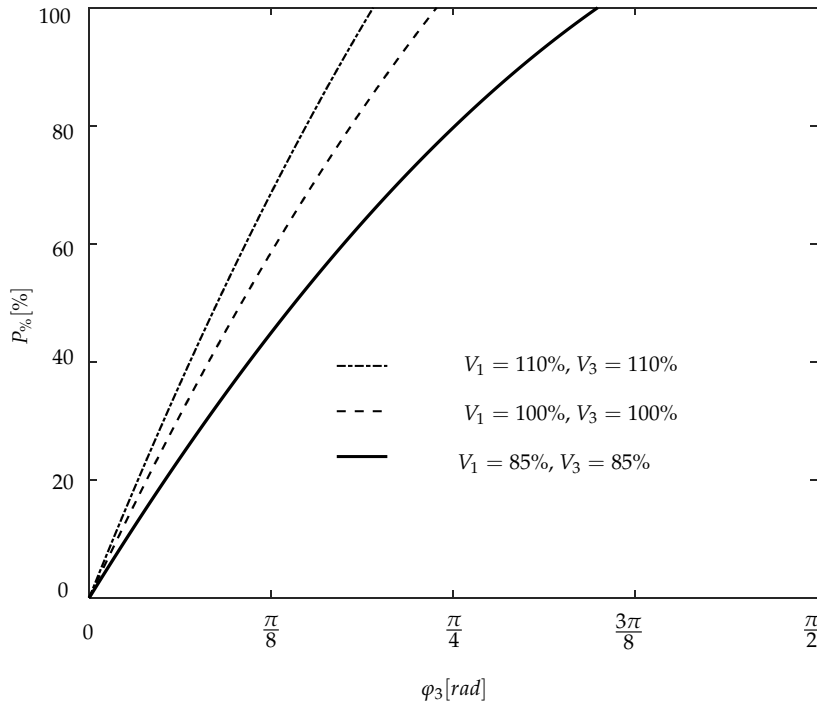
FIGURE 3.13: Transmission power at $L_\% = 30\%$ corresponding to voltage variations of 85% to 110%.

TABLE 3.3: Inductance of TAB converter for Household Renewable Energy System

Symbol	20 kHz system	100 kHz system
$L_\%$	30%	30%
L_{eq}	127.3 μH	25.5 μH
L_1	38.2 μH	7.64 μH
L_2'	38.2 μH	7.64 μH
L_3'	38.2 μH	7.64 μH

3.4 Experimental Setup and Results

3.4.1 Prototype System Rated at 200 V and 500 W

A small-scale system rated at 200 V and 500 W is implemented to verify the proposed

design method, as shown in Figure 3.14. The parameters of the prototype circuit are

shown in Table 3.4. The voltage variations of the prototype circuit are the same as

the 10 kW system shown in Table 3.2. Thus, $V_{1\%}$ and $V_{3\%}$ vary from 170 to 220 V. The

normalized inductance is also designed at 30%. The primary-referred inductance is

38.2 μH for the prototype circuit at the switching frequency of 100 kHz.

Figure 3.15 shows the prototype transformer and external inductors. The external inductors use air cores. The measured inductances are shown in Table 3.5. Each series inductance includes each external inductance and the leakage inductance of the transformer on the same side.
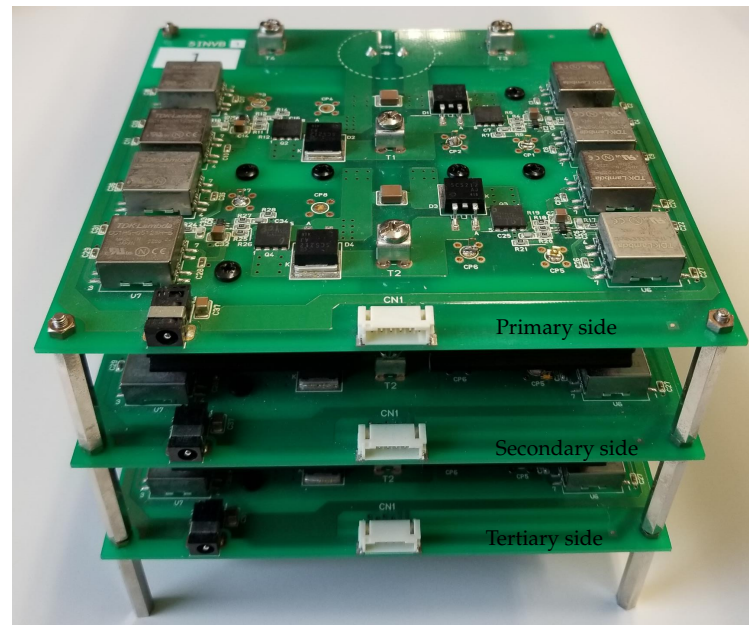
FIGURE 3.14: Implementation of experimental prototype circuit.

TABLE 3.4: Parameters of experimental prototype circuit

Elements	Symbol	Specification
Rated power	P	500 W
Turn ratio	$1 : n_2 : n_3$	1:1:1
Primary voltage	V_1	170 V - 220 V
Secondary voltage	V_2	200 V
Tertiary voltage	V_3	170 V - 220 V
Normalized inductance	$L_\%$	30%
Switching frequency	f	100 kHz
Turn ratio	$1 : n_2 : n_3$	1:1:1
Equivalent inductance	L_{eq}	127.3 μH
Primary-referred inductance	L	38.2 μH
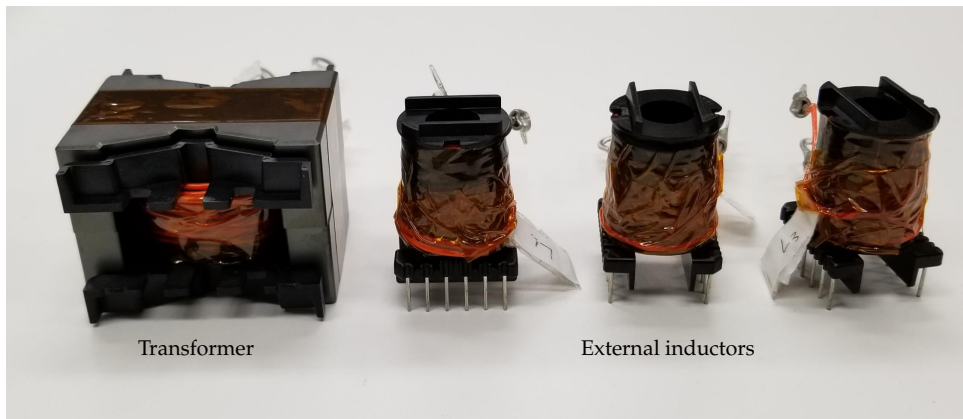
FIGURE 3.15: Implementation of transformer and inductors.

TABLE 3.5: Implementation of inductance in experimental prototype circuit

Elements	Symbol	Specification
Primary series inductance	L_1	38.1 μH
Secondary series inductance	L_2'	38.5 μH
Tertiary series inductance	L_3'	38.2 μH

3.4.2 Experimental Results

The experimental circuit was tested for most critical operations types when the transmission power is between the primary and tertiary ports with no power in the secondary port. The phase shift operation range of the converter are compared between the theoretical calculation and experiment. Three states are applied during the experiments, namely, the lowest voltage, the highest voltage, and the rated voltage design.

Figure 3.16 shows the inductance currents i_1, i_2', and i_3' and voltages between the phase leg midpoint, u_1, u_2', and u_3' for each port when the voltages of the three ports are 100% of the rated power. The phase shift of the tertiary port is 42.7º, which is almost same the same the calculated value as 42.9º.

Figure 3.17 shows the experiment results for $V_1 = 85\%$ and $V_3 = 85\%$. The actual

phase shift of the tertiary port is 62.3º, which is close to the calculated phase shift of

62.8º. Figure 3.18 shows the experiment results in for $V_1 = 110\%$ and $V_3 = 110\%$.

The preliminary phase shift of the tertiary port is 35.4º, which is also close to the

calculated phase shift of 35º.

Figure 3.19 shows a comparison between the experimental results and the the-

oretical calculations for the power of 40% to 100%. The three lines indicate the re-

lationship between power and phase shift of the three voltage conditions by calcu-

lating. The dotted points are the experimental results. It shows that the calculated

and experimental results are almost the same within 1% error in the voltage range

85%-110%.

3.5   Summary

A design procedure triple active bridge converter was proposed. The parameters are

normalized in percentage. Therefore the proposed method can be applied in many

power voltage level and variation. By pplying the design method, the complicated

relationships between the power, phase shifts, switching frequency, voltage varia-

tions, and inductances were clarified. The limitation of inductances corresponding

to the different voltage variations is specified. The effect of the inductance to the

peak current and the operating phase shift angle range are analyzed. The normal-

ized inductance is solved by the trade-off between the phase shift operating area and

peak current.

The proposed method is applied to design a system rated 400 V - 10 kW ef-

fectively. It shows that the normalized inductance is at 30% is one of the suitable

design inductances when the voltage of primary and tertiary port varies from 85%

to 110%. A small-scale system rated at 200 V and 500 W was implemented to verify

the proposed method. The experimental results correspond to the phase shift angle

calculation results within 1% error in the voltage range 85%-110%. Based on this,

the proposed method can be applied to design the TAB converter to be for various

applications.
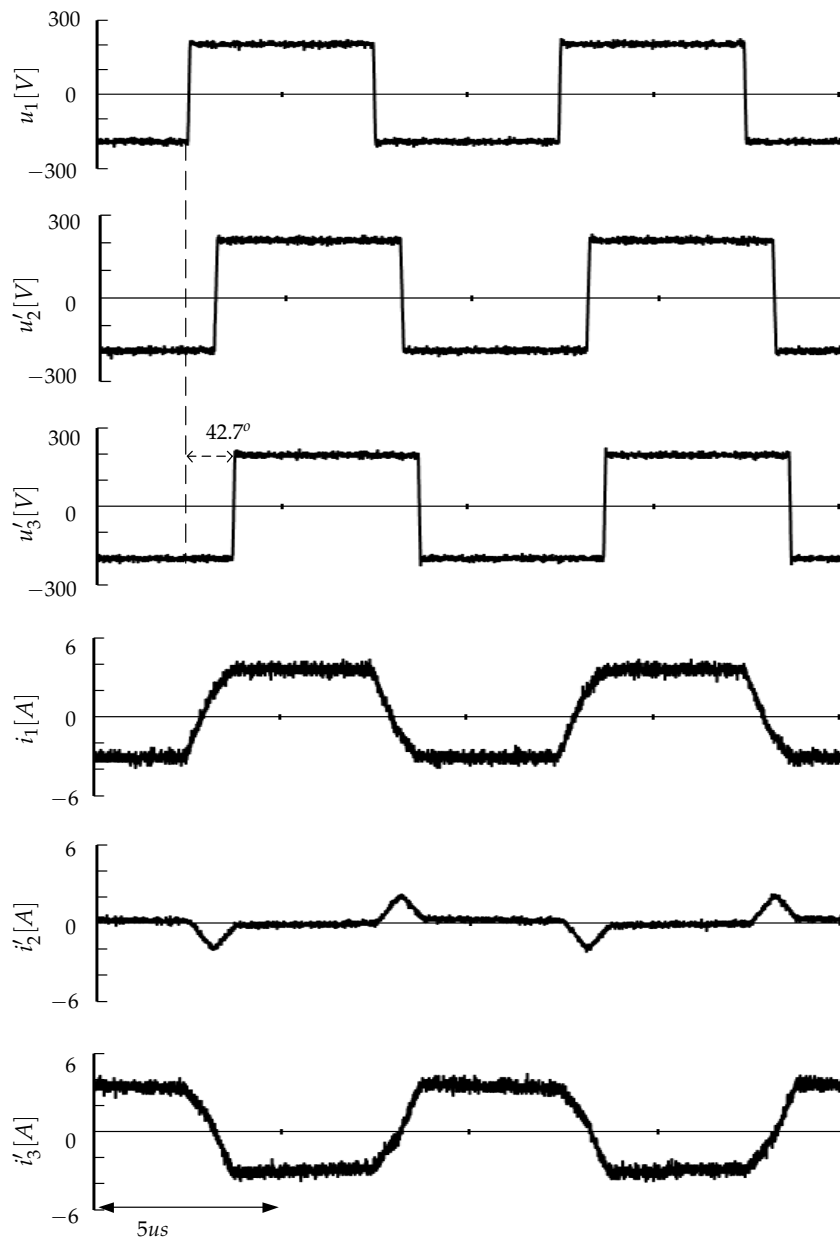
FIGURE 3.16: Experimental result when voltages of three ports are 200V (100%).
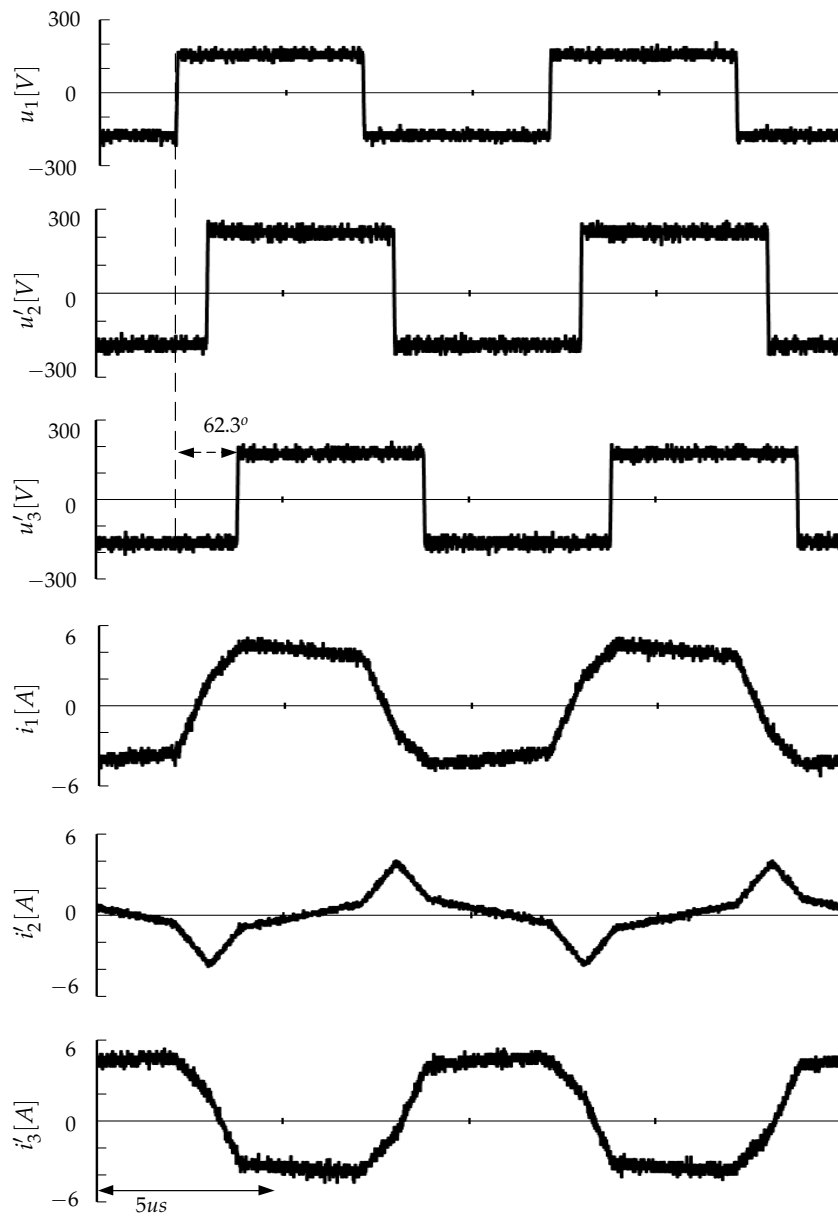
FIGURE 3.17: Experimental result when $V_1 = 170\text{V}$, $V_2 = 200\text{V}$, $V_3 = 170\text{V}$.
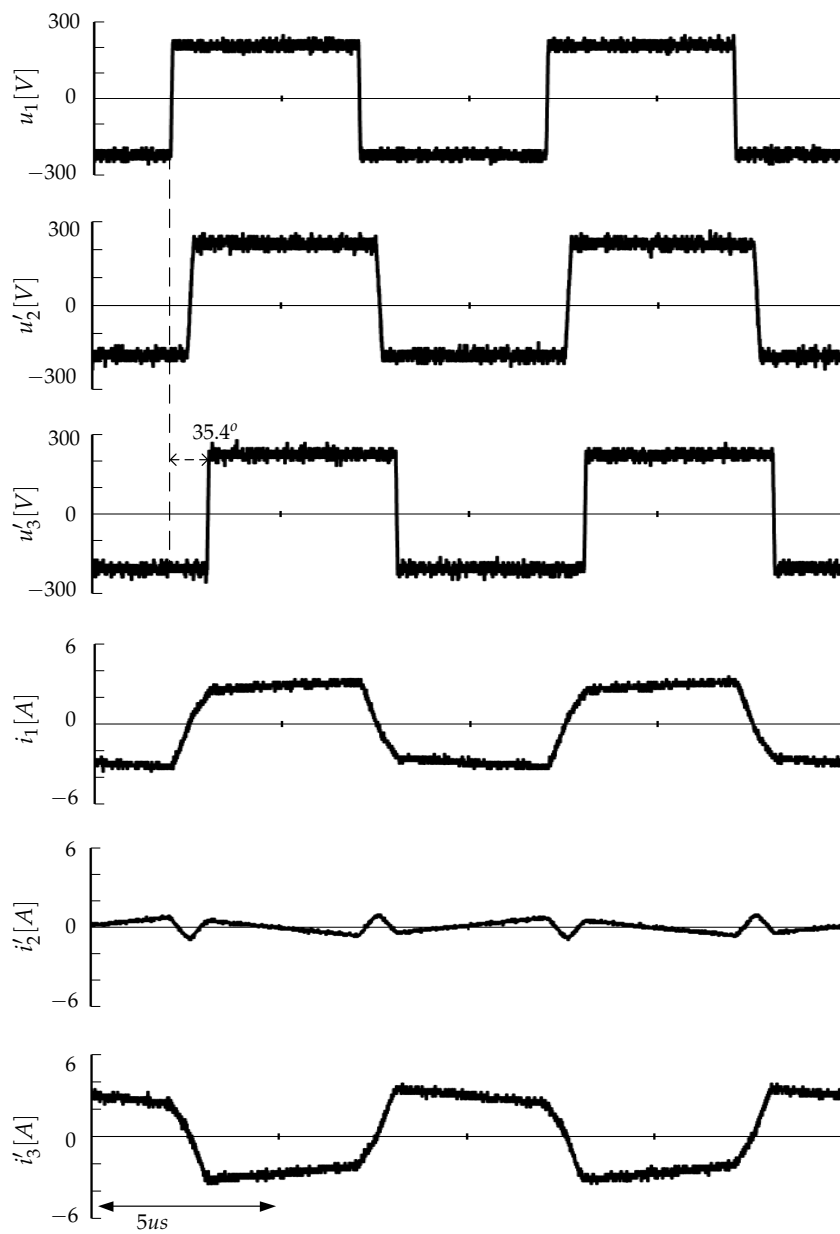
FIGURE 3.18: Experimental result when V_1 = 220V, V_2 = 200V, V_3 = 220V.
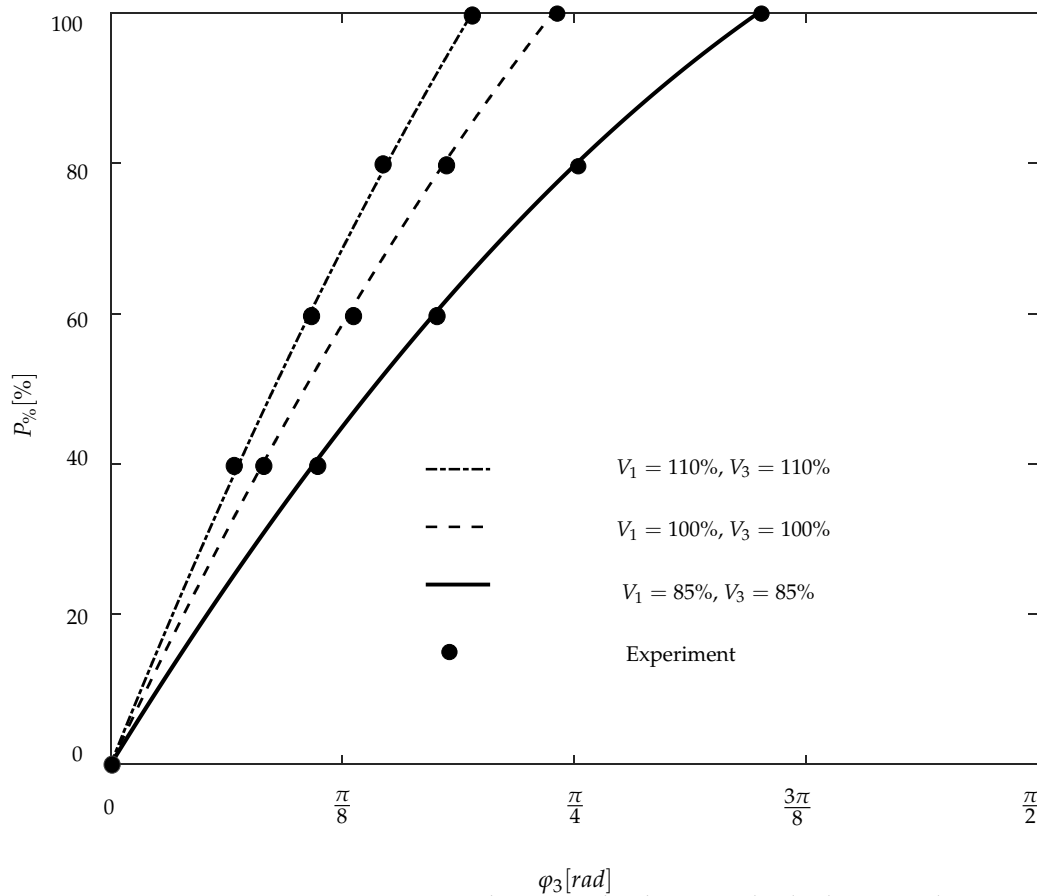
FIGURE 3.19: Comparison between the theoretical calculation and experimental results.

Chapter 4

Battery Voltage Balancing Method

4.1 Proposed Battery Balancing Method and the Operation Principle

4.1.1 Proposed Direct Cell-to-Cell Balancing Circuit

Figure 4.1 shows the proposed balancing method to maximize the capacity of the battery pack [109]-[112]. The battery pack, which is connected to one port of the TAB converter, includes many cells connected in series and parallel. The number of cells in a balancing module can be decided depending on the number of the battery cell in a battery pack and the balancing target. Figure 4.2 shows both power and control diagrams of the proposed active cell-to-cell balancing circuit for a battery module. It composes of four blocks. A digital signal processor (DSP) is used to control both the balancing circuit and also the TAB converter. A monitoring integrated circuit (IC) is used to measure the voltages of the cells. A relay network is used for selecting the cells that need to be balanced. An isolated DC-DC converter is designed to deliver power between the selected cells.

The relay network has two strings of relays. One string of relays, R_{a_1} to R_{a_n}, are used to connect the battery cell to the primary side of the converter via the DC bus, DC_{a_1} and DC_{a_2}, while the other string of relays, R_{a_1} to R_{a_n}, are used to connect

the battery cell to the secondary side of the converter via the DC bus, DC_{b_1} and DC_{b_2}. It is possible to transfer the charge from any cell to any other cell in a battery module.
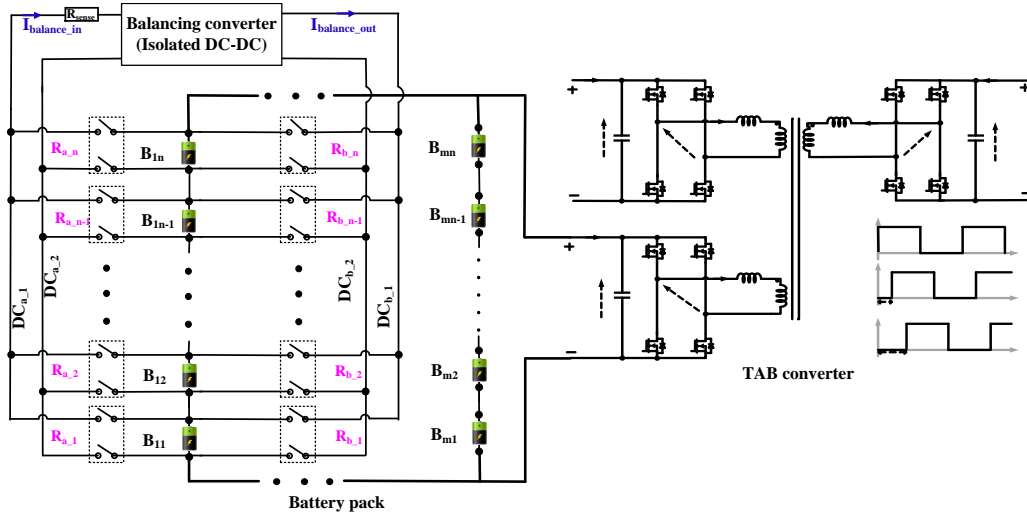
FIGURE 4.1: Proposed cell-to-cell balancing method using isolated DC-DC converter.

The voltage of each cell of the battery pack, from V_{B1} to V_{Bn}, is measured by using the monitoring IC. Then, they are transmitted to the DSP. The balancing current, $I_{balance\_in}$, is calculated by measuring voltage, V_{Bsense}, of a current sense resistor, R_{sense}, on the primary side. The current at the secondary side, $I_{balance\_out}$, can be calculated with the turn ratio and the efficiency of the isolated DC-DC converter.

The first advantage of the proposed method is its ability to transfer the charge directly from the highest voltage cell to the lowest voltage cell. Hence, its balancing speed is fast, and its efficiency is high since the energy transfer directly between required cells in a battery module. There is no sub-transfer cell necessary. Secondly, unlike the other topologies in [79]-[100], which use lots of photo-couplers or pulse transformers to drive the semiconductor bidirectional switch, the proposed topology does not require any expensive gate driver circuits. As only a cheap transistor
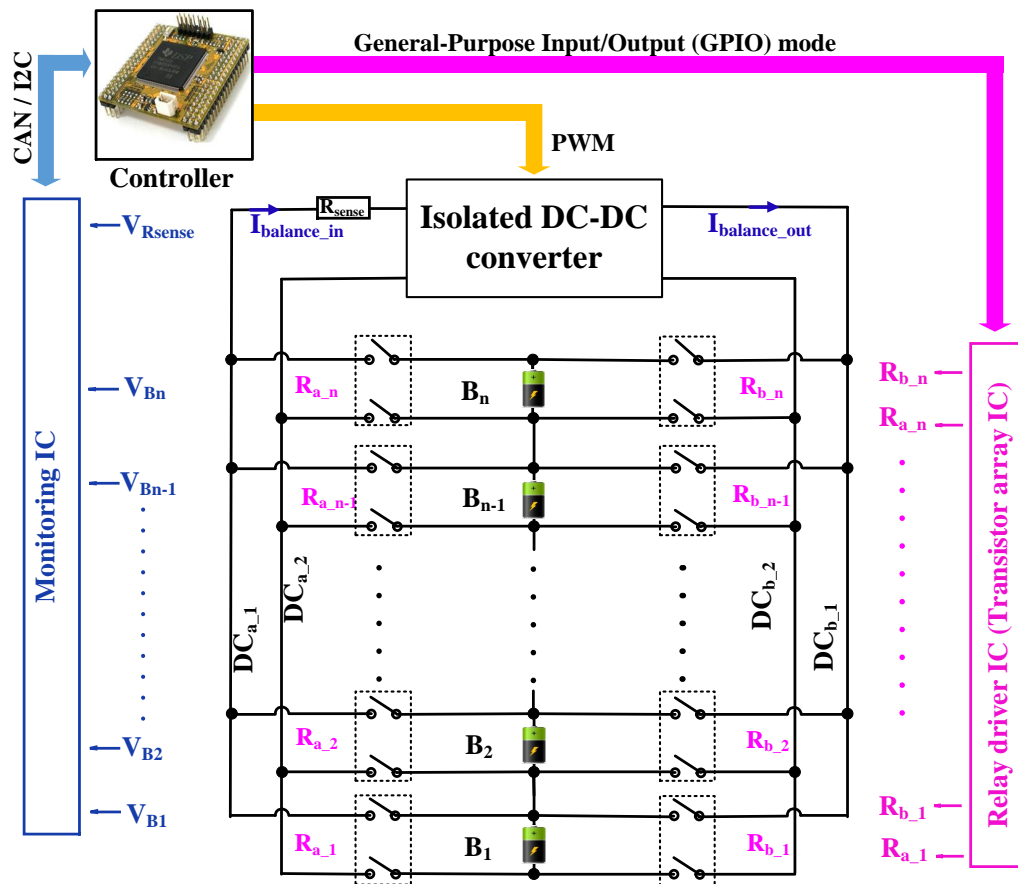
FIGURE 4.2: Balancing circuit for a battery module.

array IC is required to drive the relays on each DC bus, the cost of the system can be significantly reduced. Also, the transistor array IC can share the power supply with the controller, thereby reducing the number of the device and cost. The third advantage is the ease of implementation and extends the balancing circuit, which is a simple structure. It only requires low-voltage devices and one isolated DC-DC converter. Therefore, it can be applied to many HES systems.

4.1.2 Open Circuit Voltage of the Lithium-ion Battery

The internal impedance affects the balancing current and the terminal voltage of the battery. Therefore, it should be considered during the design process of the balancing circuit. Some battery models have been proposed by previous studies, as shown

in [113]-[117]. A simple equivalent circuit model of the Li-ion battery is widely used
to represent the battery impedance, as shown in Figure 4.3. It is composed of the
open-circuit voltage (OCV), and a Direct current internal resistance, R_{DCIR}. The V_{cell}
and I_{cell} are the terminal voltage and the current of the battery, respectively.
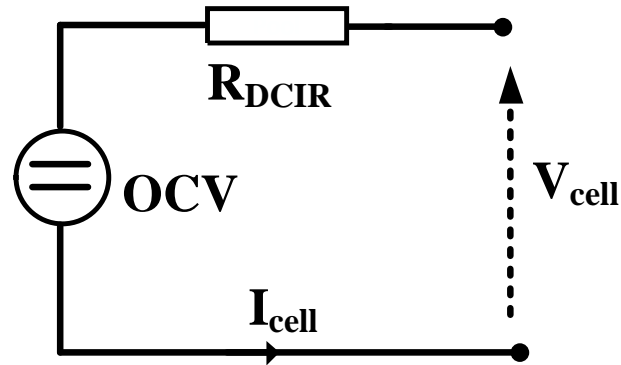
FIGURE 4.3: Simple equivalent circuit model for a Li-ion battery.
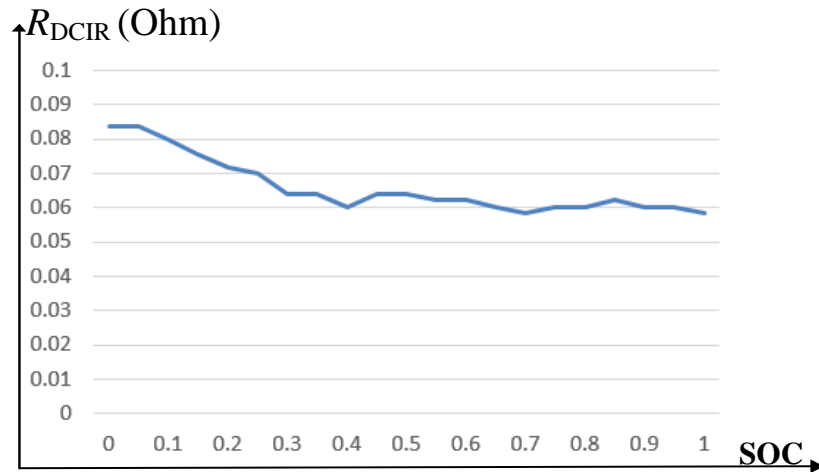
FIGURE 4.4: Impedance of a battery cell.

It has the following.

$$I_{cell} = I_{module} + I_{(balance\_in/balance\_out)} \qquad (4.1)$$

where I_{module} is loading current of all battery module. $I_{(balance\_in/balance\_out)}$ are the balancing current at the input / output of balancing converter, respectively.

As shown in equation (4.1), the current of the battery, I_{cell}, includes two parts. One is the load current of the battery module, I_{module}, and the other is the balancing current, $I_{(balance\_in/balance\_out)}$. The battery module's load current is negative when the battery module is discharging or a positive value when the battery module is charging. The balancing current flows through two cells when the balancing operation is being performed. At the input of the converter, the balancing current, $I_{balance\_in}$, which flows to discharge the high-voltage cell, is measured by the resister, R_{sense}. At the output of the converter, the balancing current, $I_{balance\_out}$, , which flows to charge the low-voltage cell, is calculated by the following equation.

$$I_{balance\_out} = \frac{I_{balance\_in}}{n} \tag{4.2}$$

Figure 4.5 shows the current and voltage of a Li-ion battery cell during the pulse charge test in the rest time. The test is applied to verify the state of charge (SOC)-OCV profile of the battery. A charge pulse equal to 5% of the battery capacity is applied, and the battery rests for three hours to get the OCV. The test is repeated until the battery is fully charged. The voltage transient during the balancing operation is attributed to the internal resistance of the battery.

The non-linear battery parameters have small differences at each voltage point and temperature of the battery. However, the dynamic SOC-OCV estimation for each cell in a battery pack requires cumbersome calculation and takes a long time with high-cost [118]. Therefore, it is acceptable for the balancing circuit to use the
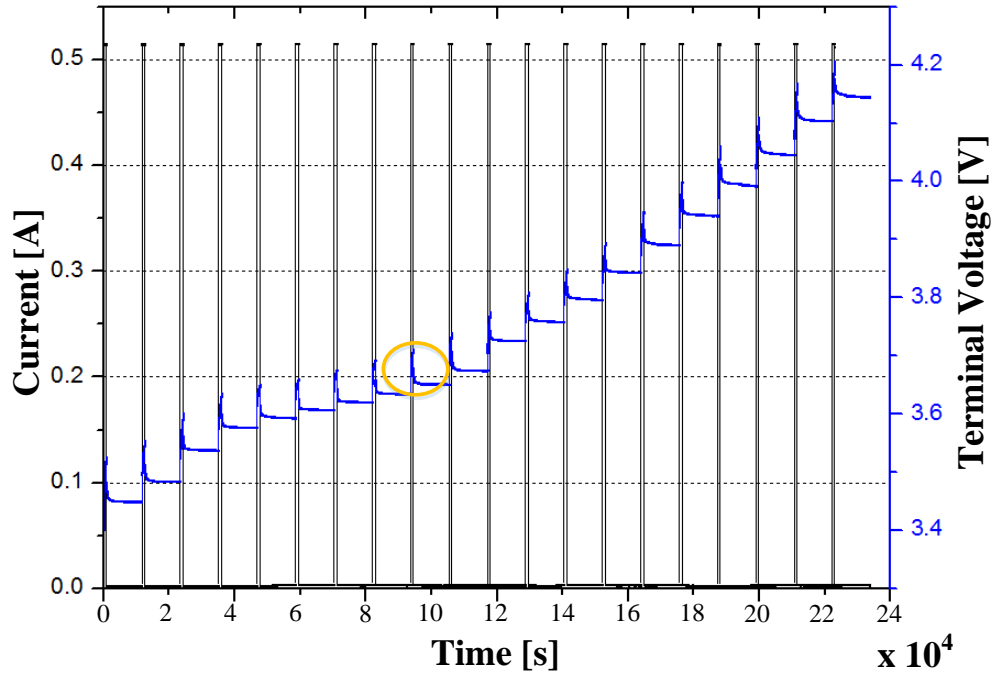
FIGURE 4.5: Current and voltage waveform of the lithium-ion battery during the pulse charge test.

parameter of the battery by a lookup table from the scanning data to reduce the complexity of the balancing circuit. Figure 4.6 shows the transient voltage of the pulse test at the nominal voltage of a Li-ion battery.

The transient voltage, ΔVt, can be approximately calculated from the voltage difference caused by the current pulse and the value of R_{DCIR} can be calculated by the following equation.

$$R_{DCIR} = \Delta V_t / I \tag{4.3}$$

Therefore, the following equations can calculate the transient voltage caused by the balancing currents during the balancing process.

$$\Delta V_{balance\_in} = I_{balance\_in} R_{DCIR} \tag{4.4}$$

$$\Delta V_{balance\_out} = I_{balance\_out} R_{DCIR} \tag{4.5}$$
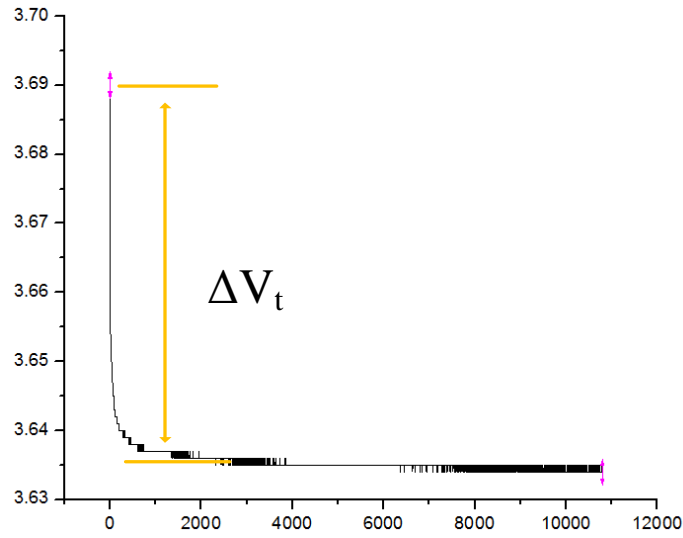
FIGURE 4.6: Transient response of a lithium-ion battery at nominal voltage.

During the balancing process, the transient voltages of two balancing cells are calculated by (4.4),(4.5). Then the OCV of two balancing battery cells is calculated by the following equations.

$$OCV_{max} = V_{cell\_in} - (I_{module} - I_{balance\_in})R_{DCIR} \qquad (4.6)$$

$$OCV_{min} = V_{cell\_out} - (I_{module} + I_{balance\_in})R_{DCIR} \qquad (4.7)$$

The OCV of other cells are calculate by the following equation.

$$OCV_i = V_{cell\_i} - I_{module}R_{DCIR} \qquad (4.8)$$

where i is the cell number.

4.1.3 Balancing Algorithm of the Proposed Balancing Circuit

Figure 4.7 shows the balancing algorithm of the proposed method. At the start, the initial set-up of the system is performed. Firstly, the controller reads the voltages of

all cells. If all of them are in the allowable range of the voltage, the controller calculate the OCV of all the cell and finds the cell with the lowest voltage, OCV_{min}, and the cell with the highest voltage, OCV_{max}. Then, at the input side, the relay, R_{a_max}, is closed to connect the cell with OCV_{max} to the input of the converter. Similarly, the relay, R_{b_min}, is closed to connect the cell with OCV_{min} to the output of the converter. Then the two selected cells begin to be balanced by the isolated DC-DC converter.

During the balancing process, the controller continuously updates all the voltages and the balancing current. If any of the cell voltage is out of range, the controller generates a warning signal and turns off the balancing process to protect the battery pack. Then the average voltage, $OCV_{average}$, of all the cells is calculated again. If OCV_{max} is bigger $OCV_{average}$ and OCV_{min} is smaller than $OCV_{average}$, the balancing operation continues. When one of two selected cells reach the average value of the voltage, both relays, R_{a_max} and R_{b_min}, are turned off. After that, the next two cells that have the highest and lowest voltage are found and balanced. The balancing process continues until all the cell voltages are balanced.

Figure 4.8, Figure 4.9, and Figure 4.10 show the operation of the proposed balancing method in three main steps. In the beginning, the controller scans the status of all cells via monitoring IC as shown in Figure 4.9. After finding the lowest and highest battery cells, Figure 4.9 shows a specific pair of cells is connected to the isolated DC-DC converter for a balancing operation. In this case, cell number $Bn - 1$ represents the cell with the highest voltage, and cell number B_1 represents the cell with the lowest voltage. Therefore, cell B_1 is connected to the output of the converter by
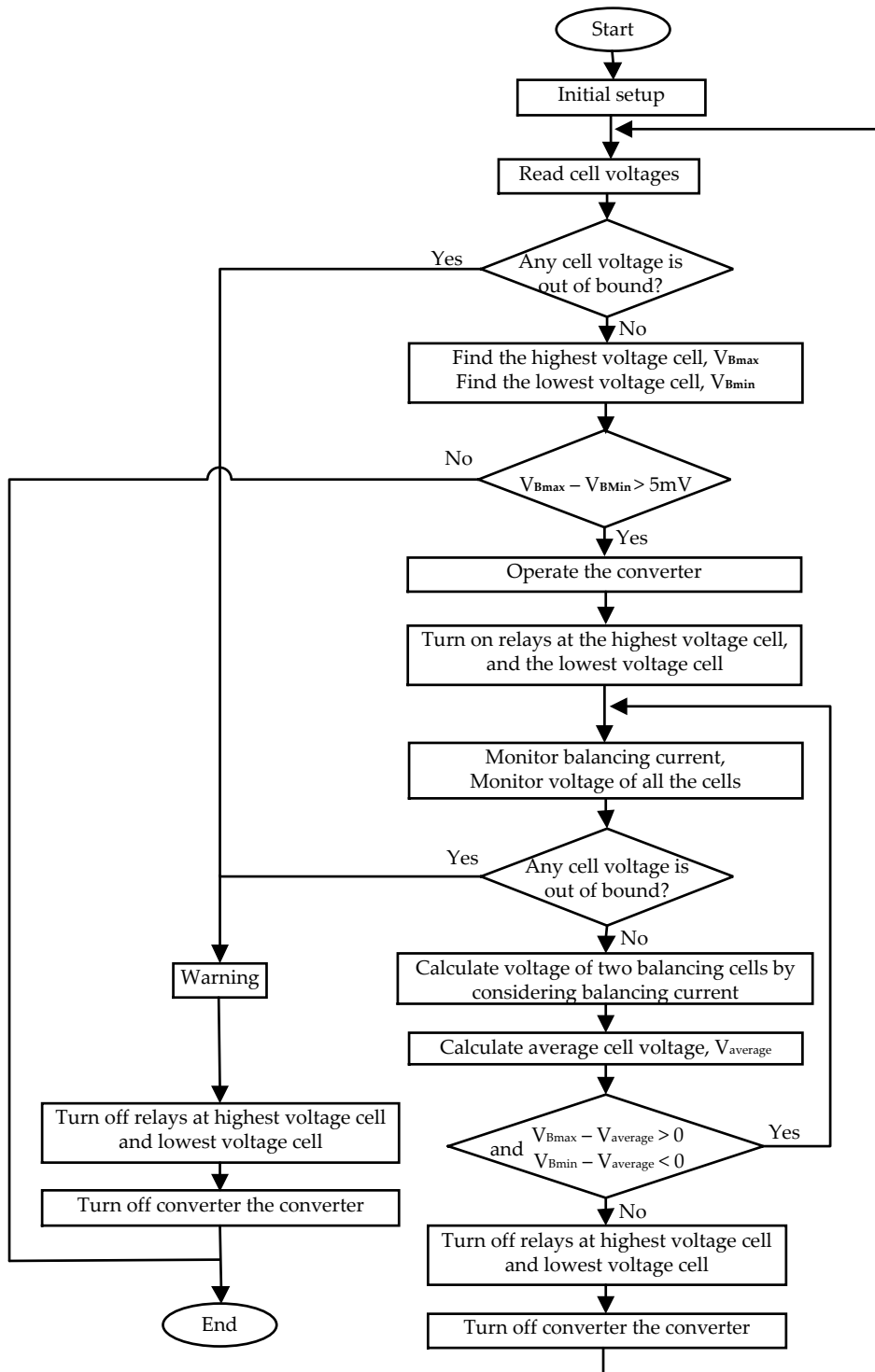
FIGURE 4.7: Balancing algorithm of the proposed circuit.
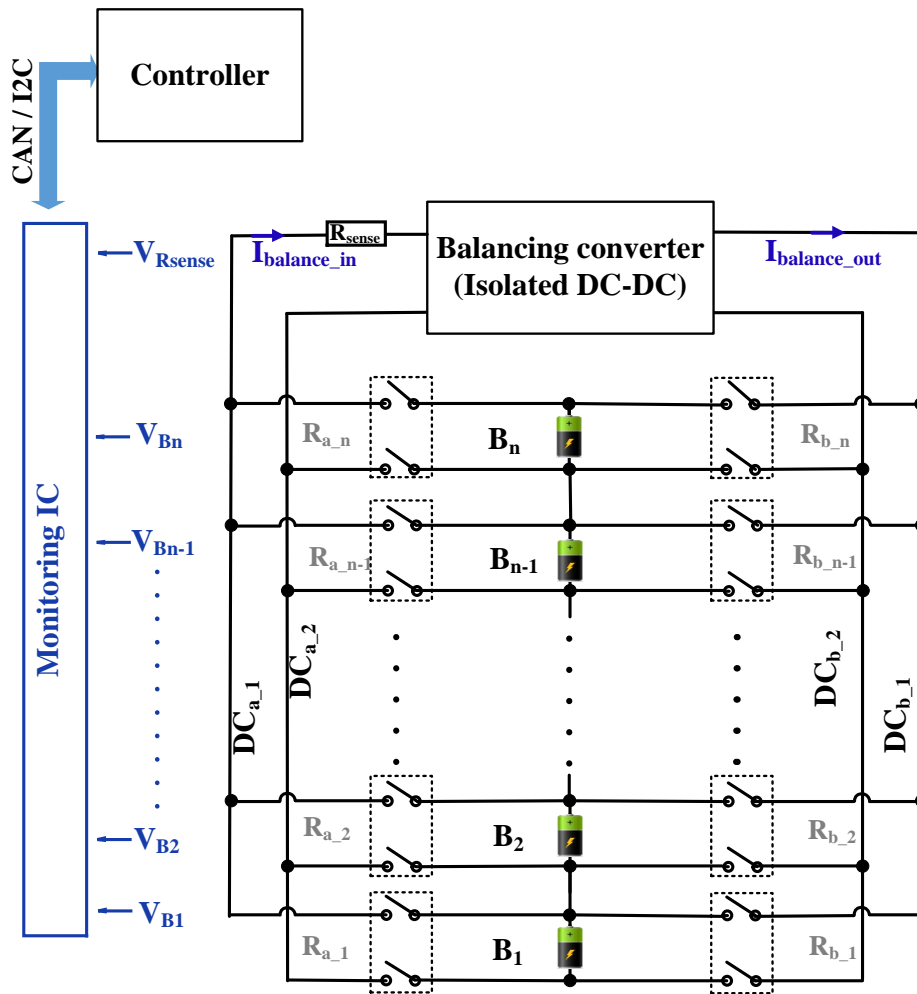
FIGURE 4.8: Step 1: Monitoring battery condition.

turning on relay R_{b_1} and cell B_{n-1} is connected to the input of the converter by turn-

ing on relay R_{a_n-1}, respectively. All other relays remain turned off. Then these two

cells start to become balanced immediately by the operation of the isolated DC-DC

converter. During the balancing process, the controller keeps updating the voltage

of all the cells, as shown in Figure 4.10.
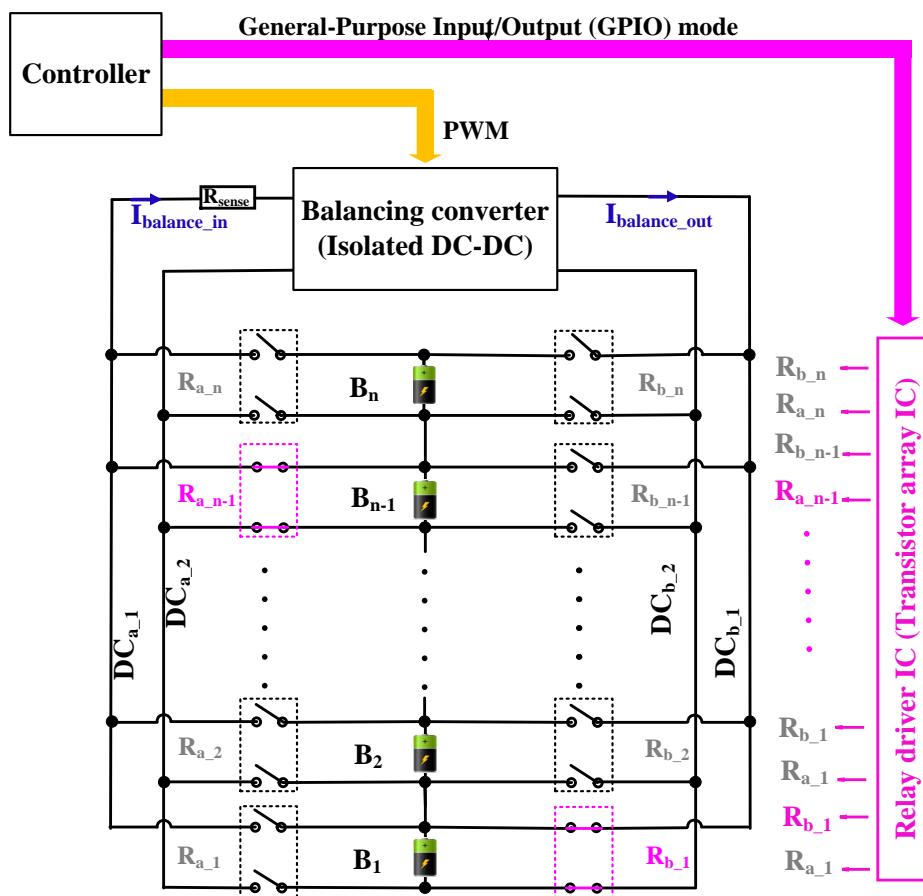
FIGURE 4.9: Step 2: Turn on relay and balancing converter for starting balancing process.

4.2 Design of High-Efficiency LLC Converter for the Balancing Circuit

Since an LLC resonant converter has several advantages such as high efficiency, low electromagnetic interference (EMI), and high-power density, it is popularly applied to many applications. Therefore, the LLC converter is adopted for the proposed balancing circuit after a careful investigation of the requirements for the active direct cell-to-cell balancing circuit. Unlike typical converter applications, a cell balancing circuit does not require a constant current operation. Therefore, it is possible to avoid a wide range of switching frequency variations. Thus, the LLC converter can be
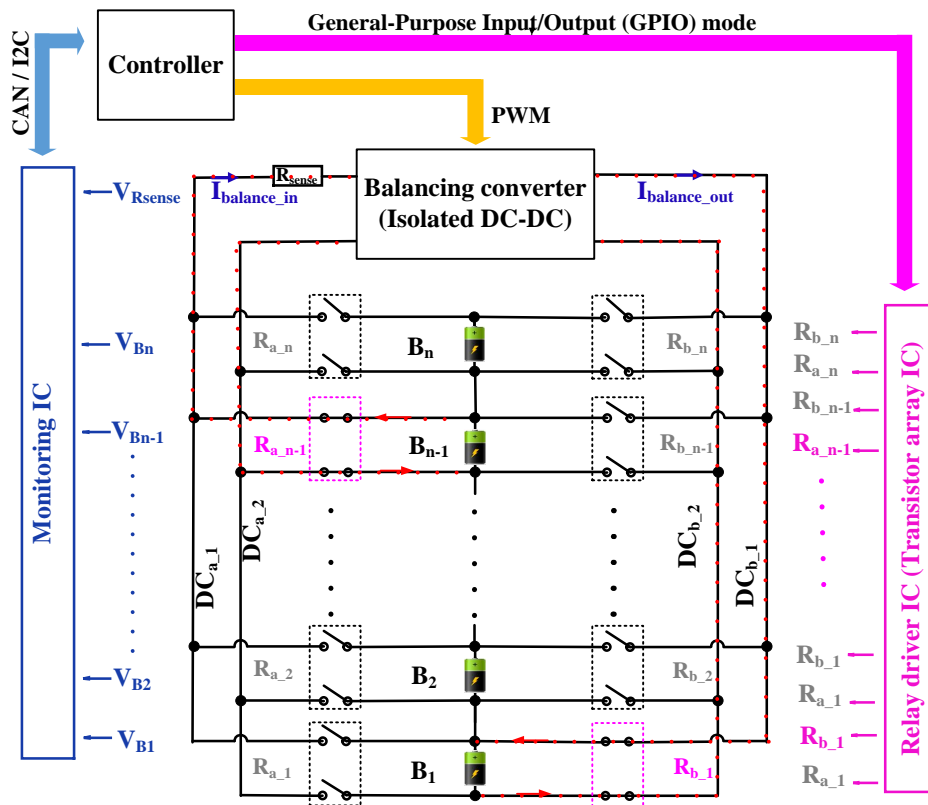
FIGURE 4.10: Step 3: During balancing process.

designed to operate under nominal operation at a constant frequency with a unity

gain without losing the soft-switching condition. Moreover, open-loop control is

preferred since it does not require additional circuitry for the feedback and simplifies

the system.
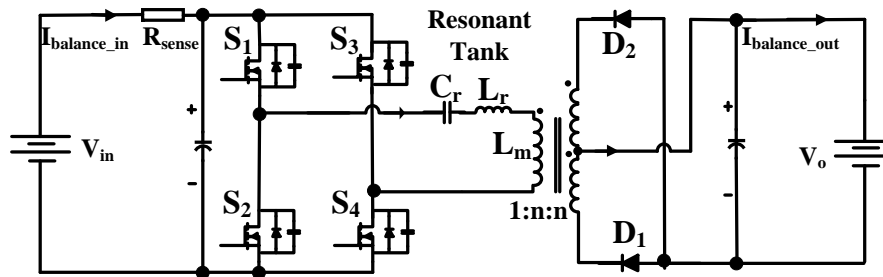
FIGURE 4.11: LLC resonant converter for the balancing circuit.

Although the half-bridge LLC converter is advantageous in terms of component

count, a full bridge LLC converter has been selected due to its lower input ripple and lower conduction loss, as shown in Figure 4.11. In the converter's secondary side, only two diodes are used to constitute a full-wave rectifier for high efficiency. Since the leakage inductance of the transformer, Lr, can be used as the resonant inductor, no additional inductor is required. Figure 4.12 shows a simplified circuit model of an LLC converter using the First Harmonic Approximation (FHA) method. R_{oe} and V_{oe} are the AC equivalent load resistance and voltage of the LLC converter's output, as the following equation.

$$R_{oe} = \frac{8}{\pi^2 \times n^2} \times \frac{V_o}{I_{balance\_out}} \tag{4.9}$$
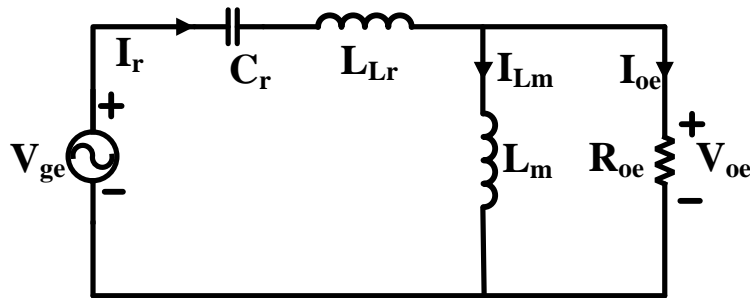
FIGURE 4.12: Equivalent circuit of an LLC converter.

The voltage gain M of the LLC resonant converter can be calculated as the following.

$$M = \left| \frac{m \times f_n^2}{[(m+1) \times f_n^2 - 1] + j\left[(f_n^2 - 1) \times f_n \times Q \times m\right]} \right| \tag{4.10}$$

where f_n is the normalized frequency, m is the inductance ratio between the resonant inductance L_r and the magnetizing inductance L_m, and Q is the quality factor. The

normalized frequency is calculated as the following.

$$f_n = \frac{f_{sw}}{f_r}$$

(4.11)

where f_{sw} is the switching frequency, and f_r is the series resonant frequency as the following.

$$f_r = \frac{1}{2\pi\sqrt{L_r \times C_r}}$$

(4.12)

where C_r is the resonant capacitor. The inductance ratio m is calculated as the following.

$$m = \frac{L_m}{L_r}$$

(4.13)

The quality factor Q can be expressed by the following.

$$Q = \frac{1}{2\pi f_{sw} R_{oe} C_r}$$

(4.14)

Normally, it is essential to choose the inductance ratio m to satisfy the system's requirements with a trade-off between the switching frequency range and the losses of the converter. Since Q and m both have impacts on the converter operation and are related to each other, the design process starts with suitable initial values optimized by iterations, making the LLC converter complex the design process.

However, since the proposed converter only works at the series resonant frequency with a unity voltage gain that is independent of the load, the value of m can be chosen by only considering the ZVS turn-on conditions for all of the primary switches under a light load.

The ZVS turn-on condition for the primary switches is important in designing a converter to achieve high efficiency. During dead-time, the magnetizing current I_m circulates through the parasitic capacitance C_{oss} of the switches before the body diode of the switches conducts. Hence, the ZVS condition can be guaranteed if (4.15) and (4.16) are satisfied. The magnetizing current is calculated by using (4.17).

$$\frac{1}{2}(L_m + L_r) \times I_m^2 > \frac{1}{2}(2C_{oss})V_{in}^2 \tag{4.15}$$

$$t_{dead} \geq 16C_{ds} \times f_{sw} \times L_m \tag{4.16}$$

$$I_m = \frac{2\sqrt{2}}{\pi} \times \frac{1}{n} \times \frac{V_o}{2\pi \times f_{sw} \times L_m} \tag{4.17}$$

The resonant capacitance value can be calculated by using the following equation.

$$C_r = \frac{1}{(2\pi f_{sw})^2 L_r} \tag{4.18}$$

The converter operates at the series resonant frequency with a unity gain. The output current of the converter (the charge current of the battery) is decided by the voltage difference between the converter output voltage V_0 and the battery voltage V_B, and the internal DC resistance of the battery R_{DCIR}. Therefore, in theory, the turns ratio of the transformer can be 1. However, the turns-ratio transformer has to be larger than 1 in practice to compensate for the voltage drop at each of the converter components, as shown in the following.

$$V_o = (V_{in} - 2 \times I_{balance\_in} \times R_{ds\_on})n - V_f - V_{ad} \tag{4.19}$$

$$n = \frac{V_o + V_f + V_{ad}}{(V_{in} - 2 \times I_{balance\_in} \times R_{ds\_on})} \tag{4.20}$$

Where V_0 is the output voltage of the converter, V_{in} is the input voltage of the converter, $I_{balance\_in}$ is the input current of the converter, R_{ds_on} is the junction resistance of the switch, V_f is the forward voltage of the diode, and V_{ad} is the additional voltage drop caused by the wire, current sensing resistor, etc. Also, $I_{balance\_in}$ is the balancing current, which is less than the 0.5 C. Here, C is the rated capacity of the battery cell. Figure 4.13 shows a comparison of the simulation waveform of a typical LLC converter and a designed LLC converter. It shows that both converters can achieve ZVS turn-on. However, the designed LLC converter achieves nearly Zero-Current Switching (ZCS) turn-off of the switches due to the design point. Since the converter operates at the resonant frequency, all switches of the designed LLC converter achieve ZVS turn-on and nearly ZCS turn-off in the balancing range.
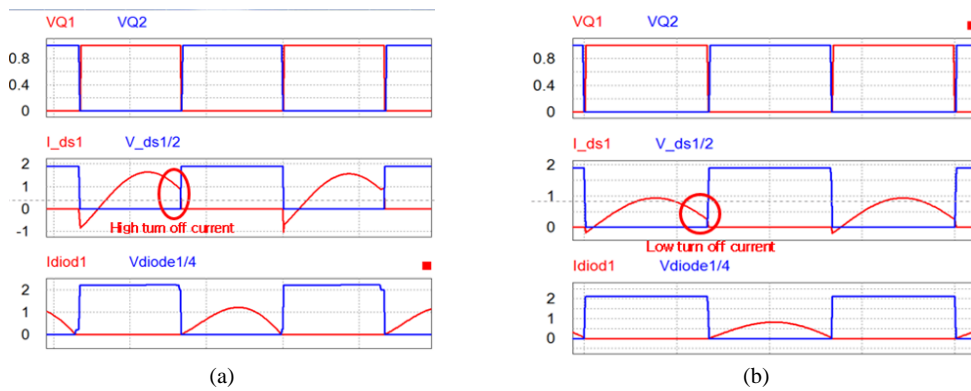
FIGURE 4.13: Simulation waveform of LLC converter. (a) normal LLC converter, (b) designed LLC converter for the balancing circuit.

4.3 Prototype Balancing Circuit and Experimental Result

4.3.1 Prototype Balancing Circuit

A prototype circuit was tested with twelve Li-ion battery cells (LG ICR18650B4, 2.6 Ah) connected in series to demonstrate the validity of the balancing system. The AC equivalent load resistance, R_{oe}, and quality factor, Q, are calculated as shown in Table 4.1. For other battery types with higher capacity and voltage, the designed method can be applied easily by changing the V_o and I_o values.

TABLE 4.1: R_{oe}, and Q of the equivalent of the LLC converter basd on the paprameter of the battery cell.

	Z_1	Z_2	Z_3
V_o	3V	4.2V	4.2V
I_o	1.3A [0.5C]	1.3A [0.5C]	0.13A [0.05C]
R_{oe}	1.30	1.82	18.19
Q	0.337	0.241	0.0241

Figure 4.14 shows an experimental setup to verify the balancing circuit using twelve lithium-ion battery cells. The Oscilloscope measure the control signals and waveforms. The power analyzer measures the efficiency of the LLC converter. Electric power supply and load are used to charge and discharge the battery pack. The balancing circuit is composed of four parts: a switch network with two relays for each cell, an LLC resonant converter for the balancing operation, a DSP TMS320F28335 to control the whole system, and a monitoring IC named bq76940 to measure the voltage of each cell. The monitoring IC can measure the voltage of the telve cells and one current. The parameters and component list of the balancing circuit are shown in Table 4.2.
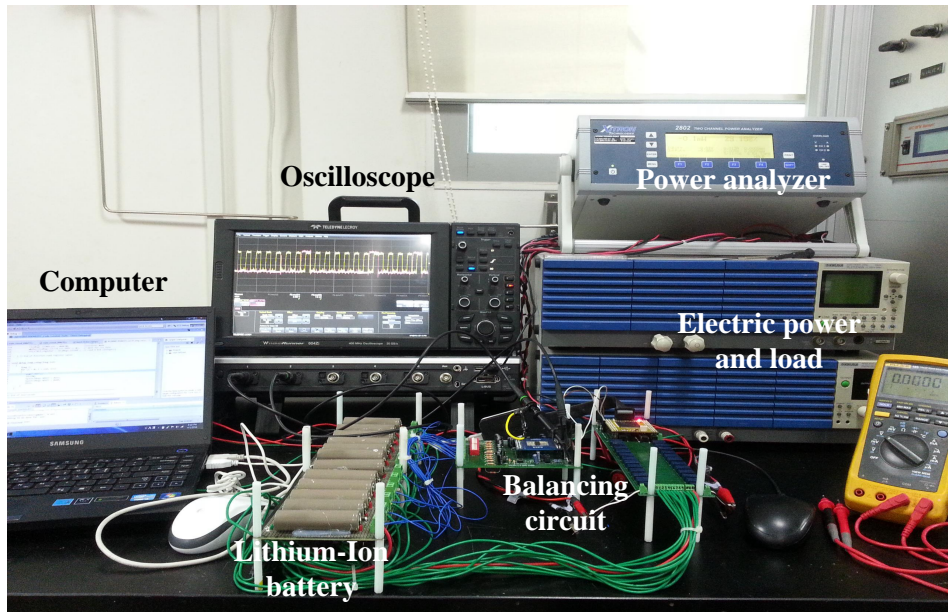
FIGURE 4.14: Experimental setup of the prototype balancing circuit.

4.3.2 Experimental Results

Figure 4.15 shows a waveform of the LLC converter during the balancing operation when the high voltage cell is 4.1 V, and the low voltage cell is 3.9 V. The primary side switches archive ZVS turn-on and nearly ZCS turn-off under both heavy and light loads. The turn-off currents of the primary switches are only 0.1 A, contributing to the reduction of the switching losses. Two diodes on the secondary side achieve full ZVS and ZCS.

A power analyzer (Xitron 2802) measures the converter's efficiency during the balancing process, as shown in Figure 4.17. The efficiency is higher than 92% in the balancing range. The maximum efficiency of the LLC converter is 94.5% at 1.5 W, which demonstrates that the proposed balancing circuit exhibits high-efficiency characteristics.

Figure 4.18 shows the balancing process in the steady-state mode of the prototype circuit for twelve Li-Ion batteries in a module. In the beginning, the voltages

TABLE 4.2: Parameters of the Prototype Balancing Circuit

Components		Parameter	
		Experimental	Theoretical design
LLC converter	Transformer core	Pot core 2213	
	Turn ratio 1: n: n	1:1.2:1.2	1:1.2:1.2
	Magnetic inductance	122 μH	120 μH
	Resonant capacitor	9.9 μH	10 μH
	Leakage inductance	1.9 μH	2 μH
	Resonant frequency	36.7 kHz	35.6 kHz
	MOSFET	IRFZ44NS	
	Schottky diode	PMEG3050EP	
Relay network	Relay driver IC (Transistor array IC)	ULN2803A	
Monitoring	Monitoring IC	Bq76940	
	Resistor current sense	WSR21L000FEA	

of the battery cells show some deviation ranging from 3.55 V to 3.73 V. The voltage variations in twelve cells are measured, and their values at each cell-changing point are saved to DSP memory during the balancing process. Therefore, Figure 4.18 mainly shows the voltage-changing of all the cells.

After reading all of the cell voltages, the system calculates the average value of the cell voltages (3.62 V) and finds that cell number 3 is the highest voltage cell (3.73 V) and cell number 12 is the lowest voltage cell (3.55 V). These two cells are balanced first. After 16 minutes, cell number 12 reaches the average voltage (3.62 V), and the cell balancing system is stopped. After rereading all of the cell voltages, the controller finds that cell number 10 is the highest voltage cell (3.68 V) and that cell number 5 is the lowest voltage cell (3.57 V). These two cells are selected and balanced. This procedure repeats until all of the cells in a battery string have the average voltage. By applying the calculation of transient voltage from balancing current, the cell voltage can be approximately balanced at the average voltage.
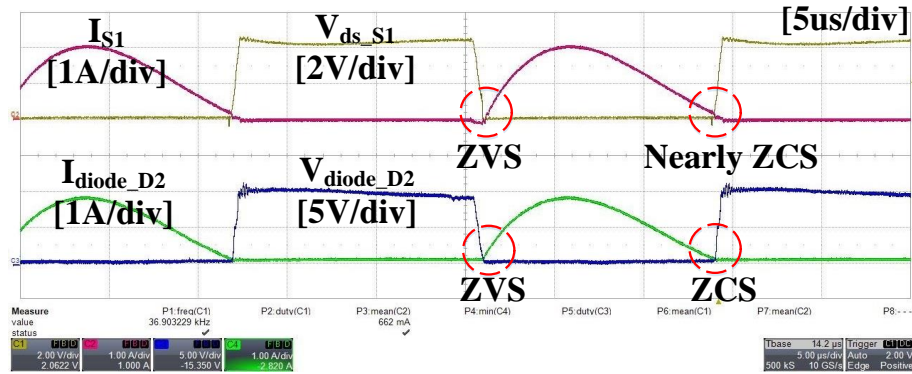
(a)
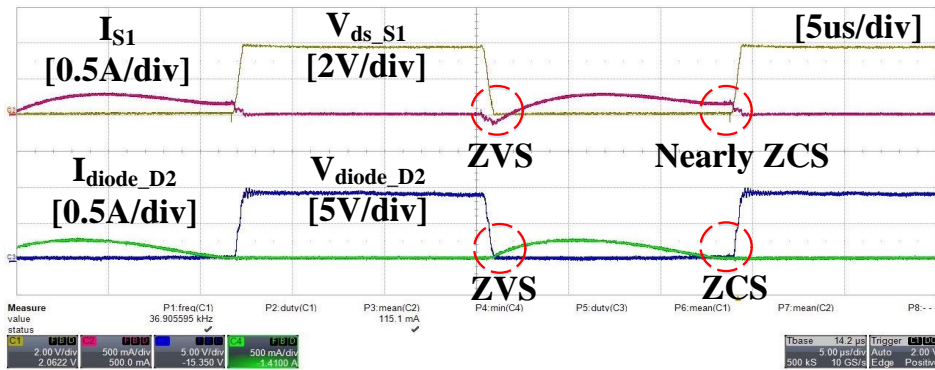
(b)

FIGURE 4.15: Experimental waveform of an LLC converter: (a) normal load 55% (Po=3W); (b) very light load 10% (Po=0.5 W).

A balancing test is also performed during the charging of the battery, as shown in Figure 4.19. In the initial state, all of the cells have some voltage differences. Cell number 4 shows the highest voltage (3.71 V), and cell number 8 shows the lowest voltage (3.51 V). By applying the proposed fast balancing algorithm, all of the cells are balanced at 4.15 V. After that, all the cell can be fully charged.

Figure 4.19 shows experimental results of balancing circuit during the discharging with 1.3 A. At the initial sate, each cell in the battery module shows differences in terms of their voltage. While discharging the battery, the proposed cell balancing algorithm is applied. All of the cells are balanced and reach the cut-off voltage.

To verify the battery pack's capacity improvement, the charging and discharging
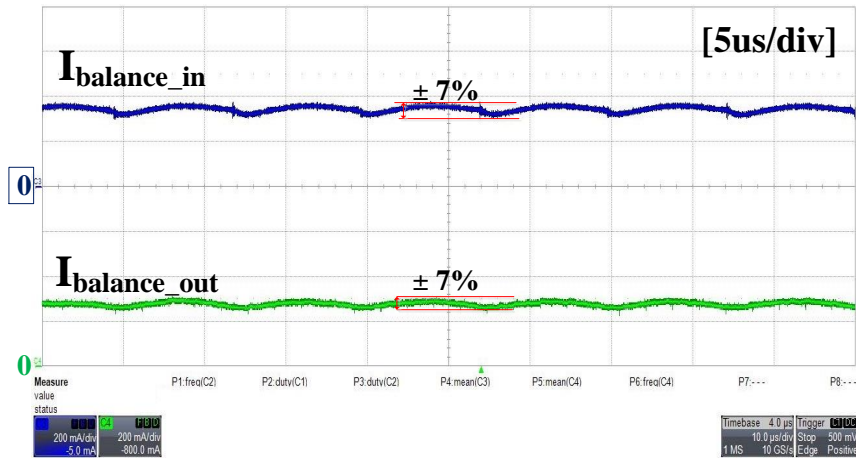
FIGURE 4.16: Balancing current of the proposed method.
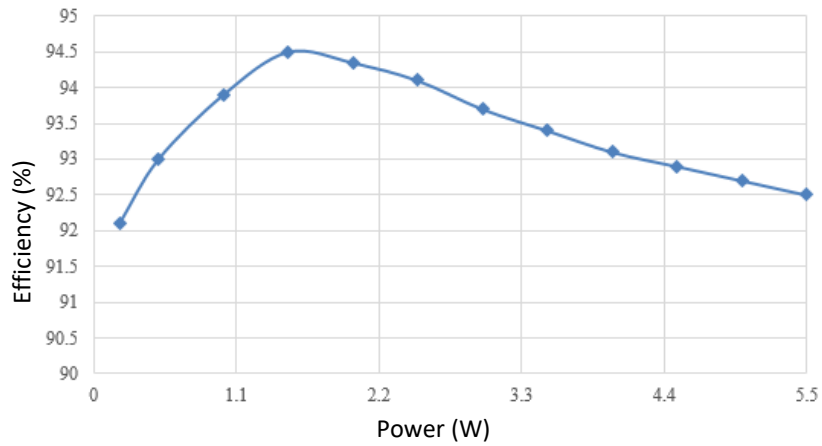
FIGURE 4.17: Efficiency profile of LLC converter for the balancing circuit.

powers to each battery cell batteries are analyzed in detail. The charge in one cell is shown in the following equation.

$$Q_i = C_i \times V_i \qquad (4.21)$$

where, Q_i is the charge in one cell. C_i is the capacity of the cell number i. V_i is the voltage of the cell number i. Then the charge to x cells in the battery module is
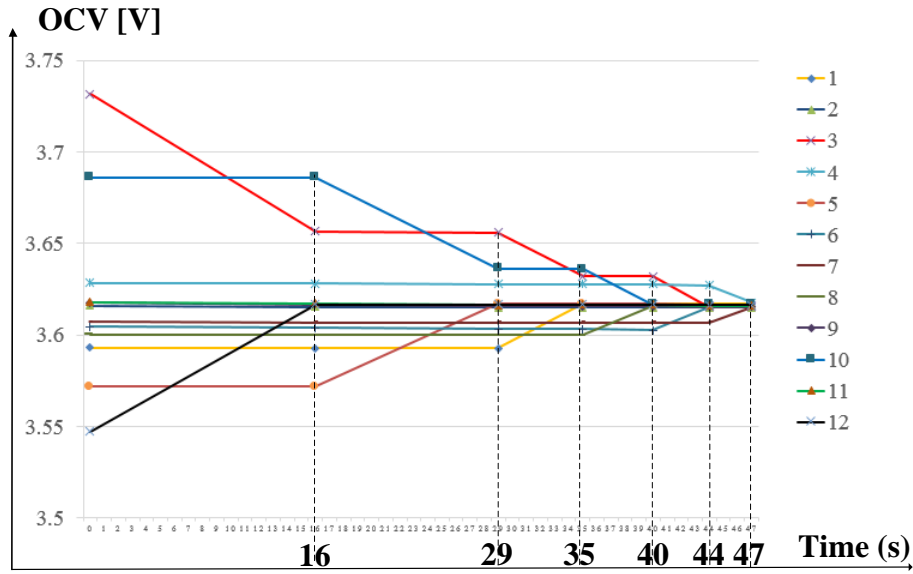
FIGURE 4.18: balancing process in the steady state mode.

calculated by the following.

$$Q_M = \sum_{i=1}^{x} Q_i \tag{4.22}$$

where, Q_M is the charge in the battery module.

In the battery pack, it is assumed that all of the cells have the same initial capacity.

$$C = C_1 = C_2 = \ldots = C_x \tag{4.23}$$

From (4.21) to (4.24), the following can be obtained.

$$Q_M = \sum_{i=1}^{x} Q_i = \sum_{i=1}^{x} C_i V_i = C \sum_{i=1}^{x} V_i \tag{4.24}$$

When charging the battery pack with the proposed balancing circuit, it is possible to charge all of the cells to their full capacities. However, without the balancing circuit, it is impossible to charge the battery module since the charge operation stops when a cell reaches its maximum voltage for the Li-Ion battery's safety reason. By
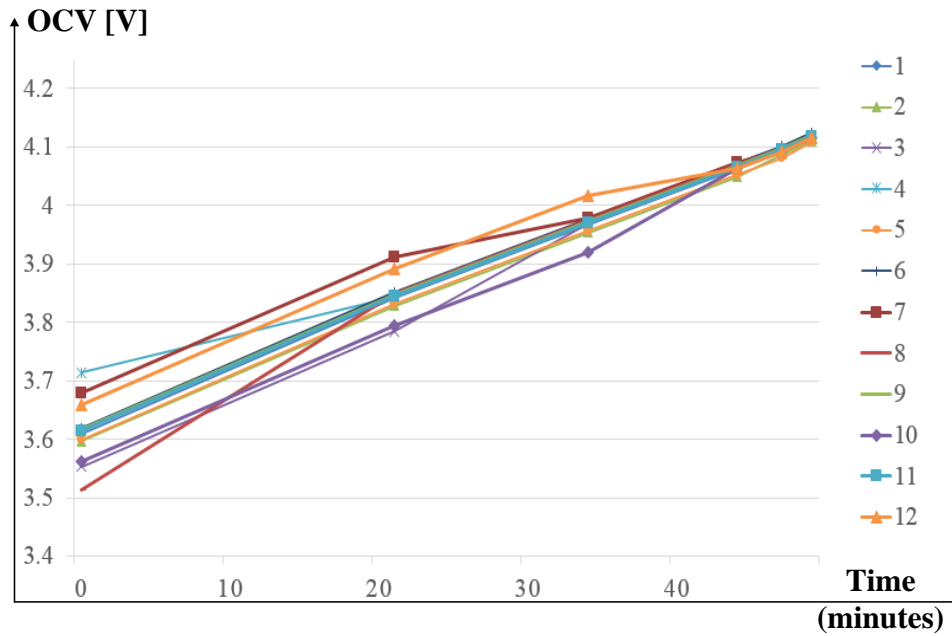
FIGURE 4.19: Balancing process during charging battery pack.

using (4.24), the energy in the battery packs in Figure 4.19 and Figure 4.20 can be calculated as shown Figure 4.22.

Without using a balancing circuit, the battery module can only be charged up to 91% of the full capacity with the initial condition of the experiment setup. Therefore, 9% of the battery capacity is left unused, as shown in Figure 4.22(a). When discharging without the proposed balancing circuit, 7% of the capacity of the battery pack is left unused. Therefore, only 84% capacity of the battery module is used. By using the balancing circuit, the capacity of the battery pack is utilized as 98%, as shown in Figure 4.22(b). It can be concluded from the above experiments that the full capacity of a battery can only be utilized when the proposed balancing circuit and algorithm are applied.
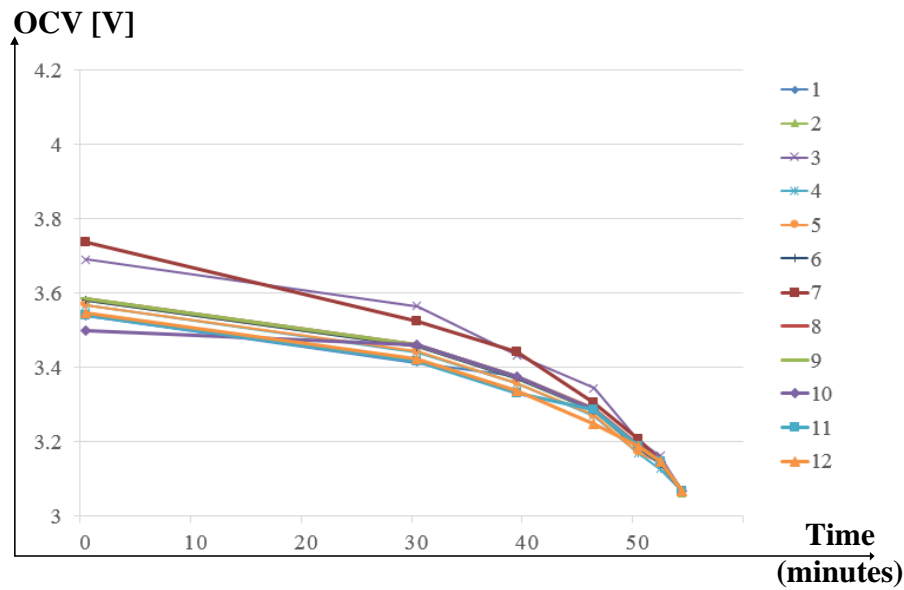
FIGURE 4.20: Balancing process during discharging battery pack.

4.4   Summary

Chapter 4 proposes a battery voltage balancing method to maximize the capacity

and correct the voltage of the Li-ion battery pack in HES systems. It is composed

of an isolated DC-DC converter, a relay network, the monitoring IC, and a DSP

controller. A simple balancing algorithm can achieve the cell balancing operation.

The open-circuit voltage (OCV), which is estimated based on a battery model, is in-

troduced to compensate for balancing current and load current to the terminal cell

voltage. Therefore, all the cells can be balanced at the average OCV. An isolated

LLC resonant converter is designed for the proposed balancing circuit to achieve

soft-switching for all of the primary switches and secondary diodes. An experiment

balancing circuit is implemented for twelve Li-ion cells in a battery module. All

cells are balanced at the average cell voltage. The maximum efficiency of 94.5% was

achieved for the balancing converter. The balancing current's ripple is 7%, which
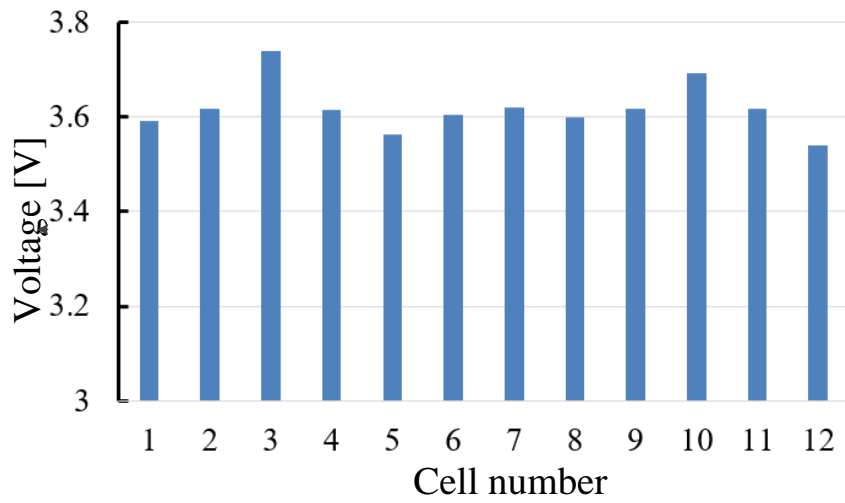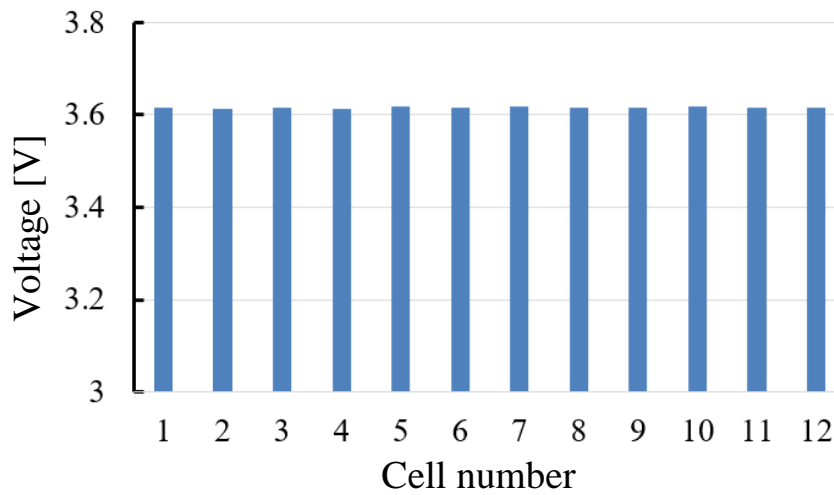
FIGURE 4.21: The voltage of each cell. (a) Before balancing; (b) After balancing.

is reduced from 100% in other direct cell-to-cell methods. Therefore, the proposed method can operate with a higher balancing current when using the same size of the hardware circuit. The experiment results show the battery capacity improvement of 14% from 84% to 98% by applying the balancing method to an experiment condition.
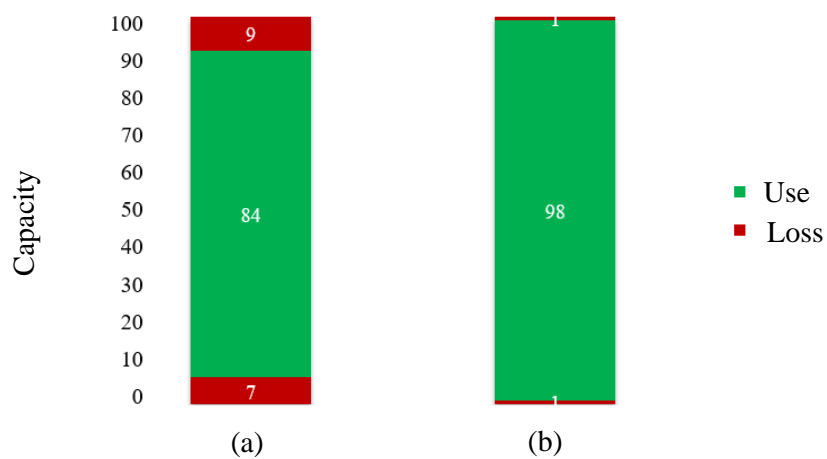
FIGURE 4.22: Comparison of the used capacity with and without a cell balancing circuit: (a) with balancing circuit; (b) without balancing circuit.

Chapter 5

Conclusions

5.1 Conclusions

In this dissertation, the technologies for realizing the HES systems using the TAB converter and studied. The effects of the voltage variation of the battery pack and other elements on the design of the TAB converter are analyzed. Then, inductances of the TAB converter are designed effetely by a normalized method. Besides, an active cell balancing circuit is proposed to solve issues of capacity loss and the voltage error of the battery pack. Therefore, the TAB converter can work with the designed voltage level and variation range in the HES systems' lifetime with maximized capacity. Each chapter addressed the following subjects and proposed the following contributions.

In chapter 2, a literature review associated with this dissertation is shown. Firstly, the HES applications using the TAB converter are discussed. The advantages and challenges of the TAB converter and Li-ion in each application are summarized. The voltage variation characteristics of the Li-ion battery and other storage or renewable energies are considered in the design of the TAB converter. Also, the usable capacity of the battery, which decides the usable capacity of the HES systems and voltage variation of the TAB converter, need to be corrected. Secondly, the current status of

the TAB converter is reviewed. The operation modes, control methods, and power transmission of the TAB converter are summarized. Twelve operation modes of the TAB converter are categorized into three groups as single input single output, dual input single output, and single input dual output. Many control methods are discussed. However, it remains a discussion about the design of the parameters of the TAB converters. The complicated relationship between parameters as inductances with powers and phase shift angles under the voltage variation is the remaining issue that needs to be solved. Thirdly, the capacity loss of Li-ion battery, which causes by the imbalance cell voltage between Li-ion battery cells in a battery pack, is revised based on the characteristics of the battery. The conventional cell balancing methods are analyzed.

In chapter 3, a design procedure of the TAB converter in considering the voltage variation of two ports is proposed. The voltage variations and inductances are normalized based on percentage, and the complicated relationships between the parameters of the TAB converter are clarified. The limitation of inductances corresponding to the different voltage variations is specified. The inductances are designed by the trade-off of the phase shift angle operating area, power transmission, and the peak current of the inductance. The proposed method is applied to design a system rated 400 V - 10 kW effectively. It shows that the normalized inductance is at 30% is one of the suitable design inductances when the voltage of primary and tertiary port varies from 85% to 110%. A prototype converter rated at 200 V and 500 W is implemented to verify the proposed method. The experimental results correspond to the phase shift angle calculation results within 1% error in the voltage range 85%-110%. Based

on this, the proposed method can be applied to design the TAB converter to be for various applications.

In chapter 4, a battery voltage balancing method for Li-ion battery pack in HES systems. It can reduce the cost of more than 18% in comparison to other conventional direct cell-to-cell methods. The configuration and operation principle of the proposed balancing circuit is introduced. The open-circuit voltage (OCV), which is estimated based on a battery model, is introduced to compensate for the effect of the balancing current and load current to the terminal cell voltage. Therefore, all the cells can be balanced at the average OCV. An isolated LLC resonant converter is designed for the proposed balancing circuit to achieve soft-switching for all of the primary switches and secondary diodes. An experiment balancing circuit is implemented for twelve Li-ion cells in a battery module. All cells are balanced at the average cell voltage. The maximum efficiency of 94.5% was achieved for the balancing converter. The experiment results show the battery capacity improvement of 14% from 84% to 98% by applying the balancing method to an experiment condition.

From the dialogue in this dissertation, the TAB converter and balancing circuit can be effectively designed for many HES applications with maximizing capacity and safety.

5.2 Future Works

The study of the TAB converter for the HES systems is analyzed in this dissertation. The design procedure of the TAB converter is proposed. A battery voltage balancing method is proposed to maximize the capacity of the battery and also HES systems.

There are nevertheless matters that ought to be considered. This section gives the comment and suggestion of further study in the future.

In chapter 2, the two-phase shift angles method can be applied to almost operation modes of the TAB converter due to simple implementation. Some other methods are proposed by controlling the mid-point voltage duty cycle, but they increase the complexity of the TAB converter, as discussed in chapter 2. It shows that some applications use all operation modes such as microgrid, distribution systems for data center, electric vehicles. Some applications do not use all operation modes. Therefore, which control method is better for each application can be discussed more in the future. In addition, there are many new applications of electricity that are discussing in academic and industry as all electrical ship, more electric aircraft, autonomous underwater vehicles. Therefore, new applications and characteristics of the TAB converter can be considered in the future.

A design procedure of the TAB converter was proposed, as shown in chapter 3. It clarified the relationships between inductances and phase shift operating areas in different voltage variations. The power transmission and peak current were discussed in the tread-off of the inductance. However, total converter loss is important and needs to be considered in the design in the future. Moreover, the magnetic component is a challenge in the practical design due to the complexity of the TAB converter and nonlinear characteristics of the magnetic material. Therefore, the transformer design needs to be studied to improve the performance of the TAB converter in different conditions.

A battery balancing circuit is proposed to maximize the battery pack capacity,

as discussed in chapter 4. It shows the advantage of low implementation cost and

small current ripple. However, the design can be optimized due to the size and total

efficiency. Moreover, the proposed method can be applied to other energy storage in

the HES systems. However, each type of energy storage has different characteristics

that require more analysis.

References

1 T. Zimmermann, P. Keil, M. Hofmann, M. F. Horsche, S. Pichlmaier, A. Jossen, "Review of system topologies for hybrid electrical energy storage systems," J. Energy Storage, vol. 8, pp. 78–90, 2016.

2 J. Li; S. Zhou; Y. Han, "Review REVIEW OF STRUCTURES AND CONTROL OF BATTERY-SUPERCAPACITOR HYBRID ENERGY STORAGE SYSTEM FOR ELECTRIC VEHICLES," in Advances in Battery Manufacturing, Service, and Management Systems , IEEE, 2017, pp.303-318.

3 Bao-Huy Nguyen, "Energy Management Strategy and Hybrid Vehicles Supplied by Hybrid Energy Storage Systems" Ph.D. thesis, Sep. 2019.

4 K.S. Krishna, K.S. Kumar, "A review on hybrid renewable energy systems," *Renew. Sustain. Energy Rev.*, vol. 52, pp. 907–916, 2015.

5 Y. Sawle, S. C. Gupta, A. K. Bohre, "Review of hybrid renewable energy systems with comparative analysis of off-grid hybrid system," and Sustainable Energy Reviews 2018.

6 International Energy Agency (IEA), "Global energy demand rose by 2.3 % in 2018, its fastest pace in the last decade," Browse date: 2020/4/28,
https://www.iea.org/newsroom/news/2019/march/global-energy-demand-rose-by-23-in-2018-its-fastest-pace-in-the-last-decade.html

7 Asia-Pacific Economic Cooperation, "APEC Energy Outlook 2019," Browse date: 2020/4/30,
https://aperc.or.jp/publications/reports/outlook.php

8 REN21, "Renewable 2019 global status report," Browse date: 2020/4/29,
https://www.ren21.net/what-are-the-current-trends-in-renewable-energy/

9 International Energy Agency (IEA), "Global EV Outlook 2019", IEA, Paris, Browse date: 2020/4/29,
https://www.iea.org/reports/global-ev-outlook-2019

10 J. Kim,C.J. Yu, M. Khammuang, J. Lui, A. Almujahid,T. Daim, "Forecasting Battery Electric Vehicles," In Proceedings of the 2017 IEEE Technology & Engineering Management Conference (TEMSCON), Santa Clara, CA, USA, 8–10 June 2017.

11 A. Q. Huang, M. L. Crow, G. T. Heydt, J. P. Zheng and S. J. Dale, "The Future Renewable Electric Energy Delivery and Management (FREEDM) System: The Energy Internet," *Proc. IEEE* **2011**, *9*, 133–148.

12 F. Blaabjerg, R. Teodorescu, M. Liserre and A. V. Timbus, "Overview of Control and Grid Synchronization for Distributed Power Generation Systems," *IEEE Trans. Ind. Electron.* **2006**, *53*, 1398–1409.

13 M. Sandelic, A. Sangwongwanich, F. Blaabjerg, "Reliability Evaluation of PV Systems with Integrated Battery Energy Storage Systems: DC-Coupled and AC-Coupled Configurations," Electronics, 2019, 8, 1059.

14 M. Longo, W. Yaïci, F. Foiadelli, "Electric Vehicle Charge with Residential's Roof Solar Photovoltaic System: A Case Study in Ottawa," In Proceedings of the 2017 IEEE 6th International Conference on Renewable Energy Research and Applications (ICRERA), Nov. 2017; pp. 121–125.

15 M. Yilmaz, P.T. Krein, "Review of the Impact of Vehicle-to-Grid Technologies on Distribution Systems and Utility Interfaces," *IEEE Trans. Power Electron.* **2013**, *28*, 5673–5689.

16 E. Planas, J. Andreu, J.I. Gárate, I.M. De Alegría, E. Ibarra, "AC and DC Technology in Microgrids: A Review," *Renew. Sustain. Energy Rev.* **2015**, *43*, 726–749.

17 B. Wunder, L. Ott, M. Szpek, U. Boeke, R. Weis, "Energy efficient dc-grids for commercial buildings," in Proceedings of the Telecommunications Energy Conference (INTELEC), Vancouver, BC, Canada, 28 September–2 October 2014; pp. 1–8.

18 U. Boeke, R. Wei, A. Mauder, L. Hamilton, L. Ott, "Efficiency advantages of +-380 v dc grids in comparison with 230 v/400 v ac grids," in *DCC +G and ENIAC*; White Paper; 2014.

19 C.C. Chan, "The State of the Art of Electric, Hybrid, and Fuel Cell Vehicles," *Proc. IEEE* **2007**, *95*, 704–718.

20 O. Z. Sharaf, M.F. Orhan, "An overview of fuel cell technology: Fundamentals and applications" *Renew. Sustain. Energy Rev.* **2014**, *32*, 810–853.

21 H. He, Y. Zhang, F. Wan, "Control strategies design for a fuel cell hybrid electric vehicle," in Proceedings of the IEEE Vehicle Power and Propulsion Conference, Harbin, China, 3–5 September 2008; pp. 1–6.

22 US Department of Energy, *The Department of Energy Hydrogen and Fuel Cells Program Plan*; "An integrated strategic plan for the research, development, and demonstration of hydrogen and fuel cell technologies," US Department of Energy: Washington, D.C., USA, 2011.

23 W Gao, "Performance comparison of a fuel cell-battery hybrid powertrain and a fuel cell- ultracapacitor hybrid powertrain" in Proceedings of the Power Electronics in Transportation (IEEE Cat. No.04TH8756), Novi, MI, USA, 21–22 October 2004; pp. 143–150.

24 L. Kouchachvili, W. Yaïci, E. Entchev, "Hybrid battery/supercapacitor energy storage system for the electric vehicles," J. Power Sources, vol. 374, no. June 2017, pp. 237–248, 2018.

25 S. Mukherjee, D. Mukherjee, D. Kastha, "Multiport soft-switching bidirectional DC-DC converter for hybrid energy storage systems," Conf. Proc. - IEEE Appl. Power Electron. Conf. Expo. - APEC, vol. 2019-March, no. 1, pp. 2103–2109, 2019.

26 S. Inoue, H. Akagi, "A Bidirectional Isolated DC–DC Converter as a Core Circuit of the Next-Generation Medium-Voltage Power Conversion System," *IEEE Trans. Power Electron.* **2007**, *22*, 535–542.

27 B. Zhao, Q. Song, W. Liu, Y. Sun, "Overview of Dual-Active-Bridge Isolated Bidirectional DC–DC Converter for High-Frequency-Link Power-Conversion System," *IEEE Trans. Power Electron.*, **2014**, *29*, 4091–4106.

28 J.L. Duarte, M. Hendrix, M.G. Simoes, "Three-Port Bidirectional Converter for Hybrid Fuel Cell Systems," *IEEE Trans. Power Electron.* **2007**, *22*, 480–487.

29 Y. Qiao, K. Jiang, H. Deng, et al. "A high-energy-density and long-life lithium-ion battery via reversible oxide–peroxide conversion," Nature Catalysis 2, 1035–1044, 2019.

30 A. Affanni, A. Bellini, G. Franceschini, P. Guglielmi, C. Tassoni, "Battery Choice and Management for New-Generation Electric Vehicles," IEEE Trans. Power Electron. 2005, 52, 1343–1349.

31 X. Gong, R. Xiong and C. C. Mi, "Study of the Characteristics of Battery Packs in Electric Vehicles With Parallel-Connected Lithium-Ion Battery Cells," in IEEE Trans. on Industry Applications, vol. 51, no. 2, pp. 1872-1879, 2015.

32 M. Caspar, T. Eiler, and S. Hohmann, "Comparison of active battery balancing systems," 2014 IEEE Veh. Power Propuls. Conf. VPPC 2014, 2014.

33 Van-Long Pham, Keiji Wada, "Applications of Triple Active Bridge Converter for Future Grid and Integrated Energy Systems," Energies, Vol. 13, No. 7, April, 2020.

34 S. Chowdhury, S.P. Chowdhury, P. Crossley, *"Microgrids and Active Distribution Networks"*, 1st ed.; IET: London, UK, 2009.

35 V.A. Prabhala, B.P. Baddipadiga, P. Fajri, M. Ferdowsi, "An Overview of Direct Current Distribution System Architectures & Benefits," Energies 2018, 11, 2463.

36 Y. Kado, D. Shichijo, I. Deguchi, N. Iwama, R. Kasashima, K. Wada, "Power flow control of three-way isolated DC/DC converter for Y-configuration power router," in Proceedings of the 2015 IEEE 2nd International Future Energy Electronics Conference (IFEEC), Taipei, Taiwan, 1–4 November 2015; pp. 1–5.

37 Y. Kado, D. Shichijo, K. Wada, K. Iwatsuki, "Multiport power router and its impact on future smart grids," *Radio Sci.* **2016**, *51*, 1234–1246.

38 K. Nishimoto, Y. Kado, K. Wada, "Implementation of Decoupling Power Flow Control System in Triple Active Bridge Converter Rate 400 V, 10 kW, and 20 kHz," *IEEJ J. Ind. Appl.***2018**, *7*, 410–415.

39 S. Nakagawa, J. Arai, R. Kasashima, K. Nishimoto, Y. Kado, K. Wada, "Dynamic performance of triple-active bridge converter rated at 400 V, 10 kW, and 20 kHz," in Proceedings of the IEEE International Future Energy Electronics Conference and ECCE Asia, Kaohsiung, Taiwan, 3–7 June 2017; pp. 1090–1094.

40 C. Zhao, J.W. Kolar, "A novel three-phase three-port UPS employing a single high-frequency isolation transformer," in Proceedings of the 2004 IEEE 35th Annual Power Electronics Specialists Conference (IEEE Cat. No.04CH37551), Aachen, Germany, 20–25 June 2004; pp. 4135–4141.

41 A.H. Ahmed Adam, S. Hou, J. Chen, "Analysis, Design, and Performance of Isolated Three-Port UPS Converter for High-Power Applications," in Proceedings of the 2019 IEEE International Conference on Environment and Electrical Engineering and 2019 IEEE Industrial and Commercial Power Systems Europe (EEEIC / I&CPS Europe), Genova, Italy, 10–14 June 2019; pp. 1–7.

42 H. Tao, J.L Duarte, M.A.M. Hendrix, Line-Interactive UPS Using a Fuel Cell as the Primary Source," *IEEE Trans. Ind. Electron.***2008**, *55*, 3012–3021.

43 M.M.J.A. Michon, J.L. Duarte, M. Hendrix, M.G. Simoes, "A three-port bi-directional converter for hybrid fuel cell systems," in Proceedings of the 2004 IEEE 35th Annual Power Electronics Specialists Conference, Aachen, Germany, 20–25 June 2004; pp. 4736–4742.

44 H. Tao, A. Kotsopoulos, J.L. Duarte, M.A.M Hendrix, "Transformer-Coupled Multiport ZVS Bidirectional DC-DC Converter with Wide Input Range," *IEEE Trans. Power Electron.* **2008**, *23*, 771–781.

45 M. Wiboonrat, "An empirical study on data center system failure diagnosis," in Proceedings of the 3rd International Conference on Internet Monitoring and Protection, Bucharest, Romania, 29 June–5 July 2008.

46 Y. Yu, K. Masumoto, K. Wada, Y. Kado, "A DC Power Distribution System in a Data Center Using a Triple Active Bridge DC-DC Converter," *IEEJ J. Ind. Appl.* **2018**, *7*, 202–209.

47 Y. Yu, K. Wada, "Simulation Study of Power Management for a Highly Reliable Distribution System using a Triple Active Bridge Converter in a DC Microgrid," *Energies* **2018**, *11*, 3178.

48 Y. Yu, K. Masumoto, K. Wada, Y. Kado, "Power Flow Control of a Triple Active Bridge DC-DC Converter Using GaN Power Devices for a Low-Voltage DC Power Distribution System," in Proceedings of the 2017 IEEE 3rd International Future Energy Electronics Conference and ECCE Asia (IFEEC 2017—ECCE Asia), Kaohsiung, Taiwan, 3–7 June 2017; pp. 772–777.

49 M. Yilmaz, P.T. Krein, "Review of battery charger topologies, charging power levels, and infrastructure for plug-in electric and hybrid vehicles," *IEEE Trans. Power Electron.*, **2013**, *28*, 2151–2169.

50 S.Y. Kim, H. Song, K. Nam, "Idling Port Isolation Control of Three-Port Bidirectional Converter for EVs," *IEEE Trans. Power Electron.* **2012**, *27*, 2495–2506.

51 S.Y. Kim, I. Jeong, K. Nam, H.S. Song, "Three-Port Full Bridge Converter Application as a Combined Charger for PHEVs," In Proceedings of the 2009 IEEE Vehicle Power and Propulsion Conference, Dearborn, MI, USA, 7–10 September 2009; pp. 461–465.

52 Z. Ling, H. Wang, K. Yan, J. Gan, "Optimal Isolation Control of Three-Port Active Converters as a Combined Charger for Electric Vehicles," *Energies* **2016**, *9*, 715.

53 D.-D. Nguyen, G. Fujita, C.-M. Ta, "New Soft-Switching Strategy for Three-Port Converter to be Applied in EV Application," in Proceedings of the 2017 IEEE 3rd International Future Energy Electronics Conference and ECCE Asia, Kaohsiung, Taiwan, 3–7 June 2017.

54 C. Zhao, S.D. Round, J.W. Kolar, "An Isolated Three-Port Bidirectional DC-DC Converter with Decoupled Power Flow Management," *IEEE Trans. Power Electron.* **2008**, *23*, 2443–2453.

55 Van-Long Pham, and Keiji Wada, "Implementation Decoupling Control for Triple Active Bridge Converter in Green Building Electrical System," in Vietnam – Japan Science and Technology Symposium 2019 (VJST 2019), Hanoi, Vietnam, May, 2019.

56 B. Sarlioglu, C.T. Morris, "More Electric Aircraft: Review, Challenges, and Opportunities for Commercial Transport Aircraft," *IEEE Trans. Transp. Electrif.* **2015**, *1*, 54–64.

57 P.W. Wheeler, J.C. Clare, A. Trentin, S. Bozhko, "An overview of the more electrical aircraft," *J. Aerosp. Eng.* **2012**, *227*, 578–585.

58 X. Roboam, O. Langlois, H. Piquet, B. Morin, C. Turpin, "Hybrid power generation system for aircraft electrical emergency network," *IET Electr. Syst. Transp.* **2011**, *1*, 148–155.

59 S. Wu, Y. Li, "Fuel cell applications on more electrical aircraft," In Proceedings of the 17th International Conference on Electrical Machines and Systems (ICEMS), Hangzhou, China, 24–25 October 2014; pp. 198–201.

60 F. Giuliani, G. Buticchi, M. Liserre, N. Dehnonte, P. Cova, N. Pignoloni, "GaN-based triple active bridge for avionic application. In Proceedings of the 2017 IEEE 26th International Symposium on Industrial Electronics (ISIE), Edinburgh, Edinburgh, Scotland, 19–21 June 2017; pp. 1856–1860.

61 A.M. Bradley, M.D. Feezor, H. Singh, F.Y. Sorrell, "Power systems for autonomous underwater vehicles," in *IEEE J. Ocean. Eng.* **2001**, *26*, 526–538.

62 T. Hyakudome, T. Nakatani, H. Yoshida, T. Tani, H. Ito, K. Sugihara, "Development of fuel cell system for long cruising lange Autonomous Underwater Vehicle," In Proceedings of the 2016 IEEE/OES Autonomous Underwater Vehicles (AUV), Tokyo, Japan, 6–9 November 2016; pp. 165–170.

63 M.M Albarghot, M.T. Iqbal, K. Pope, L. Rolland, "Sizing and dynamic modeling of a power system for the MUN explorer autonomous underwater vehicle using a fuel cell and batteries," *J. Energy* **2019**, *2019*, 4531497.

64 J.S. Thongam, M. Tarbouchi, A.F. Okou, D. Bouchard, R. Beguenane, "All-electric ships—A review of the present state of the art," in Proceedings of the 2013 Eighth International Conference and Exhibition on Ecological Vehicles and Renewable Energies (EVER), Monte Carlo, Monaco, 27–30 March 2013; pp. 1–8.

65 G. Seenumani, J. Sun, H. Peng, "Real-Time Power Management of Integrated Power Systems in All Electric Ships Leveraging Multi Time Scale Property," *IEEE Trans. Control Syst. Technol.* **2012**, *20*, 232–240.

66 A. Tessarolo, S. Castellan, R. Menis, G. Sulligoi, "Electric generation technologies for all-electric ships with Medium-Voltage DC power distribution systems," In Proceedings of the 2013 IEEE Electric Ship Technologies Symposium (ESTS), Arlington, VA, USA, 22-24 April 2013; pp. 275–281.

67 K. Kim, K. Park, J. Ahn, G. Roh, K. Chun, "A study on applicability of Battery Energy Storage

System (BESS) for electric propulsion ships," in Proceedings of the 2016 IEEE Transportation Electrification Conference and Expo, Asia-Pacific (ITEC Asia-Pacific), Busan, Korea, 1–4 June 2016; pp. 203–207.

68 Y. Tran, D. Dujic, "A multiport medium voltage isolated DC-DC converter," In Proceedings of the IECON 2016—42nd Annual Conference of the IEEE Industrial Electronics Society, Florence, Italy, 23-26 October 2016; pp. 6983–6988.

69 S. Ilango, R. Viju Nair, R. Chattopadhyay, S. Bhattacharya, "Photovoltaic and Energy Storage Grid Integration with Fully Modular Architecture using Triple Port Active Bridges and Cascaded H-Bridge Inverter," In Proceedings of the IECON 2018—44th Annual Conf. of the IEEE Industrial Electronics Society, Washington D.C., USA, 21–23 October 2018; pp. 1400–1405.

70 J. Schäfer, D. Bortis, J.W. Kolar, "Multi-port multi-cell DC/DC converter topology for electric vehicle's power distribution networks," In Proceedings of the 2017 IEEE 18th Workshop on Control and Modeling for Power Electronics (COMPEL), Stanford, CA, USA, 9–12 July 2017; pp. 1–9.

71 H. Tao, J.L. Duarte, M.A.M Hendrix, "High-Power Three-Port Three-Phase Bidirectional DC-DC Converte," in Proceedings of the IEEE Industry Applications Annual Meeting, New Orleans, LA, USA, 23-27 Septemper 2007; pp. 2022–2029.

72 M. Neubert, A. Gorodnichev, J. Gottschlich, R.W. De Doncker, "Performance analysis of a triple-active bridge converter for interconnection of future dc-grids," in Proceedings of the 2016 IEEE Energy Conversion Congress and Exposition (ECCE), Milwaukee, WI, USA, 18–22 September 2016; pp. 1–8.

73 M. Neubert, H. Van Hoek, J. Gottschlich, R.W. De Doncker, "Soft-switching operation strategy for three-phase multiport-active bridge DC-DC converters," in Proceedings of the IEEE 12th International Conference on Power Electronics and Drive Systems (PEDS), Honolulu, Hawaii, USA, 12–15 December 2017; pp. 1,207–1,213.

74 J. Gottschlich, P. Weiler, M. Neubert, R.W. De Doncker, "Delta-sigma modulated voltage and current measurement for medium-voltage DC applications," in Proceedings of the 2017 19th European Conference on Power Electronics and Applications (EPE'17 ECCE Europe), Warsaw, Poland, 11–14 September 2017; pp. 1–9.

75 M. Neubert, S.P. Engel, J. Gottschlich, R.W. De Doncker, "Dynamic power control of three-phase multiport active bridge DC-DC converters for interconnection of future DC-grids," in Proceedings of the IEEE 12th International Conference on Power Electronics and Drive Systems (PEDS), Honolulu, HI, USA, 12–15 December 2017; pp. 639–646.

76 G. Engelmann, A. Sewergin, M. Neubert, R.W. De Doncker, "Design Challenges of SiC Devices for Low- and Medium-Voltage DC-DC Converter," in Proceedings of the 2018 International Power Electronics Conference (IPEC-Niigata 2018-ECCE Asia), Niigata, Japan, 20–24 May 2018; pp. 3979–3984.

77 M. Ouyang , Z. Chu, L. Lu, J. Li, X. Han, X. Feng, and G. Liu, "Low temperature aging mechanism identification and lithium deposition in a large format lithium iron phosphate battery for different charge profiles," J. Power Sources, vol. 286, pp. 309-320, Jul. 2015.

78 Shane D. Beattie, M.J. Loveridge, Michael J. Lain, S. Ferrari, Bryant J. Polzin, Rohit Bhagat, and R. Dashwood, "Understanding capacity fade in silicon based electrodes for lithium-ion batteries using three electrode cells and upper cut-off voltage studies," J. Power Sources, vol. 302, pp. 426-430, Jan. 2016.

79 Christopher D. Rahn, and Chao-Yang Wang, "Battery System Engineering," A John Wiley and Sons, Ltd., Publication, 2013, The Pennsylvania State University, USA, 2013

80 Mohamed Daowd, Noshin Omar, Peter Van Den Bossche, and Joeri Van Mierlo, "Passive and active battery balancing comparison based on MATLAB simulation," in Proc. IEEE Vehicle. Power Propulsion Conf., Sep. 6–9, 2011, pp. 1–7.

81 Wai Chung Lee, David Drury, and Phil Mellor, "Comparison of passive cell balancing and active cell balancing for automotive batteries," in Proc. IEEE Vehicle. Power Propulsion Conf., Sep. 6–9, 2011, pp. 1–7.

82 Nasser H. Kutkut, and Deepak M. Divan, "Dynamic equalization techniques for series battery stacks," in Proc. 18th Int. Telecommun. Energy Conf., 1996, pp. 514–521.

83 M. Raeber, A. Heinzelmann, and A. Taeschler, "Beneficial Effects of Active Charge Balancing in Lithium-Ion Battery Systems," Journal of Clean Energy Technologies vol. 4, no. 3, pp. 225-228, 2016.

84 Z. B. Omariba, L. Zhang and D. Sun, "Review of Battery Cell Balancing Methodologies for Optimizing Battery Pack Performance in Electric Vehicles," in IEEE Access, vol. 7, pp. 129335-129352, 2019.

85 Chol-Ho Kim, Moon-young Kim, Hong-sun Park, and Gun-Woo Moon, "A Modularized Two-Stage Charge Equalizer with Cell Selection Switches for Series-Connected Lithium-Ion Battery String in an HEV," IEEE Trans. Power Electron., vol. 27, no. 8, pp. 3764–3774, Aug. 2012.

86 Aiguo Xu, Shaojun Xie, and Xiaobao Liu, "Dynamic Voltage Equalization for Series-Connected Ultracapacitors in EV/HEV Applications," IEEE Trans. Veh. Technol., vol. 58, no. 8, pp.3981-3987, Oct. 2009.

87 Hong-sun Park, Chong-Eun Kim, Chol-Ho Kim, Gun-Woo Moon, and Joong-Hui Lee, "A Modularized Charge Equalizer for an HEV Lithium-Ion Battery String," IEEE Trans. Ind. Electron., vol.56, no.5, pp.1464-1476, May 2009.

88 Nasser H. Kutkut, Deepak M. Divan, and Donald W. Novotny, "Charge equalization for series connected battery strings," IEEE Trans. Ind. Appl., vol.31, no.3, pp.562-568, May/Jun. 1995.

89 Chang-Soon Lim, Kui-Jun Lee, Nam-Joon Ku, Dong-Seok Hyun, and Rae-Young Kim, "A Modularized Equalization Method Based on Magnetizing Energy for a Series-Connected Lithium-Ion Battery String," IEEE Trans. Power Electron., vol.29, no.4, pp.1791-1799, Apr. 2014.

90 Yunlong Shang; Bing Xia; Chenghui Zhang; Naxin Cui; Jufeng Yang; Chris Mi, "A Modularization Method for Battery Equalizers Using Multi-Winding Transformers," IEEE Trans. Veh. Technol., vol. 66, no. 10, pp. 8710-8722, 2017.

91 16. Abusaleh M. Imtiaz, and Faisal H. Khan, "Time Shared Flyback Converter Based Regenerative Cell Balancing Technique for Series Connected Li-Ion Battery Strings," IEEE Trans. Power Electron., vol. 28, no. 12, pp. 5960-5975, Dec. 2013.

92 Yao Guo; Rengui Lu, Guoliang Wu, and Chunbo Zhu, "A high efficiency isolated bidirectional equalizer for Lithium-ion battery string," in Vehicle Power and Propulsion Conf., Seoul 2012, pp. 962-966, 9-12 Oct. 2012.

93 Chol-Ho Kim, Moon-Young Kim, and Gun-Woo Moon, "A Modularized Charge Equalizer Using a Battery Monitoring IC for Series-Connected Li-Ion Battery Strings in Electric Vehicles," IEEE Trans. Power Electron., vol. 28, no. 8, pp. 3779-3787, Aug. 2013.

94 Haoqi Chen, Liang Zhang, Yehui Han, "System-Theoretic Analysis of a Class of Battery Equalization Systems: Mathematical Modeling and Performance Evaluation," IEEE Trans. Veh. Technol., vol. 64, no. 4, pp. 1445-1457, 2015.

95 H.-S. Park, C.-H. Kim, K.-B. Park, G.-W. Moon, and J.-H. Lee, "Design of a charge equalizer based on battery modularization," IEEE Trans. Veh. Technol., vol. 58, no. 7, pp. 3216–3223, 2009.

96 Moon-Young Kim, Chol-Ho Kim, Jun-Ho Kim, and Gun-Woo Moon, "A Chain Structure of Switched Capacitor for Improved Cell Balancing Speed of Lithium-Ion Batteries," IEEE Trans. Ind. Electron., vol. 61, no. 8, pp.3989-3999, Aug. 2014.

97 M. Uno, and K. Tanaka "Influence of High-Frequency Charge–Discharge Cycling Induced by Cell Voltage Equalizers on he Life Performance of Lithium-Ion Cells," IEEE Trans. Veh. Technol., vol.

60, no. 4, pp. 1505 - 1515, 2011.

98 Andrew C. Baughman and Mehdi Ferdowsi, "Double-Tiered Switched-Capacitor Battery Charge Equalization Technique," IEEE Trans. Ind. Electron., vol. 55, no. 6, pp. 2277-2285, Jun. 2008.

99 T. Hai Phung, Alexandre Collet, and Jean-Christophe Crebier, "An Optimized Topology for Next-to-Next Balancing of Series-Connected Lithium-ion Cells," IEEE Trans. Power Electron., vol. 29, no. 9, pp. 4603-4613, Sept. 2014.

100 Sang-Hyun Park, Ki-Bum Park, Hyoung-Suk Kim, Gun-Woo Moon, and Myung-Joong Youn, "Single-Magnetic Cell-to-Cell Charge Equalization Converter With Reduced Number of Transformer Windings," IEEE Trans. Power Electron., vol. 27, no. 6, pp. 2900-2911, Jun. 2012.

101 Moon-Young Kim, Jun-Ho Kim, and Gun-Woo Moon, "Center-Cell Concentration Structure of a Cell-to-Cell Balancing Circuit with a Reduced Number of Switches," IEEE Trans. Power Electron., vol. 29, no. 10, pp. 5285-5297, Oct. 2014.

102 Mohamed Daowd, Mailier Antoine, Noshin Omar, Peter van den Bossche and Joeri, van Mierlo, "Single Switched Capacitor Battery Balancing System Enhancements," Energies, 6, pp. 2149-2174, 2013.

103 Sang-Hyun Park, Tae-Sung Kim, Jin-Sik Park, Gun-Woo Moon, and Myung-Joong Yoon, "A New Buck-boost Type Battery Equalizer," in Proc. IEEE 24th Annu. Appl. Power Electron. Conf. Expo., Feb. 15–19, 2009, pp. 1246–1250.

104 K.-M. Lee, Y.-C. Chung, C.-H. Sung, and B. Kang, "Active Cell Balancing of Li-Ion Batteries using LC resonant circuit," IEEE Trans. Ind. Electron., vol. 62, no. 9, pp. 5491-5501, Sep. 2015.

105 Van-Long Pham, Keiji Wada, "Normalization Design of Inductances in Triple Active Bridge Converter for Household Renewable Energy System," *IEEJ J. Ind. Appl.*, Vol. 9, No. 3, **2020**, pp. 227-234.

106 Van-Long Pham, Keiji Wada, "Design of Series Inductances in Triple Active Bridge Converter Using Normalization Procedure for Integrated EV and PV System," 2019 10th International Conference on Power Electronics and ECCE Asia (ICPE 2019 - ECCE Asia), Busan, Korea (South), 2019, pp. 3027-3032.

107 Tamura, "Smoothing Permalloy dust choke coils," AHD Coils.

108 Coilcraft, "Shielded Power Inductors – XAL1010," Document 804, Revised 11/2/18 (2018).

109 Van-Long Pham, V.-T. Duong, W. Choi, "High-efficiency Active Cell-to-Cell Balancing Circuit for Lithium-Ion Battery Modules using LLC Resonant Converter," Journal of Power Electronics, 20, pp. 1037–1046, 2020.

110 Van-Long Pham, V.T. Duong, W. Choi, "A Low Cost and Fast Cell-to-Cell Balancing Circuit for Lithium-Ion Battery Strings," Electronics Vol.9, No. 248, 2020.

111 Van-Long Pham, T.-T. Nguyen, D.-H. Tran, V.-B. Vu, W. Choi, "A new cell-to-cell fast balancing circuit for Lithium-ion batteries in Eelectric Vehicle and Energy Storage System," in Proc. IEEE 8th International Power Electronic and Motion Control Conf., 2016, pp. 2461-2465.

112 Van-Long Pham, A.-B. Khan, T.-T. Nguyen, W. Choi, "A low cost, small ripple, and fast balancing circuit for lithium-ion battery strings," in Proc. IEEE Transportation Electrification Conference and Expo, Asia-Pacific, 2016, pp. 861-865.

113 H. He, R. Xiong, J. Fan, "Evaluation of Lithium-Ion Battery Equivalent Circuit Models for State of Charge Estimation by an Experimental Approach," Energies 2011, 4, 582–598.

114 W. Waag, S. Käbitz, D.U. Sauer, "Experimental investigation of the lithium-ion battery impedance characteristic at various conditions and aging states and its influence on the application," Appl. Energy 2013, 102, 885–897.

115 J. Kim, J. Shin, C. Chun, B.-H. Cho, "Stable Configuration of a Li-Ion Series Battery Pack Based on

a Screening Process for Improved Voltage/SOC Balancing," IEEE Trans. Power Electron. 2012, 27, 411–424.

116 J.H. Kim, S.J. Lee, J.M. Lee, B.H. Cho, "A new direct current internal resistance and state of charge relationship for the Li-ion battery pulse power estimation," In Proceedings of the 2007 7th Internatonal Conference on Power Electronics, Daegu, Korea, 22–26 October 2007.

117 Y. Barsukov, J. Qian, "Battery Power Management for Portable Devices" Atech Hourse: Boston, MA, USA, 2013.

118 N-T. Tran, K-H. Nguyen, Van-Long Pham, A. B. Khan, W. Choi, "SOC/SOH Estimation Method for AGM VRLA Battery by Combining ARX Model for Online Parameters Estimation and DEKF Considering Hysteresis and Diffusion Effects," in Proc. of 9th International Conference on Power Electronics and ECCE Asia (ICPE-ECCE Asia), Seoul, 2015, pp. 1169-1175.

Journal papers

1. Van-Long Pham, and Keiji Wada, "Normalization Design of Inductances in Triple Active Bridge Converter for Household Renewable Energy System," *IEEJ Journal of Industry Applications*, Vol. 9, No. 3, May, **2020**.

2. Van-Long Pham, and Keiji Wada, "Applications of Triple Active Bridge Converter for Future Grid and Integrated Energy Systems," *Energies*, Vol. 13, No. 7, April, **2020**.

3. Van-Long Pham, V-T. Duong, and W. Choi, "High Efficiency Active Cell-to-Cell Balancing Circuit for Lithium-Ion Battery Modules Using an LLC Resonant Converter," *Journal of Power Electronic (2020)*, April 28, **2020**.

4. Van-Long Pham, V-T. Duong, and W. Choi, "A Low Cost and Fast Cell-to-Cell Balancing Circuit for Lithium-Ion Battery Strings," *Electronics*, Vol.9, No. 2, January, **2020**.

Patent

1. W. Choi, and Pham Van Long, "Apparatus and Method for Battery Cell Balancing Control", Patent no. 10-1720027, Korean Intellectual Property Office, March, 2017. (DOI: 10.8080/1020160097359)

International Conference

1. Van-Long Pham, and Keiji Wada, "Design of Series Inductances in Triple Active Bridge Converter Using Normalization Procedure for Integrated EV and PV System", in Proceedings of International Conference on Power Electronics (ICPE 2019 ECCE Asia), Busan, Korea, May 27-30, 2019, pp. 3027-3032.

2. Van-Long Pham, and Keiji Wada, "Implementation Decoupling Control for Triple Active Bridge Converter in Green Building Electrical System," in Vietnam – Japan Science and Technology Symposium 2019 (VJST 2019), Hanoi, Vietnam, May, 2019.

3. Van-Long Pham, T-T. Nguyen, D-H. Tran, V-B. Vu, and W. Choi, "A New Cell-to-Cell Fast Balancing Circuit for Lithium-Ion Battery in Electric Vehicles and Energy Storage System", in Proceedings of IEEE 8th International Power Electronic and Motion Control Conference (IPEMC-ECCE Asia), Hefei, China, May 22-25, 2016, pp. 2461-2465.

4. Van-Long Pham, A. B. Khan, T-T. Nguyen, and W. Choi, "A Low Cost, Small Ripple, and Fast Balancing Circuit for Lithium-Ion Battery String," in Proceedings of IEEE Transportation Electrification Conference and Expo Asia-Pacific, ITEC 2016 Busan, June 1-4, 2016, pp. 861-865.

5. D-H. Tran, V-B. Vu, Van-Long Pham, and W. Choi, "Design and Implementation of High Efficiency Wireless Power Transfer System for On-Board Charger of Electric Vehicle," in Proceedings of 8th International Power Electronics and Motion Control

Conference –ECCE Asia, IPEMC 2016, May 22 – 25, 2016, pp. 2466 – 2469.

6. V-B. Vu, V-T. Doan, Van-Long Pham and W. Choi, "A New Method to Implement the Constant Current - Constant Voltage Charge of the Inductive Power Transfer System for Electric Vehicle Applications," in Proceedings of IEEE Transportation Electrification Conference and Expo Asia-Pacific, ITEC 2016 Busan, June 1-4, 2016, pp. 449-453.

7. D-D. Tran, HN Vu, HH Lee, Van-Long Pham, and W Choi, "A novel 10kW hybrid converter for the electric vehicle charge applications", in Proceedings of IEEE Transportation Electrification Conference and Expo Asia-Pacific, ITEC 2016 Busan, June 1-4, 2016, pp. 220-224.

8. A-B. Khan, Van-Long Pham, TT Nguyen, and W Choi, "Multistage constant-current charging method for Li-Ion batteries", in Proceedings of IEEE Transportation Electrification Conference and Expo Asia-Pacific, ITEC 2016 Busan, June 1-4, 2016, pp. 381-385.

9. V-B. Vu, DH Tran, Van-Long Pham, and W Choi, "Implementation of the CC/CV Charge of the Wireless Power Transfer System for Electric Vehicle Battery Charge Applications", in Proceedings of the Korea Institute of Power Electronics Summer Annual Conference, Korea, July 2015, pp. 25-26.

10. N-T. Tran, K-H. Nguyen, Van-Long Pham, A. B. Khan, and W. Choi, "SOC/SOH Estimation Method for AGM VRLA Battery by Combining ARX Model for Online Parameters Estimation and DEKF Considering Hysteresis and Diffusion Effects," in Proceedings of 9th International Conference on Power Electronics and ECCE Asia (ICPE-ECCE Asia), Seoul, 2015, pp. 1169-1175.

Domestic Conferences

1. Van-Long Pham, A. B. Khan, T-T. Nguyen, and W. Choi, "A Cell-to-Cell Fast Balancing Circuit for Lithium-Ion Battery Module," in Proceedings of the Korea Institute of Power Electronics Fall Annual Conference, Korea, November, 2015, pp. 7-8.

2. Van-Long Pham, K-H. Nguyen, A. B. Khan, and W. Choi, "A Direct Cell-to-Cell Charge Balancing Circuit for EVs Battery Module," in Proceedings of the Korea Institute of Power Electronics Summer Annual Conference, Korea, July 2015, pp. 401-402.

Acknowledgements

First of all, I would like to thank my supervisor, Prof. Keiji Wada, very much for your support and encouragement. You demonstrated your patience, commitment, dedication and inspired me to continue exploring and overcoming the difficulties Your constant encouragement in academic aspects has allowed me to accumulate knowledge, improve research skills, and develop the management ability. Besides, you have kept giving me a lot of opportunities to grow me up. Of course, I know that I had to open my path by myself, but I am sure that I could not pass or achieve what I did during the doctoral course without your support and agreements. I could keep research and achieve short- and long-term goals in all of my research life in TMU.

I would like to express my special gratitude to Prof. Toshihisa Shimizu for advising and educating me during the doctoral course. I was inspired by your constant help and support, personality, knowledge, and experience, leadership, and critical thinking. I felt in a blessed environment because I can communicate easily with you, who is one of the most achieved professors in power electronics.

Besides my supervisor, I would like to thank Prof. Toshihisa Shimizu and Prof. Yukihisa Suzuki of my thesis committee. You took out valuable time in my defense and reviewing my dissertation. I appreciate your insightful or critical comments and constructive criticism. I could well examine my research from various perspectives.

I really appreciate to Korean supervisor Prof. Woojin Choi. You allowed me to develop my knowledge and skills from the master's program and support me in preparing for the doctoral program. Also, I never forget you guys who are RECL-SSU members. You are so kind and hardworking. Thank Dr. Van-Tuan Doan for

your guideline. Thank Mr. Van-Tinh Duong for your support to publish my research.

I really appreciate the laboratory members who have contributed immensely to my studying and personal time. The laboratory has been a source of friendships, good advice, and collaboration. We studied and participated in conferences and many activities together. Besides, I very much appreciated their enthusiasm, intensity, and willingness to support me, and I could breakthrough so much because of your all kind support. Laboratory member: Mr. Hisao Akiyama, Mr. Eiji Ikuta, Mr. Hirofumi Suda, Mr. Yoshio Bizen, Dr. Pin-Yu Huang, Dr. Tomoyuki Mannen, Dr. Hiroaki Matsumori, Dr. Yu Shan Cheng, Dr. Yoshihiro Miwa, Dr. Yu Yue, Dr. Daiki Yamaguchi, Dr. Yoshikazu Kuwabara, Mr. Shinichiro Hayashi, Mr. Turmandakh Bat-Orgil, Mr. Kazuki Matsubara, Mr. Keisuke Masumoto, Mr. Ryo Shirai, Mr. Keisuke Suzuki, Mr. Koji Mitsui, Mr. Daiki Masuko, Mr. Takaya Sekiguchi, Mr. Mitsuhito Sagara, Mr. Hiroshi Tokuyama, Mr. Ryuta Shimamoto, Mr. Keigo Arita, Mr. Kawa Hayashi, the other all laboratory members and graduated members, and Secretaries: Ms. Ryuko Saitoh, Ms. Noriko Kubota. Thank Mr. Mitsui, Mr. Masuko, and Mr. Suzuki for your support to set up my life in Japan from the beginning. Thank Dr. Miwa, Dr. Kuwabara, and Mr. Shinichiro Hayashi, Mr. Ryo Shirai for a lot of support.

I appreciate to members of the Board of committees of Vietnam power electronics community (VPEC) and Vietnam academic network in Japan (VANJ) for giving me the opportunities to discuss wide knowledge areas and organize the events for developing academic networks. You are so talented and have excellent skills and

attitudes for research and society. That inspired me a lot. I would like to thank international affairs office for many support. I would like to thank Vietnamese and international friends in TMU for being friends and sharing at many events.

Finally, I would like to thank all my family: my father, mother, mother-in-law, father-in-law, sister, brothers, brother-in-law, grandmother, uncles, aunts. You are always supporting me and on side me. Especially, I would like to thank my wife and my children, who always stay with me and make me stronger with love. I really appreciate that, and thank you for continuing your support and encouragement.